THE INFLUENCE OF ELECTRODE SURFACE CONDITIONS ON THE BOUNCING BEHAVIOUR OF LOW-VELOCITY CHARGED MICROSPHERES IN A HIGH FIELD GAP

by SUNITA MOHINDRA B.Sc (Hons)

A Thesis submitted for the degree of
DOCTOR OF PHILOSOPHY
University of Aston in Birmingham
January 1981

A thesis submitted for the degree of Doctor of Philosophy

by Sunita Mohindra (1981)

SUMMARY

This study presents an experimental and theoretical investigation into the influence of electrode surface conditions on the bouncing impact behaviour of charged microparticles in a high voltage gap. It uses a simulation technique based on a microparticle gun that can inject positively charged, low velocity microparticles into a planar UHV gap. Experiments have been performed on different combinations of particle/target materials (e.g. carbonyl - iron, gold, titanium, copper and nickel) and a variety of surface states (e.g. mechanically polished, argon ion etched, electron bombarded and electropolished) which are monitored ellipsometrically.

It is found firstly, that the mean mechanical behaviour as characterized by the coefficient of restitution or e-values exhibits general trends which are similar to those found with corresponding macro systems. The observed differences in the critical velocity for elastic impact for the micro and macro systems and the large scatter in the measured e-values are interpreted in terms of the microtopography of a surface. Secondly, the electrical behaviour, as characterized by the ratio reversed/initial charge or Q-values, is found i) to exhibit overall trends that are similar for all particle/electrode combinations and ii) to vary in magnitude for individual surfaces. This is interpreted in terms of the electrical properties of the contaminating films, in particular the tunnelling resistivity and relative work functions of the junction oxide layers which are shown to be influential in determining the magnitude of charge transferred (Q_r) and hence the Q-values.

Theoretically, the evaluation and assessment of an existing model based on quantum mechanical tunnelling across the oxide junction has resulted in a modified expression for Q_r which predicts theoretical values that are in close agreement with experimental values.

Finally, in considering the technological implications of these findings it has been shown that although both the mechanical and electrical properties determine the breakdown criterion for a material it is the electrical properties which are the more dominant.

Microparticle-low-velocity bouncing, surface conditions/work functions/ electrical breakdown / coefficient of restitution

A C K N O W L E D G E M E N T S

I would like to thank my supervisor Dr. R. V. Latham for his advice and many hours of helpful discussion throughout the course of this project

I would also like to thank the following -

The Physics workshop staff, especially Mr. F. Lane, for their help in the construction of several components.

Professor S. E. Hunt for the use of the departmental facilities.

The Science Research Council for their financial support.

Mrs. E. A. N. Bremner for typing the manuscript.

LIST OF CONTENTS

CHAPTER 1

CHAPTER 2

CHAPTER 3

CHAPTER 4

CHAPTER 5

CHAPTER 6

LIST OF FIGURES

CHAPTER 1

1.0 Introduction

1.1 The phenomenon of vacuum breakdown

As a result of the progress in vacuum technology, there has been an increased interest in the electrical insulating properties of ultra high vacuum. The use of a vacuum gap as an insulator in commercial high voltage devices, such as high energy particle accelerators, X ray tubes, electron microscopes, etc., is common. However there are severe limits to its insulating capability and when breakdown occurs it is frequently an irreversible and catastrophic process that has profound implications for the design of such high voltage equipment. In theory, it would appear that the absence of a charge carrying medium in ultra high vacuum should provide ideal insulation between a pair of metal electrodes. In practice, however, there is some characteristic voltage for a given gap at which an arc is struck between the two electrodes and its resistance falls to zero i.e. electrical breakdown occurs.

Under "commercial" vacuum conditions (i.e. $> 10^{-5}$ mbar) initiation of electrical breakdown is believed to be due to ionisation effects associated with either the residual gas or desorption from the electrode surface. At sufficiently low pressures however, ($\leq 10^{-7}$ mbar) the initiation of the arc or electrical breakdown becomes nearly independent of the residual gas pressures and appears to be determined by the properties of the electrodes. It has now become widely accepted that the complex phenomenon of electrical breakdown resulting from a

transition of gap insulation to gap conduction is dependent on a number of parameters; the most obvious of these being

i) the electrode material, geometry and temperature and

ii) the electrode surface characteristics e.g. surface finish, coating and contamination. Since however, the microscopic electrode surface state is invariably ill-defined, controlled experiments taking into account all these parameters are almost impossible. Consequently, interpretations of results are complex, and many different hypotheses have been put forward to explain the various processes involved in the initiation of electrical breakdown. Essentially, these hypotheses have been based on two fundamental physical processes. These are

i) the emission of electrons from localised sites on electrode surfaces where the field is assumed to be locally enhanced to such a value that field electron emission can occur and

ii) the concept that charged particles can be detached from an electrically stressed electrode surface resulting in their acceleration across the electrode gap and subsequent impingement on the opposite electrode. The theories associated with these two fundamental processes will now be discussed in more detail in the following sections.

1.2. Electron emission initiated breakdown

It is now a well established fact that if the electric field applied to the surface of a metal exceeds a value $\sim 3 \times 10^9$ Vm^{-1}, the basic condition for the quantum mechanical tunnelling of electrons from the metal into the vacuum is fulfilled. This electron emission mechanism frequently referred to as "cold"

cathode emission, was first analysed theoretically by Fowler and Nordheim (1) who showed that on the basis of a free electron model, the low temperature ($\leq 300^{\circ}K$) field emitted current density J will be given by the relation

$$J = \frac{1.54 \times 10^{-6} E^2}{\phi t^2(y)} \exp - \left[\frac{6.83 \times 10^9 \phi^{3/2} v(y)}{E} \right] \quad \text{---} \quad 1.1$$

where E is the electric field at the surface of the metal in Vm^{-1}

ϕ is the work function of the cathode in eV

t(y) and V(y) are tabulated dimensionless elliptic functions of the parameter y which is related to E and ϕ by $y = 3.79 \times 10^{-5} \frac{E^{\frac{1}{2}}}{\phi}$

By introducing realistic values for ϕ into equation 1.1 it can be shown that a field of $\sim 10^9 V/m$ is required to obtain measurable current densities of around 10^{-13} Amps m^{-2}. The validity of this expression was first demonstrated by Haefer (2) using a micropoint emitter regime which is the only practical way of achieving these high fields under controlled laboratory conditions. It is, however, possible to observe "cold" emission currents, known as prebreakdown currents, with broad area electrodes for externally applied macroscopic gap fields of less than $10^7 Vm^{-1}$. To explain this phenomenon it has been necessary to introduce the concept of local geometric field enhancement at isolated microscopic pointed protrusions on the electrode surface. This effect may be quantified by introducing a dimensionless field enhancement factor β that relates the local

microscopic field at the emitter (Emicroscopic) to the externally applied macroscopic field in the gap such that

$$E_{mic} = \beta E_{mac} \qquad \text{- - - 1.2}$$

If the electron emission originating at these protrusions is excessive then it can lead to electrical breakdown through thermal instability involving melting and vaporisation processes at the surface of the cathode protrusion or at the anode hot spot formed by the bombarding electrons (3, 4, 5): these are respectively referred to as cathode and anode initiated breakdown mechanisms.

Dyke and his colleagues (6) have demonstrated that cathode initiated breakdown in a point to plane diode geometry is caused by the Joulian and Nottingham heating of the cathode tip that is associated with excessive field emission currents. They have also shown that as the electric field at a clean single crystal tungsten - point - cathode is varied, the current flowing to the anode accurately follows the predictions of the Fowler - Nordheim (1) theory for field emission. Alpert et al. (7) have suggested that the same mechanism of arc initiation occurs at the microprotrusions on broad area electrodes as for the laboratory point to plane geometry. In addition they have shown that the current-voltage characteristic of the field emission from such points could be used as a tool to ascertain the field enhancement factor β of such sites and hence predict the voltage at which the breakdown would occur. Their results also give strong support to the fact that breakdown occurs when the local electric field at such microscopic protrusions on the cathode surfaces reaches

a critical value of approximately 10^{10} Vm^{-1} that is independent of the geometry or gap spacing.

The presence of whisker-like projections on a cathode surface that could potentially act as prebreakdown emission sites were first observed by Little and Whitney (8). These projections were shown to have the appropriate geometry for producing the necessary field enhancement for there to be finite field emission at macroscopic electric fields of 10^{7} Vm^{-1}; the threshold field for prebreakdown current. Little and Smith (9) however showed that the small pointed projections on the cathode surface were not present until the application of an electric field and the occurrence of a microdischarge i.e. in agreement with the findings of Van Oostrum (10) who showed that microscopic surface conditions are subject to changes with time, particularly at gap voltages high enough to induce prebreakdown currents. These findings therefore suggested that electron emission could occur from sites where it was not necessary for the external field to be geometrically enhanced.

With this in mind Cox (11) developed a technique for isolating and observing the microtopography of broad area emission sites in situ in an SEM and found electron emission to occur either from grain boundaries or from impurity particles. In addition, Hurley et al. (12) have found that electron emission from these sites is also accompanied by electroluminescence on the surface of copper cathodes following the application of high electric fields. Further, Allen and Latham (13) have shown that the energy spectra of electrons emitted from these sites are untypical of metals and more like that of semiconductors and

insulators. To explain these findings the latter authors have developed a model which is based on the injection of electrons into the conduction band of a semi-conducting/insulating impurity, which are then "heated" by the penetrating electric field to $\sim$ 4-5 eV which is sufficient for them to be emitted over the potential barrier. Hurley (14) on the other hand proposed an alternative model which involved the growth of a conducting filament within the insulating microimpurity that gave rise to an "internal" geometrical field enhancement at the tip, i.e. eliminating the need for an "external whisker". More recently, Athwal and Latham (15) have developed an improved model that is based on the physical regime of an insulating rather than a semiconducting microimpurity that is in intimate contact with the substrate metallic cathode and suggested that the variation of the shift and half width of the energy spectra with the applied macroscopic field and site emission current can be explained in terms of band bending due to the combination of field penetration, space charge effects and surface states. They propose that field penetration in the insulator causes it to "switch" to a high- conductivity state so that there is a rapid re-arrangement of the energy band configuration, with scattering processes in a high field surface region formed by surface states being responsible for the electroluminesence phenomenon.

1.2.1 Cathode versus anode initiated breakdown

The question of whether a breakdown will in fact be cathode or anode initiated has been the subject of several theoretical

analyses. As indicated above, cathode initiated breakdown follows the vaporisation of a microprotrusion when, the thermal balance between the heat generated by the current flowing in the protrusion and that dissipated by conduction and radiation is destroyed. The detailed theory of this breakdown mechanism was first proposed by Dyke and Trolan (6) who using a tungsten-molybdenum-plane geometry similar to that of a field emission microscope obtained values for the critical electric field at breakdown to be $\sim 7 \times 10^9$ Vm^{-1}, which was one or two orders of magnitude higher than that found on more usual electrode geometries. Charbonnier, Bennette and Swanson (16), distinguishing between cathode and anode initiated breakdown, identified the former as being due to the electron beam power density at the cathode becoming critical and the latter as a result of the same power density becoming critical at the anode.

This latter anode initiated breakdown was first studied in detail by Boyle (4) who proposed that the thermal instability is a result of vaporisation of the anode material from localised anode "hot" spots which have been subjected to electron bombardment by electron beams originating from cathode protrusions. This mechanism was subsequently refined and developed more quantitavely by a number of researchers (17, 18) whose conclusion was that the main parameters determining whether thermal instabilities originate at the cathode or anode is the local field enhancement factor β of the emitting cathode protrusions. Thus large β value emitters will lead to cathode initiation whilst low β emitters will give rise to anode initiated breakdown.

1.3. Microparticle initiated breakdown

1.3.1 Clump hypothesis

Since freshly polished electrodes are likely to have numerous micron sized particles loosely embedded in their surfaces, it follows that on the application of an electric field between the electrodes these microparticles will experience strong electro-mechanical forces tending to tear them from the surface. This phenomena of particle detachment from the parent electrode was first proposed by Cranberg (19) who suggested that a charged "clump" or microparticle is accelerated across the gap and strikes the opposite electrode resulting in breakdown if the energy per unit area (W) delivered to the target electrode exceeds some limit C' governed by the electrode geometry. The energy per unit area then becomes the product of the gap voltage V and the charge density (which is proportional to the field E) on the clump. Hence the breakdown criterion becomes $VE \geq C$ where C is a product of C', numerical factors and a field intensifying factor due to the microscopic inhomogeneities. In the case of plane parallel electrodes $E = \frac{V}{d}$, where V is the gap voltage and d the inter-electrode gap. The above criterion predicts that the maximum voltage that will be supported by a gap will be proportional to the square root of the gap separation (d) for a given pair of electrodes so that

$$V \geqq (Cd)^{\frac{1}{2}} \qquad \text{- - - 1.3}$$

Curves of breakdown voltage against varying gap separations for uniform and nearly uniform field conditions showed good agreement with

his hypothesis. Cranberg further used this hypothesis to explain certain qualitative aspects of vacuum breakdown, in particular the conditioning process. He suggested that conditioning was simply the process of detachment of the most loosely adhering material and its firm embedment in the opposite electrode following its acceleration across the gap to a high impact velocity. Cranberg's hypothesis postulating a single transit impact event as an initiation of vacuum breakdown was also used by him to explain the well known sporadic character of breakdown.

Slivkov (20) refined the basic idea of Cranberg by using data obtained from experiments conducted with large electrode gap separations and voltages of the order of hundreds of kilovolts, i.e. where field emission was too low to explain breakdown. He showed that under these conditions the anode material has an effect on the discharge process by virtue of the deposition of fine particles of anode material on the cathode surface. His proposed mechanism for such a discharge assumes the existence of a conducting cloud between the electrodes which is propogated from one electrode to the other. In addition, Slivkov's analysis applied constraints on the particle size whereby an upper and a lower limit was established by the prerequisites that the kinetic energy of the particle be sufficient to vaporise its own mass, and that the gas cloud be large enough to permit charge multiplication. Later investigations into the nature of the damage resulting from the impact of high velocity single-transit microparticles indicated that velocities of the order of 6 Kms^{-1} are required for explosive vaporisation (21) and velocities in

the range 2 - 4 Kms^{-1} for partial vaporisation (22).

Since Cranberg's original proposal, and particularly during the last decade, theories and models concerning the possibility of microparticle induced breakdown have appeared in the literature. As a result, the concept of microparticle induced breakdown has not only become more accepted but also better understood.

1.3.2 Evidence of naturally occurring microparticles

Although there are many reports suggesting the presence of microparticles as a plausible explanation for the breakdown of a high vacuum gap where the gap is > 6mm, it was some time before the validity of this theory could be realistically tested. One of the earliest investigations that could be cited as giving support to Cranberg's theory of material transfer in the form of clumps was due to Anderson (23) who, using dissimilar electrodes, reported the deposition of a brownish substance on the steel cathode identified as copper from the copper anode. More recently, evidence of the presence of sub micron sized particles in a high voltage gap was reported by Menon and Srivastava (24) who, using a shielded collector placed behind perforated (50% transparency) cathodes of differing materials together with electron optical methods of detection observed an abundance of irregularly shaped microparticles made of the electrode materials at voltages which were as low as 30% of the breakdown voltage. In addition, from their experiments on combinations of dissimilar electrode pairs, they suggested that since stainless steel particles could only be observed when the

anode was of stainless steel material, then the cathodic particles must be generated by the impact of anode particles. They did not however, detect large microparticles (>10μm) during the prebreakdown phase, thus suggesting that the breakdown is predominantly due to the micron or submicron sized particles. Such an abundance of micron size particles was not however observed by Chatterton and Birdar (25) or Hurley and Parnell(26) who carried out similar detection studies. This could be due either to the fact that in the case of Hurley and Parnel's work, the optical microscopy detection technique restricted the observable range and size of particles and secondly that many of the weakly adhering particles could have been removed and lost from the gap due to bouncing of the detached particles in the applied electric fields.

More recently, Texier (27) has used a technique which incorporated a semi transparent grid electrode in conjunction with an inflight detection system and has identified naturally occurring microparticles ranging in size from 1 - 8 micron, from abrasively polished unoutgassed electrodes. Rohrbach (28) using a laser-scattering technique has shown that it is possible to make inflight detection of microparticles larger in size than 3 micron. Puiz (29) using a similar technique has observed several events which could be identified as microparticles, whilst Hurley and Parnell (26) using a plastic film interposed between two electrodes have shown the presence of trapped microparticles of diameters 3 - 40 micron. More recently Jenkins and Chatterton (30) using an improved laser technique

were able to observe large numbers of microparticles, particularly at low fields; it is however significant that these did not cause breakdown.

1.3.3 Microparticle induced breakdown mechanisms

Subsequent to Cranberg's original proposal, several other breakdown mechanisms involving microparticles have been proposed. However, it will be seen from the following summary that the type of mechanism that will operate in a given situation is determined by the particle size and impact velocity. It should be noted for the purpose of the following review that the velocity v, of a microparticle accelerated across a gap can be readily obtained from the relation

$$v = \frac{(2QV)^{\frac{1}{2}}}{m} \qquad \text{- - - 1.4}$$

where Q and m are respectively the charge and mass of the particle and V is the p.d. applied across the gap.

The impact velocities of large microparticles ($Rp > 10$ micron) are usually found to be too low ($\lesssim 100\ ms^{-1}$) to cause breakdown as a result of electrode impact damage. However, using artificially generated particles it has nevertheless been shown that breakdown can still be initiated by such larger low velocity microparticles. One process by which this can occur is the trigger discharge mechanism which was originally demonstrated by Olendzkaya (31). She suggested that as a particle approached an electrode, there would be an enhancement of the field between the

electrode and charged conducting particle which may be sufficient for a field emission current to be drawn from the electrode surface to the particle. This may in turn cause thermal instability of the electron bombarded area with the generation of sufficient metal vapour between the particle and the cathode to produce a discharge between them. Such a discharge can then trigger a discharge of the main vacuum gap. Martynov (32) extended this model and proposed that after the initial trigger discharge, the plasma produced extends beyond the electrode-particle interspace, so as to form a positive ion sheath which enhances the field locally and allows a conventional field emission breakdown in the main gap. Chatterton et al. (33) further refined the model and proposed that the trigger discharge caused localised melting of regions on the particle and the electrode so that when the particle bounces back an emission site is formed which can become immediately unstable or at some later time.

From calculations based on the above models Chakrabarti and Chatterton (34) have established that, in practice, particle sizes larger then 50 - 100 micron are required for the onset of the trigger discharge process. This would therefore suggest that this mechanism is only likely to be important in the very rare cases when such large particles exist in the interelectrode gap. A further modification of the trigger discharge hypothesis of Olendzkaya has been proposed by Beukema (35) who proposed that in the case of smaller particles ($\leq$ 10 micron), where the temperature rise of the particles due to electron bombardment will be

too low for instant vaporisation, it is still possible for it to be high enough to melt the surface so that such a particle becomes welded to the electrode on contact. Under these circumstances reflection of the particle becomes impossible and as a result its kinetic energy is converted in a rise of temperature of the clump and a part of the cathode. In addition, if a sufficiently high electric field is applied and the particle is irregular it may act as a source of field emission electrons. Alternatively the charge of the particle may be reversed during impact so that it is drawn off the cathode surface by electrostatic forces leaving some remains of the molten part to be extruded by the field to form emission sites on the cathode.

1.3.4 Simulation studies using artificially generated microparticles

In this context it is relevant to cite two types of experiments. Both use an artificial source of microparticles generated from a vacuum operated dust source gun using a reservoir of micrometre sized powder. These involve

i) an "active" situation whereby high velocity microparticles are injected into a high field test gap and

ii) a more "passive" situation whereby the artificially generated microparticles are fired on to a target surface for impact ionisation studies.

i) Injection experiments

Here, the basic philosophy was to test the validity of the Cranberg-Slivkov theories, by injecting artificially generated high

velocity microparticles into an electrically stressed gap and to observe whether these initiated breakdown events. In one such study by Slattery et al. (22) artificially generated high velocity (up to 5 kms^{-1}) microparticles of known mass, were injected through an aperture in one electrode of a plane parallel electrode configuration. Their findings showed indeed that breakdown events could be correlated with the incidence of microparticles, but that the probability of discharge was much greater for particles with energies and radii in excess of about 0.8×10^{-7} J and 0.9 micron respectively. In addition, they showed that smaller, less energetic particles were capable of initiating discharges at higher voltages and fields and found that there was a definite dependence on the polarity of the applied voltage and thus the polarity of the particles.

A similar study was carried out by Birdar and Chatterton (25) who injected artificially generated carbonyl-iron microparticles (.5 - 3 micron radii) into a cylindrical geometry, electrode system consisting of a fine tungsten wire cathode coaxial with an aluminium anode. They too showed that breakdown events could be initiated by such particles, (although depending on the applied voltage) and verified the existence of a low-energy limit for particles capable of initiating such an event.

ii) Impact ionisation studies

The same type of microparticle dust source gun described above has been used to carry out an investigation into the micro-

cratering and ionisation processes associated with micrometeorite impact. Dietzel et al. (36), using hyper velocity (.2 to 40 kms^{-1}) iron microparticles from a 2 - Mv Van de Graaff accelerator have shown that below 1 kms^{-1} the impacting particle suffers almost no deformation with no plasma being generated. On the other hand they observed complete vaporisation of the particle with particle velocities above ~ 6 kms^{-1}. The formation of free charges by the impact of hypervelocity dust particles on metallic surfaces has also been observed by Friichtenicht (37) and by Auer and Sitte (38). Smith and Adams (39), again investigating the impact of hypervelocity (0.5 - 10 kms^{-1}) iron microparticles with a molybdenum target, found that during impact a plasma was generated where the ions were characteristic of the particle and not the target material. In addition, the charge extracted from the plasma reached a maximum value a few microseconds after impact and subsequently decayed exponentially with a time constant of several microseconds. They further found that the kinetic energy of the incident particle was largely dissipated in a mass of material much smaller than the particle mass and that only a small fraction of this energy was utilized in plasma production.

1.3.5 Energy enhancing particle bouncing hypothesis

From the above discussion it would appear that only high velocity simulated impact studies have been carried out. However, this is not the case as, in a more recent type of study, Brah and Latham (40) have adapted the previously mentioned dust source

microparticle gun to produce low velocity charged microshperes for the purpose of investigating another type of microparticle breakdown mechanism based on a particle bouncing phenomenon. From the theories and mechanisms discussed earlier it can be seen that the requisite for microparticle initiated electrical breakdown is either large diameter low velocity, or small diameter high velocity microparticles derived from large accelerating voltages. However, breakdown has commonly been observed with micron-submicron sized particles ($\lesssim 5$ micron) having low single-transit velocities in an inter-electrode gap of between 1 -2 mm where the accelerating voltages are low, say less then 20kV. Clearly, therefore, there must exist some intermediate mechanism whereby the velocities and hence energies of these microparticles are enhanced to a value where they can precipitate a Cranberg type breakdown event. Such an energy enhancing mechanism was proposed by Latham (41) and is based on a concept that micro-particles bounce between a pair of electrodes. According to his model a microparticle undergoing a bouncing impact from a high voltage electrode could experience both charge and momentum reversal. Thus referring to Figure 1.1 it is assumed that a negatively charged particle originating at say the cathode will be accelerated across the gap to impact on the anode with a sub critical impact velocity. Consequently it will bounce off this electrode with partial momentum reversal, and if at the same time, the charge is also reversed it will be further accelerated back across the gap to gain a velocity v_2, where v_2 is greater than v_1:

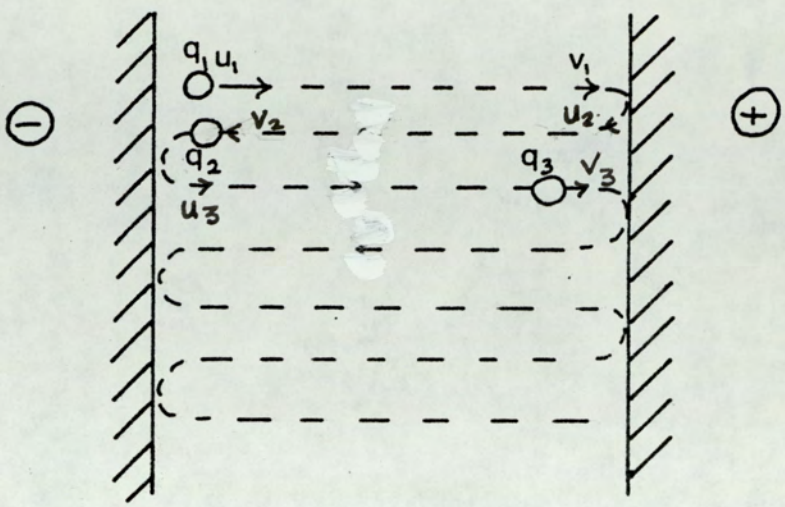

Figure 1.1 : Particle bouncing in an inter-electrode gap

Such a process may be repeated at subsequent impact events as shown. As a result there will be a progressive velocity enhancement until an ultimate impact velocity is attained which is high enough to produce localised melting and vaporisation and thus lead to electrical breakdown. Latham and Braun (42) have suggested that the molten material thus produced will tend to be removed by the applied field. Some will freeze before leaving the surface, while the remainder will be accelerated to the anode as a profusion of sub-micrometre droplets which will subsequently solidify during transit and act as a source of "secondary" microparticles. The condition for $(V_2) > (V_1)$ can be established by using the simple argument that for the particle velocity to be

enhanced after each impact the total energy lost must be less than the total energy gained. Thus if a particle is injected artificially into a gap with an energy q_1 Vo, where Vo is the accelerating voltage and Vg is the gap voltage q_2 is the reversed charge and e is the coefficient of restitution then

$$q_1 \, Vo \, (1 + \frac{Vg}{Vo}) \, (1 - e^2) < q_1 \, Vg + q_2 \, Vg$$

so that $$e^2 > 1 - \frac{q_1 \, Vg + q_2 \, Vg}{q_1 \, Vo \, (1 + Vg/Vo)}$$

giving $$e^2 > 1 - \frac{q_2}{q_1} \left(\frac{Vg}{Vg + Vo} \right)$$

However, for the real situation in a vacuum gap where the particle is initially at rest on the parent electrode Vo is zero so that

$$e^2 > 1 - q_2/q_1$$

1.3.6 Verification of the bouncing hypothesis

The phenomenon of particle bouncing with associated energy enhancement discussed earlier, has been demonstrated by Brah and Latham (40) using the previously detailed simulation technique. In their investigation they found that both the velocity and momentum enhancement, and the charge reversal process, to be strongly dependent on the target electrode material. A commercially polished copper electrode, for example, acted as a more efficient promoter of the charge reversal mechanism than a commercially polished stainless steel electrode (43). Follow up

measurements by Latham et al. (44) have shown that the surface microstructure resulting from the diamond polishing of a metal electrode surface leads to large variations in the localised elastic properties, which would have a significant influence on the behaviour of microparticle bouncing in a real electrode gap. Although previous studies appear to indicate that the microscopic mechanical properties of electrodes play a significant rôle in the energy enhancement mechanism, it has been shown (44) that these are unlikely to play the dominant rôle in controlling the initiation of the type of electrical breakdown event which results from multiple bouncing microparticle impact processes in high field gaps. Rather, they suggested that it is the electrical properties of an electrode surface, through their controlling action on charge reversal mechanisms during the bouncing impact of a microparticle, which is the decisive factor. In a recent study carried out by Latham and Brah (43), which involved in situ surface cleaning techniques, it was found that the removal of the oxide layer greatly enhanced the charge exchange process. Conversely, a thick oxide film on the electrode surface was found to be inhibitive to the reversal mechanism. In addition, they found the efficiency of this mechanism to be strongly dependent on the electrical properties of the surface oxide films.

1.3.7 Objective of investigation

From the preceding discussion, it is clear that there are several well established physical mechanisms which can initiate the

breakdown of a vacuum gap. For small interelectrode gaps of < 1mm, field emission processes appear to be responsible, whilst for larger gaps of 6mm or more it is the impact of high energy microparticles. For the intermediate range, however, more clarification is required, since it is difficult to justify the high field enhancement factors or high energy particles required by the proposed mechanisms of the more conventional theories. On the other hand, the particle bouncing hypothesis offers one plausible explanation for the observed behaviour. However, prior to this investigation, only a very limited amount of direct evidence of its existence was available, consisting mainly of some early data from copper and stainless steel targets using the afore mentioned simulation technique. Accordingly, the major part of the present investigation has been devoted to the study of the energy-enhancing particle bouncing mechanism for an extended range of impact regimes, including differing particle and electrode materials and varying electrode surface preparations e.g. polished, evaporated and "oxide free" surfaces. An important aspect of the study involves a comparison of the impact behaviour of carbonyl iron microspheres on two commercially available alloys of titanium, Ti 318 and Ti 115, since practice has shown that one of these, Ti 318, is widely used as a high voltage electrode material because of its reliable performance.

An equally important aim of these studies is to develop a more complete understanding of the fundamental mechanisms responsible for the actual process of charge reversal. These include the rôle played by the various electrical and mechanical properties

of the electrode surface, for example work function and elasticity together with the influence of the thickness and properties such as band gap and dielectric constants of the surface oxide films present on the target electrode and the impacting microparticle. The rôle of the respective work functions has been investigated by using various combinations of impacting materials, e.g. carbonyl iron or gold microspheres on copper, gold and titanium electrodes. Another important study is concerned with the development of a subsidiary technique, which would enable the measurement of the contact time between the microparticle and target since this is a fundamental mechanical impact parameter.

To complement these experimental findings a theoretical analysis that correlates the mechanical and electrical aspects of the impact process is presented. It includes a review of existing impact theories, and incorporates detailed calculations of the locally enhanced electric field between the microparticle and target. It then goes on to predict theoretical values for the magnitude of charge transferred between the impacting microparticle and target for varying oxide thicknesses, microparticle radii and macroscopic gap fields. However, as will be seen in Chapter 5, agreement between theoretical and experimental values is very variable. Accordingly, discrepancies are interpreted in terms of microscopic properties of the target surfaces.

CHAPTER 2

2.0 Theoretical considerations

In order to interpret the experimental data obtained from the present series of microsphere impact studies, it is necessary to consider the fundamental physical processes that occur at the colliding surfaces. Specifically, these can be conveniently divided into the

i) mechanical interactions and

ii) electrical interactions which respectively control the momentum and charge exchange that occurs during a bouncing event. A further important aim of the analysis is to develop a model incorporating both of these aspects so that it explains the energy-enhancing particle bouncing phenomena which can occur in a high voltage gap and was referred to briefly in the Introduction.

2.1 Mechanical considerations

When two solid surfaces collide, a number of complex processes ranging from deformation of the bodies to plasma generation can take place at the point of impact. It would appear, however, from experiments described in section 1 that severe permanent deformation of the material used is unlikely at microparticle velocities of below $\sim 200 ms^{-1}$. Hence in the present study, where low velocity particles have been used, the impact may be considered to be elastic. In addition, at the point of contact the situation can be considered in terms of adhesion and the relating adhesive forces.

2.1.1 Elastic phenomena

When two solid surfaces come together under dynamic contact pressure it is clear that a number of complex elastic interactions are involved which are critically dependent on the curvature and approach velocity of the surfaces. For the present analysis, we are particularly interested in the factors determining i) the area of contact and ii) the duration of contact. However, when considering the contact area, a distinction has to be made between macro and micro systems so that on the microscopic scale where the curvature of the surface asperities are comparable to the microsurface 'ideal' impact geometry may be considered. Ideally, the microsphere - planar electrode impact regime can be represented schematically as shown in Figure 2.1 where both the sphere and electrode are assumed to have completely smooth surfaces.

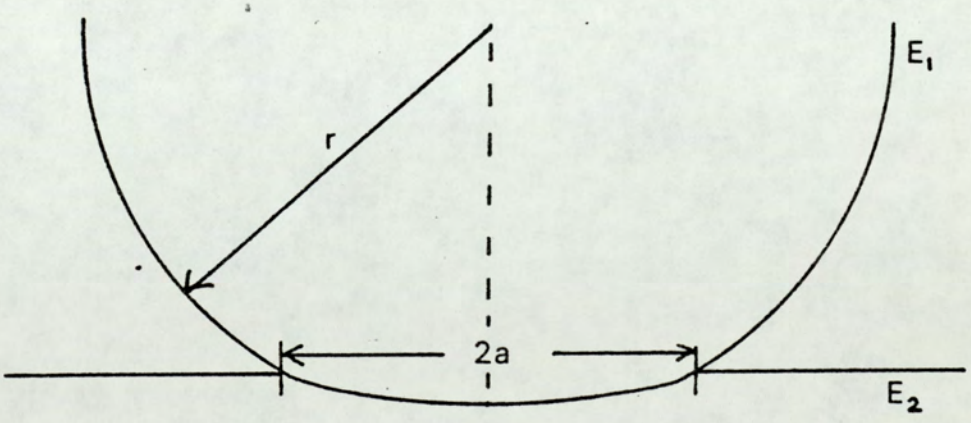

Figure 2.1 : Microsphere/planar impact regime

According to classical Hertzian elastic theory (45) the reversibly deformed contact area for such a regime will be bounded by a circular disc of radius given by

$$a = \left\{ \frac{Wr}{2} \left(\frac{1}{E_1} + \frac{1}{E_2} \right) \right\}^{\frac{1}{3}} \qquad \text{- - - 2.1}$$

where

r = radius of curvature of microsphere

E_1 and E_2 = Young's moduli for the sphere and electrode materials

W = Applied load or mean force transmitted to the target.

It follows therefore that the area of contact $A_c = \pi a^2$ and will be proportional to $W^{2/3}$, whilst the mean pressure Pm over the region of contact will be given by

$$Pm = \frac{W}{\pi a^2}$$

and hence proportional to $W^{\frac{1}{3}}$. The above equation however, can only be used if there is no permanent deformation, i.e. the contact is purely elastic. In practice, as the mean force or load is increased, the elastic limit is first exceeded and the metal becomes plastic and yields irreversibly. In a practical case, such as with a spherical micropoint indentor (111) this sequence will be initiated at the central axial point where the mean force acts normally. However, in neighbouring regions, where the contact pressure is lower, the deformation may still be elastic, so that when the load is removed only a small amount of permanent deformation is left. If the load is increased still

further, the whole of the region of contact flows plastically and the size of the deformed area increases. Tabor (46) states that the transition from a purely elastic contact to one in which some plastic flow may occur, is determined by the criterion that the mean pressure over the area of contact between the spherical indentor and the plane is about 1.1 times the uniaxial yield stress Y of the target material. On the other hand, full plasticity is developed if the mean pressure is $\geq 3Y$.

It is of interest to note that in the case of macro contacting surfaces, such as are relevant to tribological applications, calculations based on the work of Bowden and Tabor (47) have shown that when metal surfaces are in contact, even under small loads ($< 0.1g$), the material around the finer asperities is subjected to stresses exceeding the elastic limit, and in most cases material around the tips of the asperities will be subjected to 'full' plasticity; the mean pressure Pm being given by

$$Pm = cY$$

where

c is a number and depends on the shape and size of the surface irregularities (typically taking a value of ~ 3)

and Y is a measure of the elastic yield stress.

In addition, they suggested that in most practical cases, for all types and shapes of surface irregularities, the real area of contact is very nearly proportional to the load W i.e.

$$a = \frac{1}{p} W$$

where p is a constant of proportionality

Greenwood and Williamson (48) have also found that for a nominal given area, the real area of contact is almost exactly proportional to the load. This is in contrast to the value of a obtained in equation 2.1 for elastic impact where

$$a = \frac{1}{p} W^{2/3}$$

This contradicting evidence has been studied by Archard (49) who points out that plastic deformation cannot be the universal rule and introduces a model which shows that the area of contact can be proportional to the load even with purely elastic contact. However, in the case of a dynamic situation where a metal sphere strikes a plane anvil, both the Hertz theory of elastic impact and theories of inelastic impact (46, 50) recognise that the dynamic yield pressure Pc of a material is a function of the impact velocity. Hence if the impact velocity exceeds a critical value which results in Pc being exceeded, plastic deformation will follow. Tabor predicts

$$Pc = \left(\frac{\pi \rho E^4}{638}\right)^{1/5} v_c^{2/5} \qquad \text{- - - 2.2}$$

Where Vc is the maximum velocity for elastic impact, conventionally defined as the critical velocity.

where ρ is the density

If the impulse imparted by the impacting sphere is assumed to act uniformly over its cross sectional area, the mean pressure exerted during impact will be

$$\bar{P} = \frac{2mv}{\pi r^2 t_c} \qquad \text{- - - 2.3}$$

where v is the impact velocity

where t_c is the duration of contact which, from Hertz theory of elastic impact is given by

$$t_c = 6\left(\frac{15\,m}{16\pi E r^{\frac{1}{2}}}\right)^{2/5} \frac{1}{v^{1/5}} \qquad \text{--- 2.4}$$

which, after substitution for $m = \frac{4}{3}\pi r^3 \rho$ leads to

$$t_c = 6\left(\frac{15}{16\pi E}\,\frac{4\pi r^3 \rho}{3\,r^{\frac{1}{2}}}\right)^{2/5} \frac{1}{v^{1/5}}$$

or

$$t_c = 6\left(\frac{5}{4}\,\frac{\rho}{E}\right)^{\frac{r}{v^{1/5}}} \qquad \text{--- 2.5}$$

This therefore indicates that t_c increases with particle size but decreases with increasing impact velocity. An alternative definition of P_c is available from Hertz's theory which gives an expression for the maximum mean pressure delivered to a target in terms of the impact velocity v, viz.

$$P^5 = \frac{1280}{243\pi^4}\rho v^2 \left(\frac{1}{f(E)}\right)^4$$

Thus P_c will be defined by the condition $v = v_c$, or vice versa

$$P_c = \left[\frac{1280}{243\pi^4}\,\rho v_c^{\,2}\left(\frac{1}{f(E)}\right)^4\right]^{1/5} \qquad \text{--- 2.6}$$

Here $f(E)$ is a function of the elastic constants of the sphere and target materials, given by

$$f(E) \equiv (1 - \nu_1^2) / E_1 + (1 - \nu_2^2) / E_2 \qquad \text{-- 2.7}$$

where ν is poisson ratio

Equation 2.6 hence indicates that the critical pressure depends

solely on the elastic constant, density and velocity of the microsphere and is independent of its size.

Considering now an elastic impact, the contact time te of a spherical particle against an elastically deforming plane will be given by equations 2.4 or 2.5 from which Hutchings (51) derives the time taken for the contact pressure to reach its maximum to equal half the total contact time so that

$$t_{ce} = 1.47 \left(\frac{5\pi}{4}\right)^{2/5} \rho^{2/5} \frac{r}{v^{1/5}} \left(f(E)\right)^{2/5} \quad \text{--- 2.8}$$

and the chordal radius at the end of this time to be

$$a_e = \left[1.25 \pi \rho f(E)\right]^{1/5} r\, v^{1/5} \quad \text{--- 2.9}$$

On the other hand for plastic impact the contact time tp based on the same assumptions as Andrew's work has been shown by Tabor (52) to be

$$t_{c\rho} = \frac{\pi}{2} r \left(2\rho / 3P\right)^{\frac{1}{2}} \quad \text{--- 2.10}$$

where P is the mean pressure acting on the sphere i.e. over the area of contact πa^2

and the radius at the end of time $t_{c\rho}$ to be

$$a_\rho = 2^{\frac{1}{2}} r\, v^{\frac{1}{2}} \left(\frac{2\rho}{3p}\right)^{\frac{1}{4}} \quad \text{--- 2.11}$$

Equation 2.8 derived by Hutchings for the period where impact is elastic indicates that the contact time is proportional to the radius of the particle and varies only slowly with the velocity. If plots of contact time against the velocity for various radii of microspheres are plotted for both the elastic and plastic impact the

following relationships are observed.

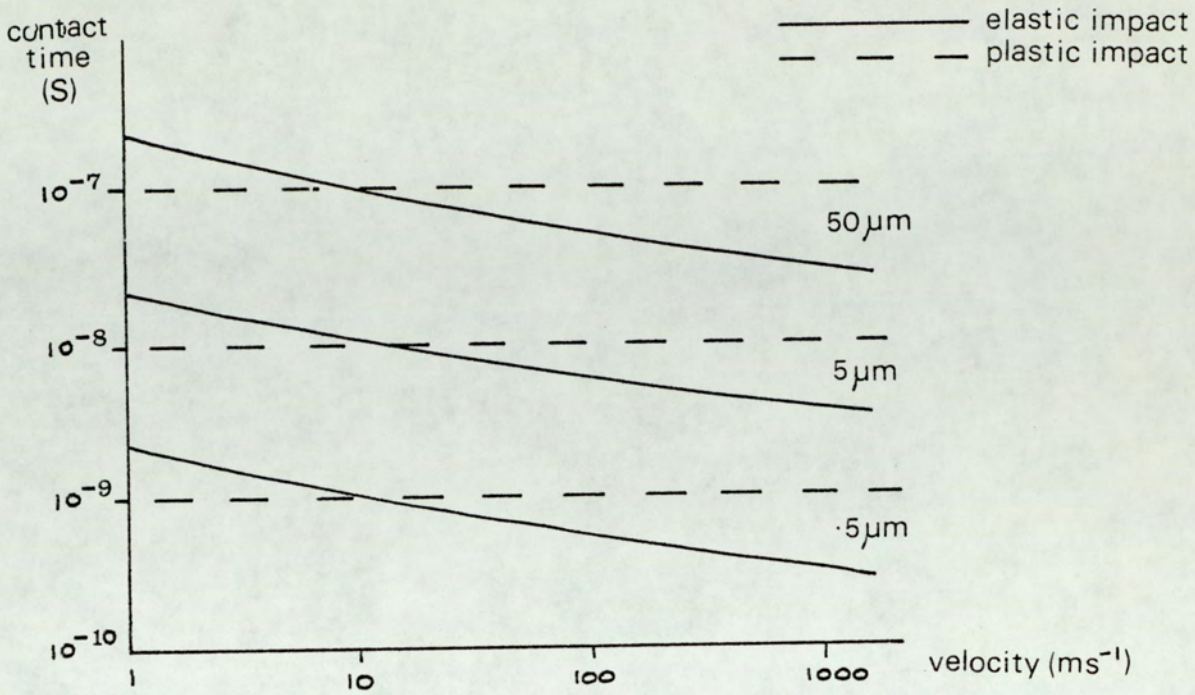

Figure 2.2 : Variation of contact time with impact velocity

In the case of the present study where microparticles of between 1 - 10 micron and velocities of between 10 - 120 ms^{-1} have been employed, it would appear that the contact time is of the order of $\simeq 10^{-8}$ s whether or not the impact is either elastic or plastic.

2.1.2 Adhesion of solids

If two perfectly smooth surfaces are brought together it is found that there is generally an attractive force between them that increases as their separation decreases towards final intimate contact. The finite force required to separate them is normally described as the adhesive force or more simply as the adhesion. This force of adhesion however has been shown to be

critically dependent on

i) the surface roughness (47, 53) and

ii) the presence of surface films such as oxides (54, 55, 56)

Thus Fuller and Tabor (59) studied the strength of adhesion as a function of the surface roughness and found that relatively small surface irregularities are sufficient to reduce the adhesion to a very small value. On the other hand, the earlier work of Holm (54) and Shaw and Leavey (55) has shown that strong adhesion may occur between surfaces which have been completely freed of adsorbed surface films, but if the surfaces are exposed to air no adhesion is observed. Two approaches have been adopted to explain the physical basis of adhesion:-

i) in terms of surface chemistry, where adhesive forces are correlated to Van der Waal's forces between surface atoms and

ii) using the energy balance concept (57, 58) which is based on optimising the total energy of the system at equilibrium, where the adhesive force is derived by equating the first derivative of the total energy to zero.

2.1.3 Adhesion due to Van der Waal's forces

Most combinations of solid surfaces normally experience adhesion due to Van der Waal's forces resulting from interactions between atoms below the surface layers (46). From closer studies of this type of adhesion Tabor and Winterton (59) found a change in the nature of Van der Waal's forces which was dependent on the separation of the two metals. They observed the existence of "ordinary" Van der Waal's forces for gap separations of $< 100^{\circ}$ A and "retarded" Van der Waal's forces for separations of $> 100^{\circ}$ A. On considering the force between two solid bodies separated by a small gap, the ordinary Van der Waal's force F_o for a plane - sphere situation as illustrated in Figure 2.3 was given by

$$F_o = \frac{A R}{6 h^2} \qquad \text{--- 2.12}$$

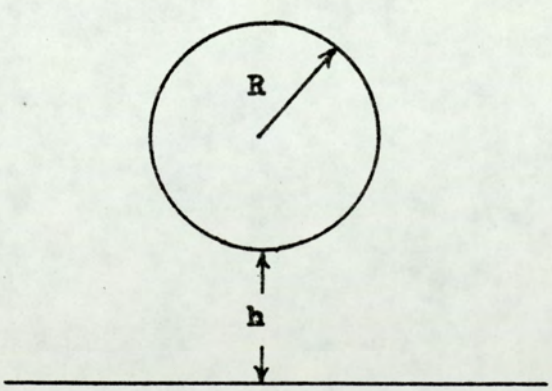

Figure 2.3 : Plane/sphere seperation

where h is the distance between sphere and plane at the point of closest approach, and

A is the Hamaker constant which normally has the value $A = \pi^2 m^2 L$: numerically, this can vary between $\sim 10^{-19}$ J for Van der Waal solids to 10^{-18} J for metals (52). Considering a gap separation of 100° A and a microsphere of radius $5\mu m$ a numerical value of 8×10^{-9} N for the ordinary Van der Waal's force is obtained. For separations of $>100^{\circ}$ A the retarded Van der Waal force F_R, again for a plane - sphere situation is given by

$$F_R = \frac{2\pi B R}{3 h^3} \qquad \text{---} \quad 2.13$$

where B is the retarded Van der Waal constant and has a value of $\simeq 10^{-26}$ J.

Considering a microsphere of the same dimensions as above and a gap separation of 200° A a numerical value of $\sim 13 \times 10^{-9}$ N for the retarded Van der Waal force is obtained.

Hence it would appear that the two types of Van der Waal forces have comparable values for the range of gap separations considered. In practical terms, this therefore implies that a particle approaching within 200° A of a plane will experience an approximately constant force.

2.1.4 Energy balance approach

Since calculations of the adhesive forces between more detailed surface regimes is generally very complex, an alternative approach based on a surface energy concept has been introduced by Kendall (57) and Johnson et al. (58). According to their theory every surface

can be characterised by having a certain free surface energy resulting from the action of surface forces due to decreased bonding of the surface atoms and analogous to surface tension so that when two surfaces come together they will experience an attractive force which, although of little significance at high loads, becomes increasingly important as the load is reduced to zero. Thus according to Johnson et al. when two surfaces having surface energies of γ_1 and γ_2 come into contact under zero load, there will be a contact area A whose dimensions will be determined by the energy balance between the stored elastic energy around the interface and that released as a result of the replacement of two free surfaces by a solid - solid interface of lower surface energy. This energy deficit will then be given by $A\Delta\gamma$ where $\Delta\gamma$ can be obtained from the Dupré equation

$$\Delta\gamma = \gamma_1 + \gamma_2 - \gamma_{12} \qquad \text{- - - 2.14}$$

here γ_{12} is the surface energy of the solid - solid interface.

Johnson et al.[58] have also shown that in addition to a finite area of contact for zero joining load there is a finite pull-off force which is independent of the initial joining load. In the case of a sphere-plane regime its value is given by

$$F_d = \frac{3}{2}\pi r \Delta\gamma \qquad \text{- - - 2.15}$$

where r is the radius of the sphere. Johnson et al. (58) found F_d to be of the order of several millinewtons when using optically smooth rubber spheres and rubber flats. Gane et al. (60) found similar results for Fa when using rubber surfaces where

$\gamma_1 = \gamma_2$, $\gamma_{12} = 0$, $r = 22$ mm and $\gamma_{rubber} \simeq 30 mJm^{-2}$.

On the other hand experiments carried out by them on hard elastic solids such as titanium carbide having clean surfaces revealed an absence of any appreciable adhesion with values for F_a ranging from $50\mu N$ to $100\mu N$. They failed to increase the adhesion even after a variety of cleaning techniques such as argon ion bombardment. Similar results were obtained by Pollock et al. (61) from measurements on platinum and tungsten where he found F_a to be $\sim 80\mu N$.

The relation between adhesion and ductility has also been studied by many workers (62, 63, 64) and in particular by Gane et al. (60) who found that for non ductile solids the effect of submicroscopic surface roughness was to make the adhesive force much smaller than would be expected for a given value of $\Delta\gamma$. This can be explained partly in terms of a reduced contact area resulting from the presence of a few high asperities which prevent contact with the lower asperities and so reduce the total adhesion and partly due to the fact that with non ductile metals the energy to pull the surfaces apart involves very little plastic work, thus increasing the value of γ_{12}. From equation 2.14 it can be seen that if γ_{12} is increased $\Delta\gamma$ is lowered and thus from equation 2.15 the adhesive force is lowered. On the other hand if materials are very ductile the junctions may undergo considerable plastic deformation during pull off (i.e. some of the elastic energy stored during contact is dissipated on unloading by plastic flow), thereby lowering the value γ_{12} and hence increasing the adhesive strength per unit area of contact.

In practical terms this would therefore indicate that in the present regime where the combination of surfaces used are i) iron - titanium 115/titanium 318 ii) iron - gold iii) iron - copper iv) gold - titanium 115/titanium 318 v) gold - gold vi) gold - copper; wide variations in the adhesive forces could be expected. For combinations (iii) to (vi), which include a ductile material, the adhesive force would be expected to be lower than that for combination (i).

2.2 Electrical considerations

When the separation between two vacuum - insulated metal surfaces of work functions ϕ_1 and ϕ_2 approaches atomic dimensions, say $\leq 100^{\circ}$A, charge can be transferred between them by electron tunnelling; the current flowing from the metal with the lower work function to that with the higher work function. It is in fact this phenomena that gives rise to the contact potential difference. If however an external bias voltage is applied between the two metals, the tunnelling process will either be augmented or suppressed, depending on the polarity of the bias. Considering now the impact regime of the present investigation where as shown in Figure 2.4, a charged microsphere initially at some potential V_p with respect to the target electrode, and surrounded by its ambient oxide layer of thickness $\sim 50^{\circ}$ A comes into close contact with an anvil also covered by its ambient oxide layer of similar thickness, it is evident that a close analogy exists with the above system, except that the insulating medium is no longer vacuum. For this more complicated case it is necessary to take

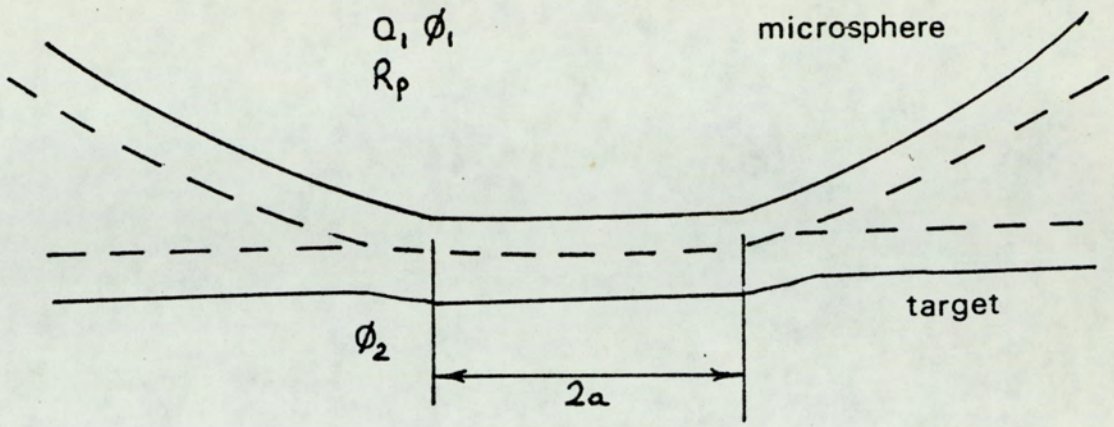

Figure 2.4 : Microsphere / Target seperation with the presence of the ambient oxides

account of the electrical properties of the insulating media such as the bandgap and the dielectric constants of the respective surface oxides.

A fundamental expression for the tunnelling current density that will be applicable to the experimental regime of Figure 2.4 will be derived. However to explain the underlying physical concepts the simpler case of vacuum insulating media will first be considered.

2. 2. 1 Metal - Vacuum - Metal tunnelling (MVM)

It is a well established fact that from Sommerfeld's free-electron theory a metal can be viewed simply as a potential box with say N electrons that fill the available energy levels up to $\eta_f = N/2$ called the Fermi level. (Figure 2.5) (This is a consequence of Pauli's principle, which states that only two electrons as a result of the electron spin can occupy any energy level). The energy of an electron at rest outside the metal is normally used as a reference and is referred to as the vacuum level, whilst the energy required to remove an electron from the Fermi level in the metal will be $e\phi$ where ϕ is defined as the work function and has the units of potential

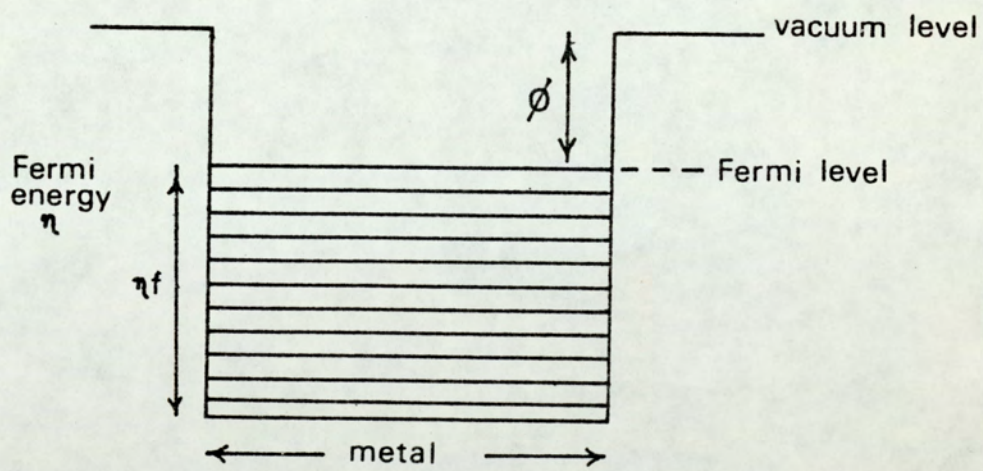

Figure 2.5 : Potential box model of atom

Since the Fermi levels for two metals in thermal equilibrium must be in coincidence (65), it follows that in the case of metals having similar ϕ values and separated by a distance S their

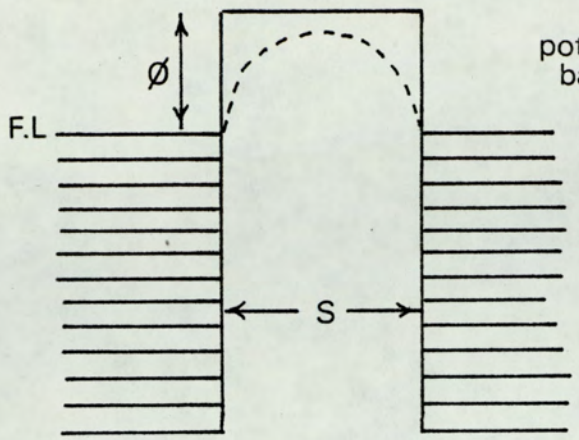

Figure 2.6 a

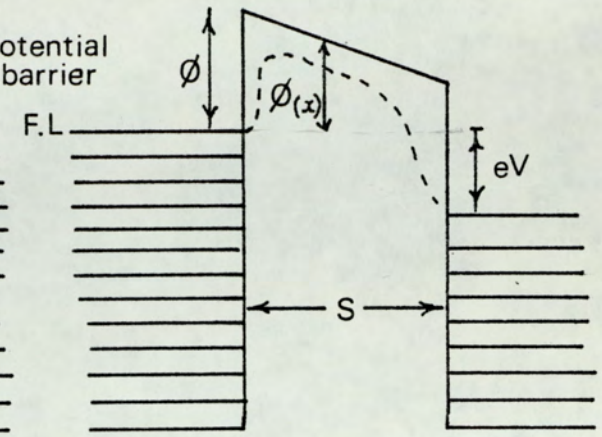

Figure 2.6 b

vacuum levels must also be in coincidence as illustrated in Figure 2.6 a.

Hence a potential barrier of width S and constant height ϕ above the Fermi levels will exist between the two electrodes. If now an external potential difference V is established between the electrodes the Fermi levels separate by an energy eV, with the Fermi level of the negatively biased - electrode moving upwards to a higher energy state. As illustrated in Figure 2.6 b the height of the potential barrier ϕ_x is now trapezoidal in shape (continuous lines) and is a linear function of the distance within the barrier given by

$$\phi(x) = \phi - e V x / S \qquad \text{- - - 2.16}$$

The effect of the image force is to reduce the total area of the

potential barrier between the electrodes by rounding off the corners and reducing the height and width of the barrier. This is illustrated by the dotted lines in Figures 2.6 a and 2.6 b for the case of zero - biased electrodes and where there is an external bias.

2.2.2 Metal - Insulator - Metal tunnelling (MIM)

The action of an insulating media between two closely spaced electrodes is one of lowering the potential barrier that exists between them since equilibrium conditions require that the bottom of the conduction band of the insulator be positioned above the the Fermi level and below the vacuum level of the electrodes. Thus the potential barrier is lowered by an amount $\phi - \Psi$ where Ψ is the potential difference between the bottom of the insulator conduction band and the Fermi level of the metal electrodes. This situation is illustrated in Figure 2.7 for the case of two electrodes of similar material

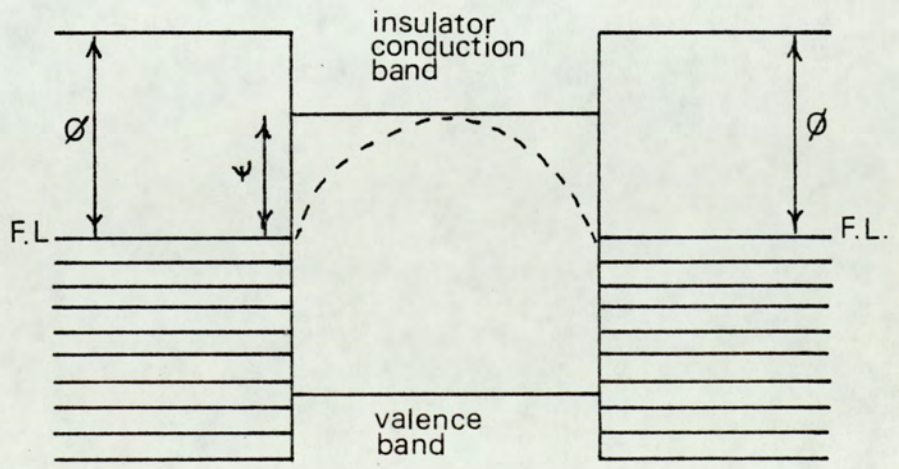

Figure 2.7

Ψ is now referred to as the barrier height at the interface of the electrode and insulator. Again the image force set up in the interspace is shown by the dotted line.

Consider now the case where the two electrodes are of different materials so that their respective work functions are ϕ_1 and ϕ_2. If two such isolated electrodes are initially brought into close proximity the situation will appear as in Figure 2.8a where there is a difference in the Fermi levels $\phi_2 - \phi_1$.

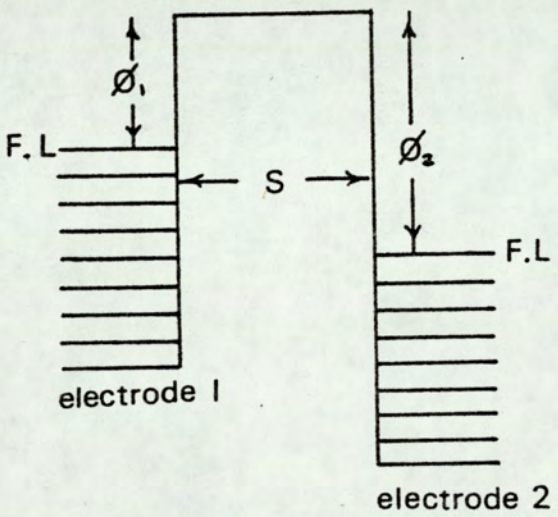

Figure 2.8a

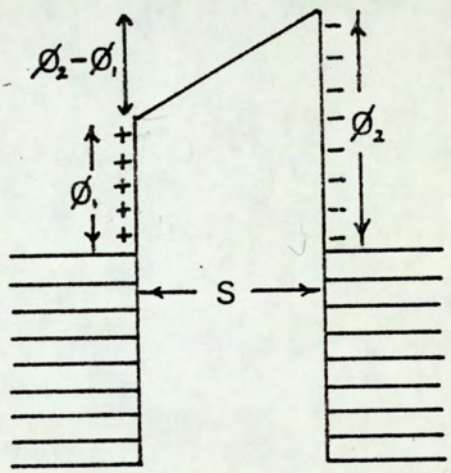

Figure 2.8b

Assuming now that the separation S is small enough for tunnelling to take place, there will be a net flow of electrons from electrodes 1 to 2 until the Fermi levels have been equalised as shown in Figure 2.8 b. Thus electrode 1 will become positively charged with respect to electrode 2, with an equilibrium p.d. $\phi_2 - \phi_1$, existing between them. This is commonly referred to as the contact potential and as a result, an extremely high intrinsic field E_i is established within the film. The

magnitude of this field is given by

$$E_i = \frac{\phi_2 - \phi_1}{S} \qquad \text{- - - 2.17}$$

where S is the thickness of the insulating film in Angströms.

As illustrated in Figure 2.8 b the height of the barrier is no longer constant but trapezoidal in shape, so that its heights at the metal - insulator interfaces are no longer equal but related as follows,

$$\begin{aligned} \Psi_2 &= \Psi_1 + E_i S \\ &= \Psi_1 + \phi_2 - \phi_1 \\ &= \Psi_1 + \Delta\phi \end{aligned}$$

The height of the barrier $\Psi(x)$ between the electrodes is now given by

$$\Psi(x) = \Psi_1 + (\Delta\phi x / s)$$

If however this arrangement is connected to a circuit containing an external bias voltage so that the imposed external field E_e acts in the same direction as the intrinsic field E_i the device is said to be reverse biased (66). On the other hand when E_e opposes E_i a situation of positive or forward bias exists. It must also be noted that the barrier shape will also be dependent on the external voltage.

2.2.3 The effect of differing bias voltage on the barrier shape

As mentioned previously, the effect of an external bias voltage on two similar electrodes is to alter the horizontal barrier existing at zero bias to a trapezoidal barrier. According to Simmons (67) the exact shape of this new asymmetric barrier will depend on the range of the external voltage. Figures 2.9 a, b and c illustrate the idealized barrier shapes in the absence of image forces for similar electrodes at i) zero bias ii) intermediate voltage and iii) high voltage.

From these diagrams it can be seen that whilst the slope of the barrier increases with increasing voltage, the effective tunnelling distance for electrons at the Fermi levels of the two electrodes remains constant for low and intermediate bias situation. However at higher biasing, and as shown in Figure 2.9c it will be seen that the bottom of the conduction band of electrode (2) becomes lower than the Fermi level of electrode (1), thus effectively reducing the tunnelling distance from S to $\triangle$ S. Under such circumstances there would be a rapid increase in the tunnelling current from (1) into the empty conduction band of (2).

In the case of dissimilar electrodes whilst the external bias changes the shape of the barrier at low and intermediate voltages there are still no polarity effects since the tunnelling width again remains constant. However the situation at high bias is different as illustrated in Figure 2.9 c where the slope shape of the barrier reverses at some particular voltage indicating a polarity dependent situation. Figures 2.10 and 2.11 illustrate

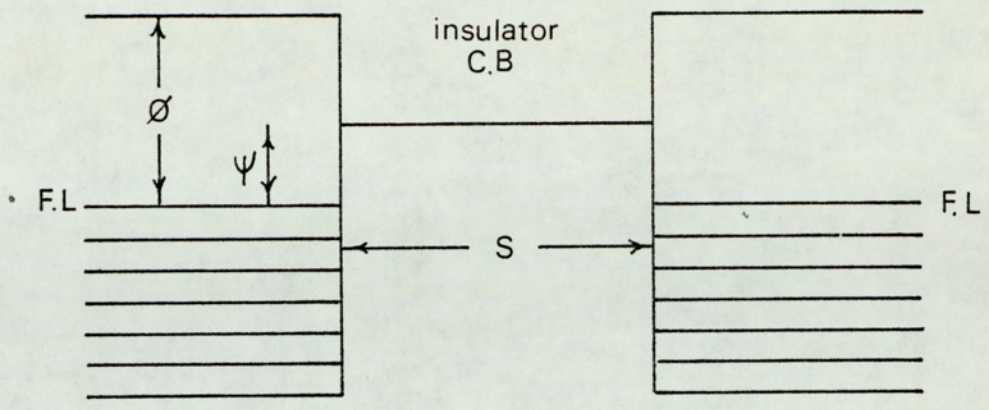

Figure 2·9a : zero voltage V = O

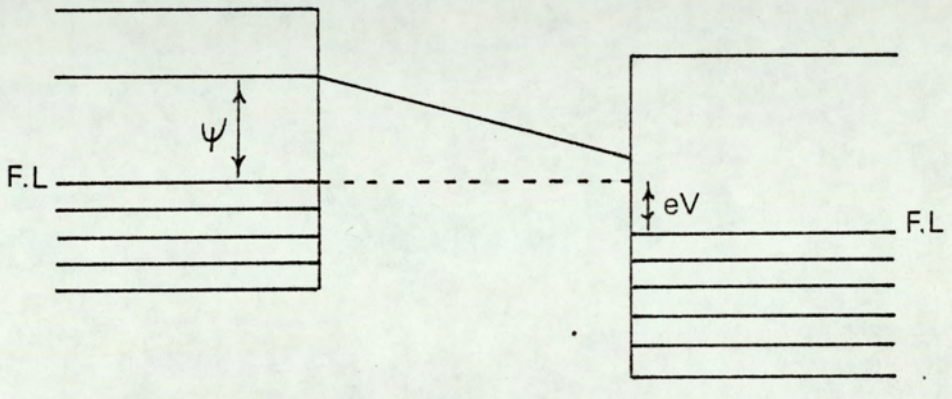

Figure 2·9b: intermediate voltage $V < \Psi/e$

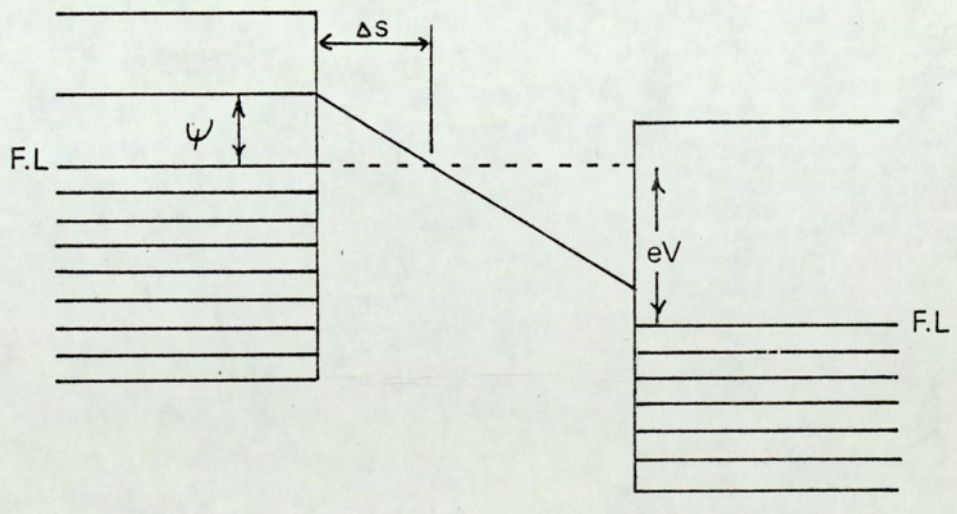

Figure 2·9c: high voltage $V > \Psi/e$

the barrier shapes for the 'forward' and 'reverse' bias situations of two dissimilar electrodes for the cases of intermediate and high voltage range, where the dotted lines represent the barrier shape prior to the application of an external bias.

INTERMEDIATE VOLTAGE

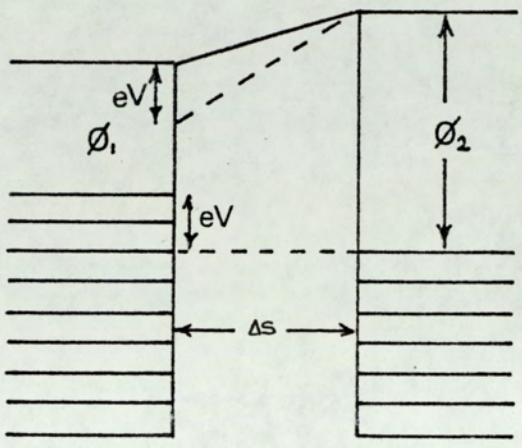

reverse bias

Figure 2.10a

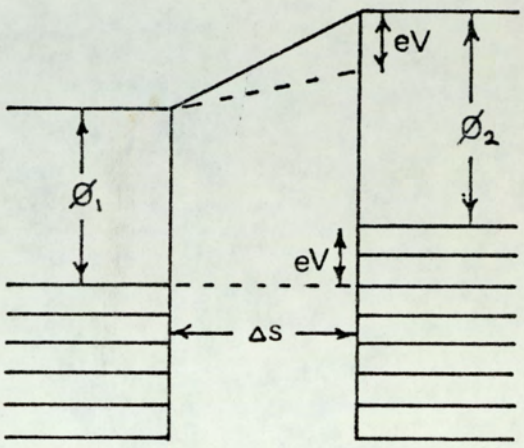

forward bias

Figure 2.10b

HIGH VOLTAGE

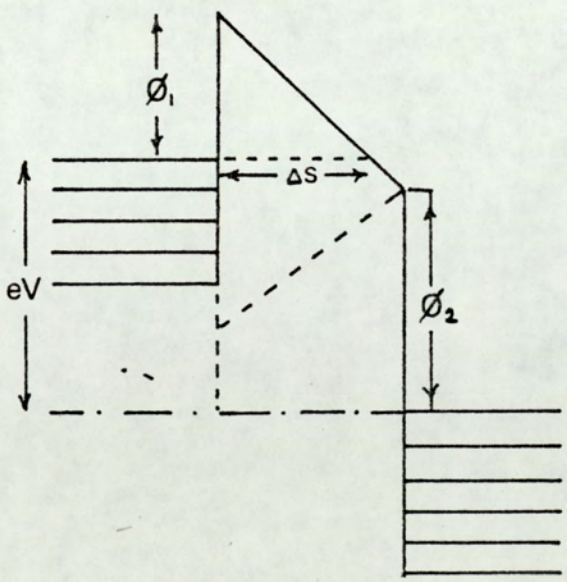

reverse bias

Figure 2.11a

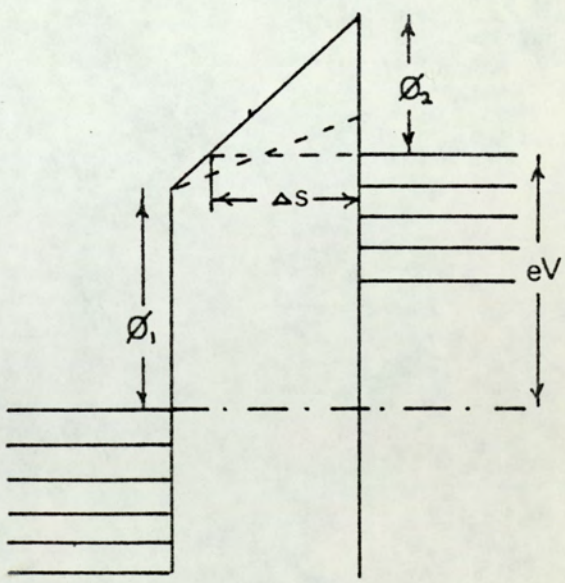

forward bias

Figure 2.11b

2.2.4 Variation of tunnelling current density with the applied voltage

From the Richardson - Dushman equation, the current flowing across a plane metal - vacuum interface is given by

$$J = A T^2 e^{-\phi / K T}$$

In the case of two - electrode system it is necessary to consider the current flow in both directions, since the electrodes are at the same temperature thus the net flow of current will be $J = A T^2 (e^{-\Psi_1/KT} - e^{-\Psi_2/KT})$ where Ψ_1 and Ψ_2 are the maximum barrier heights above the Fermi level of the negatively biased and positively biased electrodes respectively. Hence when the electrodes are at the same potential, the barrier height seen from either electrode is the same and the net current flow is zero, but when a potential V exists between them, so that

J becomes -

$$J = A T^2 e^{-\Psi_1 / K T} \left\{1 - e^{-e v / K T}\right\}$$

Developing these concepts Simmons (68) derived the following generalised expression for the tunnel current density J for a tunnel junction having similar electrodes.

$$J = J_o \left\{ \left[\bar{\Psi} \exp\left(-A\bar{\Psi}^{-\frac{1}{2}}\right) - \left(\bar{\Psi} + e V\right) \exp\left[-A\left(\bar{\Psi} + e V\right)^{\frac{1}{2}} \right] \right] \right\}$$

--- 2.18

and $J_o = e / 2 \pi h (\beta \Delta s)^2$

$A = 4 \pi \Delta s (2m)^{\frac{1}{2}} / h$

Δs is the width of the barrier at the Fermi level of of the negative electrode.

$\bar{\Psi}$ is the mean barrier height above the Fermi level of the negative electrode.

m is the electron mass

β is a function of the barrier shape

h is Planck's constant

The J - V characteristic for junctions with dissimilar electrodes and with image forces neglected were derived by Simmons (69) using the generalised formula. At the intermediate voltage where $0 < V \leq \Psi/e$ it is necessary to study the current flow in either direction since the barrier is asymmetric. Considering the flow of current for the reverse bias situation of Figure 2.10 a where the mean barrier height is given by

$$\bar{\Psi} = (\Psi_1 + \Psi_2 - e\,V)/2 \quad \text{and} \quad \Delta s = s$$

then the current density J_1 will equal

$$J_1 = \left(\frac{e}{4\pi h(\beta s)^2}\right)\left\{\left[(\Psi_1+\Psi_2-eV)\times\exp\left[-\left(\frac{4\pi s m^{\frac{1}{2}}}{h}\right)(\Psi_1+\Psi_2-eV)^{\frac{1}{2}}\right]\right.$$
$$\left. - (\Psi_1+\Psi_2+eV)\times\exp\left[-\left(\frac{4\pi s m^{\frac{1}{2}}}{h}\right)(\Psi_1+\Psi_2+eV)^{\frac{1}{2}}\right]\right\}$$

--- 2.19

For the forward bias situation illustrated in Figure 2.10 b the mean barrier height is again equal to $\bar{\Psi} = (\Psi_1+\Psi_2-e\,V)_2$ and $\Delta s = s$, thus indicating that the current density J_2 must be identical to J_1. This would appear to qualify the earlier concept of the J - V characteristic for a trapezoidal barrier at intermediate voltage being independent of bias polarity.

For the case of high voltages and considering initially the inverse bias situation of Figure 2.11 a where, $\bar{\Psi} = \Psi_1/_2$

and $\Delta s = s\Psi_1 / (e V - \Delta\Psi)$

the current density J_1 is given by

$$J_1 = \frac{1.1e(eV-\Delta\Psi)^2}{4\pi h\Psi_1 s^2}\left\{\exp\left[\left(-\frac{23\pi m^{\frac{1}{2}}}{6h}\right)\left(\frac{s\Psi_1^{\frac{3}{2}}}{eV-\Delta\Psi}\right)\right]-\left(1+\frac{2eV}{\Psi_1}\right)\right.$$
$$\left.\times\exp\left[\left(-\frac{23\pi m^{\frac{1}{2}}}{6h}\right)\left(\frac{s\Psi_1^{\frac{3}{2}}\left[1+(2eV/\Psi_1)\right]^{\frac{1}{2}}}{eV-\Delta\Psi}\right]\right]\right\} \quad -- 2.20$$

In the forward bias situation however, $\bar{\Psi} = \bar{\Psi}_2 / 2$ and $\Delta s = s\Psi_2 / (e V - \Delta\Psi)$ giving a current density value J_2 of

$$J_2 = \frac{1.1e(eV+\Delta\Psi)^2}{4\pi h\Psi_2 s^2}\left\{\exp\left[\left(-\frac{23\pi m^{\frac{1}{2}}}{6h}\right)\left(\frac{s\Psi_2^{\frac{3}{2}}}{eV+\Delta\Psi}\right)\right]-\left(1+\frac{2eV}{\Psi_2}\right)\right.$$
$$\left.\times\exp\left[\left(-\frac{23\pi m^{\frac{1}{2}}}{6h}\right)\left(\frac{s\Psi_2^{\frac{3}{2}}\left[1+(2eV/\Psi_2)\right]^{\frac{1}{2}}}{eV+\Delta\Psi}\right]\right]\right\} \quad -- 2.21$$

Thus for the case of dissimilar electrodes at high bias voltages since $J_1 \neq J_2$ it follows that not only is the J - V characteristic asymmetric with polarity but the direction of rectification reverses at some particular voltage as illustrated earlier in Figure 2.11 b. These results have been summarised by Simmons (69) by means of σ - V curves where σ is the tunnelling resistivity and is equal to V / J. Figure 2.12 illustrates σ as a function of V for gap widths s = 20, 30 and 40°A, Ψ_1 = 1 V, Ψ_2 = 2 V, $\Delta\Psi$ = 2 V. The reverse and forward directions are depicted by the full and dotted lines respectively.

Several features apparent from the curves are

i) at very low voltages the curves are almost horizontal indicating that the junction resistance is ohmic and

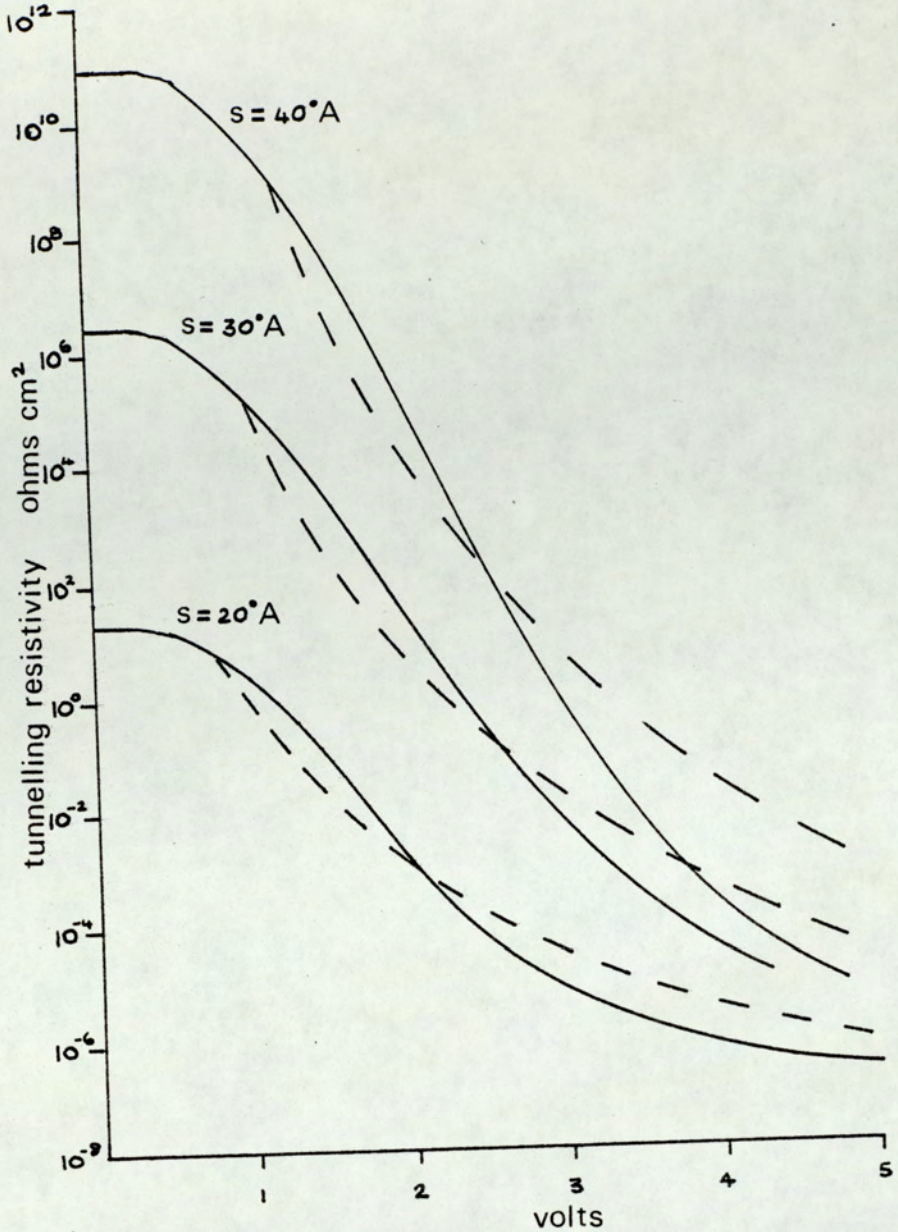

Figure 2.12 : Theoretical σ-V characteristics for an ideal barrier

ii) the tunnelling resistivity falls off rapidly with increasing bias voltage with the effect being more pronounced with thicker insulating films.

Finally it can be seen that the asymmetry of the function characteristics increases with increasing s and the characteristics interesect at approximately the same value of V for all values of s.

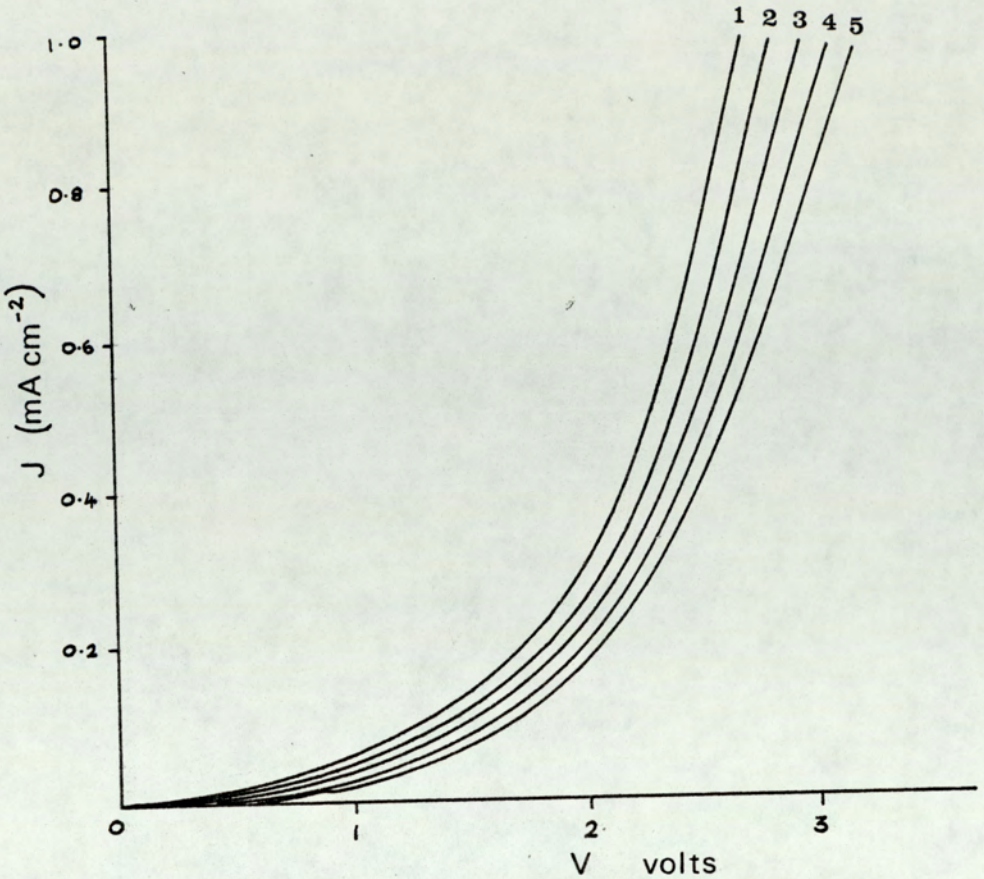

Figure 2·13a : forward characteristics for asymmetric junctions

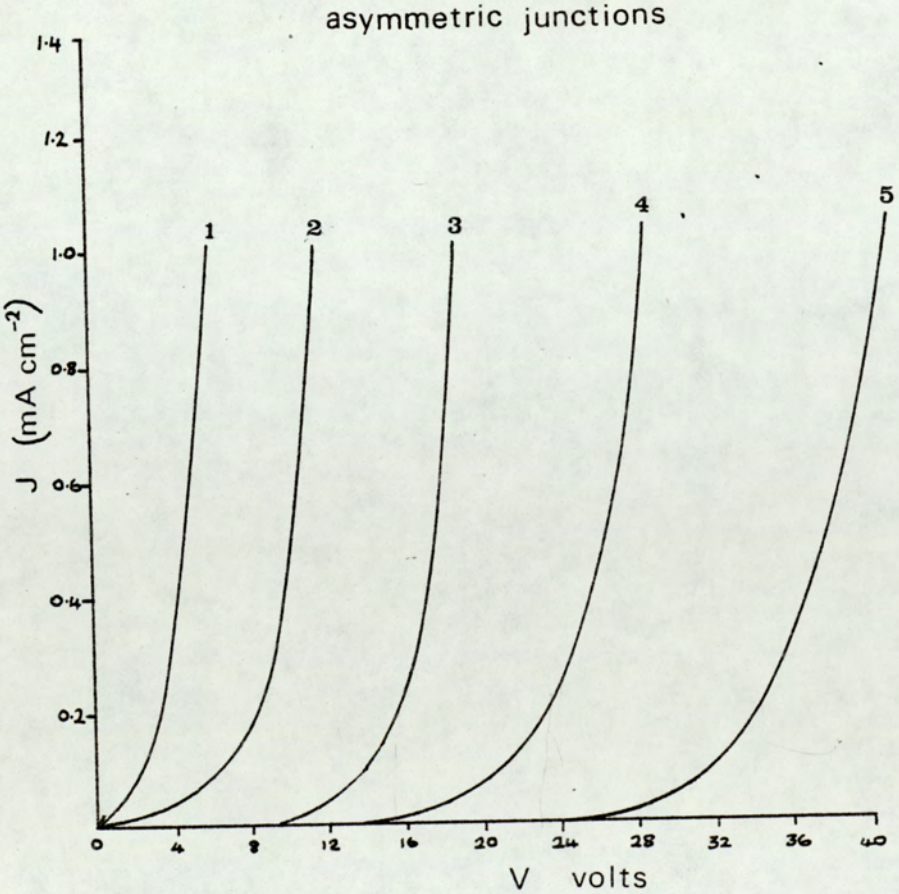

Figure 2·13b : reverse characteristics

Figures 2.13 a and 2.13 b illustrate respectively the forward and reverse characteristic for approximately five asymmetric junctions where $\Delta \phi$, the work function difference between the electrodes comprising a junction, varies from 0.1 to 0.5 e V for which $\Psi_1 = 0.5$ e V, $S = 200$ A$^{\circ}$ and $K = 5$.

From these plots it can be seen that this set of junctions generates a family of parallel curves where the displacement between any two of the family of curves along the voltage axis is equal to the difference between the work functions of the two counter electrodes of the junctions, the work functions being expressed in volts (70). In addition it can be seen that both forward and reverse J - V characteristics are asymmetric and exhibit good rectifying properties. These results have been found to be in good qualitative agreement with the experimental results of Standley amd Maissel (71). The significance of these findings to the present regime will be returned to in Chapter 5, where the experimental results will be discussed.

2.3.0 Field calculations

From the previous discussion it is evident that the tunnelling current and magnitude of charge exchanged between two metal electrodes in a M - I - M junction is predominantly dependent on the microscopic field between them. Since the microparticle - target electrode regime of the present study is analagous to such a junction the derivation of the microscopic field E_g existing between the microparticle and the target electrode is of great

importance. A review of such field calculations carried out by various researchers (24, 35, 72) will now follow.

The evaluation of the microscopic field was first carried out by Martynov[72] who restricted his calculations to the special conditions operating with the trigger discharge mechanism, where large particles of radii $\geq 10\mu m$ and large approach distances were considered. His model employed the idealised geometry of a charged conducting sphere approaching a charged plane such as shown in Figure 2.14.

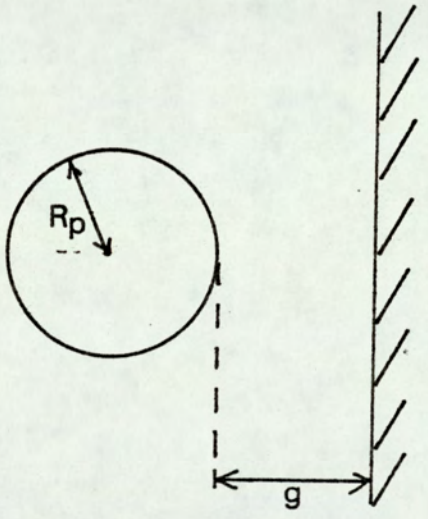

Figure 2.14 : Sphere / plane geometry

The microscopic field E_g can now essentially be taken to be the resultant of a component E_1 arising from the local enhancement of the macroscopic field E due to the presence of the microparticle and a component E_2 arising from the actual physical charge Q_p on the particle. The evaluation of E_1 and E_2 is a standard electrostatic problem involving the solution of Laplace's equation (73) and the application of image theory and

were analysed in detail by Martynov (72) who obtained the following relation for the variation of E_g with gap separation g

$$E_g = E_1 + E_2$$
$$= E f_1 (g / R_p) + E_s f_2 (g / R_p) \quad \text{--- 2.22}$$

Here E is again the uniform macroscopic field and E_s the field intensity at the surface of the charged particle in the absence of E and the conducting electrode, viz.

$$E_s = \frac{Q_p}{4\pi \varepsilon_o (R_p)^2}$$

In equation 2.22 f_1 and f_2 are geometric functions that determine how the proximity of a conducting electrode influences E_1 and E_2. At close distances of approach ($g \sim R_p$) they increase rapidly and for $g / R_p \leq 0.3$, which is relevant to the present study, can be approximated by

$$f_1 \simeq \pi^2/6 \quad \text{and} \quad f_2 \simeq 1.29 \left(\frac{Rp}{g}\right)^{0.8}$$

so that equation 2.22 becomes

$$E_g = 1.29 \left(\frac{R_p}{g}\right)^{0.8} \left[E + \frac{3Q_p}{2\pi^3 \varepsilon_o (Rp)^2} \right] \quad \text{--- 2.23}$$

In this treatment by Martynov no account was taken of the curvature of the particle and it was assumed that when $g \sim 0.3\ R_p$ a uniform field existed in the particle - electrode interspace.

Subsequently, Chatterton et al. (33) have carried out field calculations for a model consisting of a positively charged sphere approaching a field - enhancing protrusion on an otherwise planar cathode such as shown overleaf.

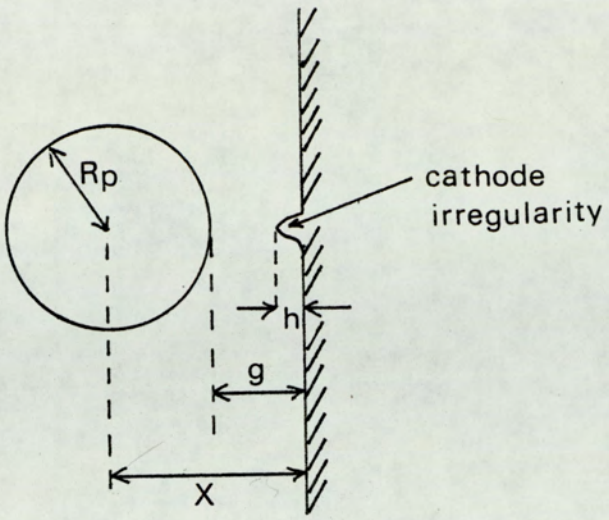

Figure 2.15 : Microsphere/cathode protrusion model

They considered the electric field intensity at the protrusion tip to be made of two components due to

i) the charge on the particle (73) = $\frac{Q_p}{4\pi\varepsilon_o R_p}$ and

ii) the distortion of the originally uniform field by the conducting sphere (72) = $Vf(\frac{x}{d})$

d being the distance between the parallel electrodes.

The combined field at the protrusion tip E_p (provided $g \leq X$) is now given by

$$E_p \simeq \beta\left[\frac{1}{9}\left(\frac{Q_p}{4\pi\varepsilon_o R_p} + V\left(\frac{x}{d}\right)\right]\right. \quad - - - \ 2.24$$

where β is the field enhancement factor of the small protrusion. This in turn gives a corresponding expression for E_g in the regime of Figure 2.15 as

$$E_g = \beta\left[\frac{1}{9}\left([R_p + 9]E + \frac{Q}{4\pi\varepsilon_o R_p}\right]\right. \quad - - - \ 2.25$$

The field enhancement factor will clearly vary with g for the geometry being considered and can be calculated using Miller's expression (74) where

$$\beta = \beta_{\infty}\left(1 - \frac{h}{g}\right) \qquad \text{---} \quad 2.26$$

and where β_{∞} is the enhancement factor for $g \gg h$. Expression 2.25 does not however take account of the effect due to induced charge distribution. More recently, Chakrabarti and Chatterton (34) have extended the above approximate analysis to carry out a more precise computation of the field between a charged conducting sphere and plane in an originally uniform field. They used the procedure of calculating a series of point charges and their images which allow the sphere and plane to be at zero potential, thus resulting in there being an induced charge say $-Q_1$ on the sphere given by

$$Q_1 = -8\pi\varepsilon_0 E_0 (g + R_p)^2 n\left(1 + \text{-------}\right) \quad \text{--} \quad 2.27$$

It then follows that the total potential V_T of the sphere relative to the plane is given by

$$V_T = \frac{Q_p + Q_1}{C} \qquad \text{---} \quad 2.28$$

where C is the capacitance of a charged conducting sphere near an earthed plate.

Beukema (35) using a similar approach to Chatterton et al. has derived an expression for the microscopic field in terms of the potential V_p of a charged sphere with respect to a plane, where V_p was originally derived by Morse and Feshbach (75) and is given

by

$$V_p = Q_p \left[4\pi\varepsilon_o R_p \sum_{n=0}^{\infty} \frac{2\left\{\left[(g+R_p)/R_p\right]^2 - 1\right\}^{\frac{1}{2}}}{\left[\left[(g+R_p)/R_p + \left\{\left[(g+R_p)/R_p\right]^2 - 1\right\}^{\frac{1}{2}}\right]^{2n+1} - 1\right]} \right] \quad \text{--- 2.29}$$

where g is the distance between the microsphere and the cathode, Q_p is the particle charge and R_p the particle radius. Beukema, however, did not consider the fact that the microparticle is in a non zero electric field and taking the critical field E_c for sufficient field emission to be $E_c \simeq 5 \times 10^9$ V m^{-1} approximated the above expression to

$$V_p \simeq \frac{Q_p}{4\pi\varepsilon_o R_p} + \frac{V}{d}(g + R_p) \quad \text{--- 2.30}$$

where V is the applied voltage. By appropriate substitution the corresponding expression for E_g is given by

$$E_g = \frac{1}{g}\left[\frac{Q_p}{4\pi\varepsilon_o R_p} + \frac{V}{d}(g + R_p)\right] \quad \text{--- 2.31}$$

which is similar to that obtained by Chatterton et al. (see equation 2.25). This is obtained from Lorrain and Carson's (73) calculations for the capacitance C of a charged conducting sphere near an earthed plane. Finally the field between the sphere and plane for small g / R_p is given by

$$E_g = \frac{Q_p + Q_1}{C_g} \quad \text{--- 2.32}$$

and the ratio of this field to the external applied field E is called the enhancement ratio. Comparing this result to the one obtained earlier by Chatterton it is found that the new calculation gives a lower value for the enhancement ratio as illustrated in Figure 2.16.

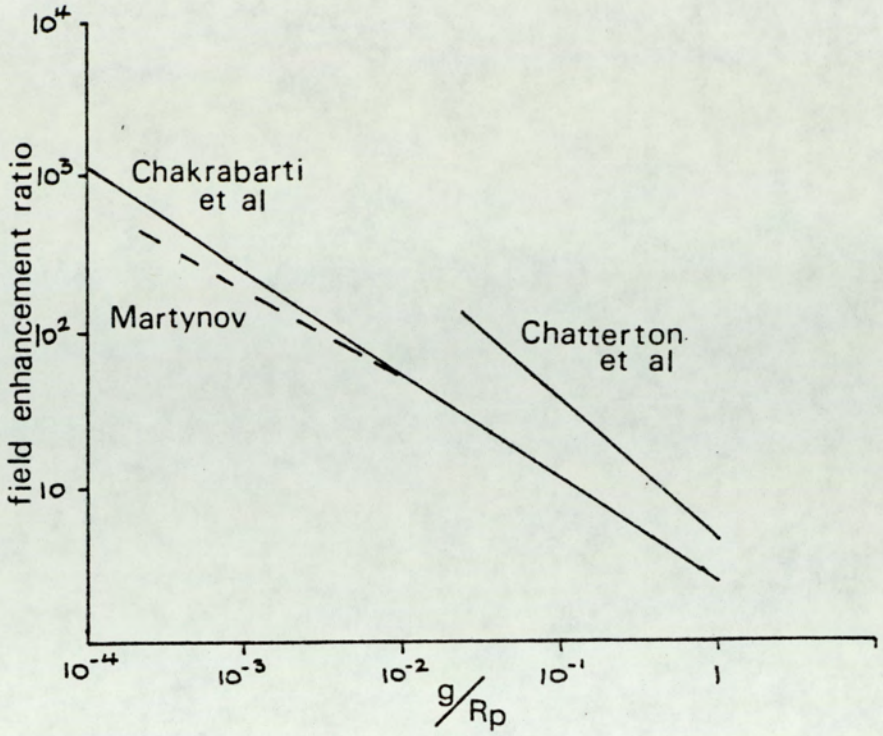

Figure 2.16 : Variation of field enhancement ratio with g/R_p

Variation of the cathode protrusion field with gap spacing g as illustrated in Figure 2.17 indicate that even with the modified field calculations large fields are still generated between the particle and the plane although they occur at smaller gap spacings.

Numerical evaluations of equations 2.23 and 2.25 indicate that the supposition of the trigger hypothesis, viz. that a discharge is struck between the particle and electrode, can only occur at close distances of approach when E_g exceeds a value of $\sim 3 \times 10^9$ Vm^{-1} allowing significant field emission to occur.

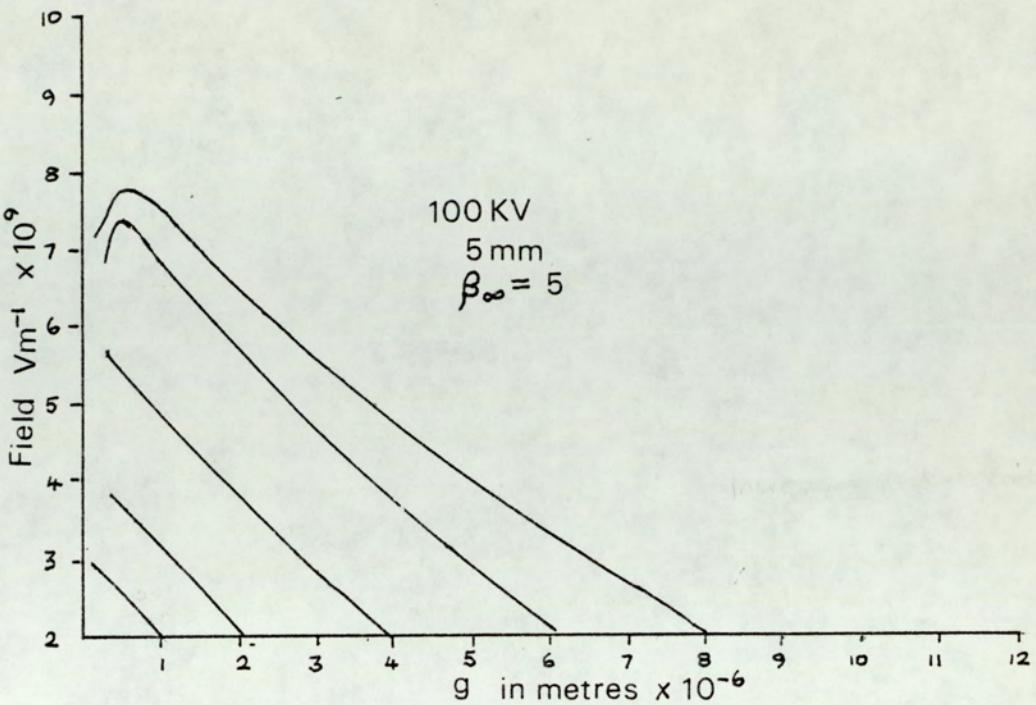

Figure 2.17 : Variation of field with gap

It also follows that the critical gap separation at which this occurs will increase with increasing particle radius through the dependence of Eg on both the ratio R_p / g and $Q_i (\propto R^2)$. In the case of the Martynov model (72) computations confirm that particles have to be $\geq 100\mu$ m in diameter for the phenomenon to occur: however, with the theoretical model of Chatterton et al. (33), it would appear that the mechanism can operate with $\sim 20\mu$ m diameter particles if the protrusion is assumed to have a β_∞- value of $\sim 5 - 10$. Chakrabarti and Chatterton's model (34) however indicates that the discharge process is unlikely to occur in practice unless particles greater than 50μm in radius exist in the system.

2.3.1 Microscopic field with the presence of surface oxides on sphere and target

In order to determine the effect of the dielectric surface films on the microscopic field Eg it is necessary to establish a theoretical model such as shown in Figure 2.18. In the absence of any in situ UHV surface cleaning procedures, both the particle and target will be covered by their respective ambient oxide films of thickness S_P and S_T which may be characterized electrically in terms of their respective dielectric constants, ε_P and ε_T

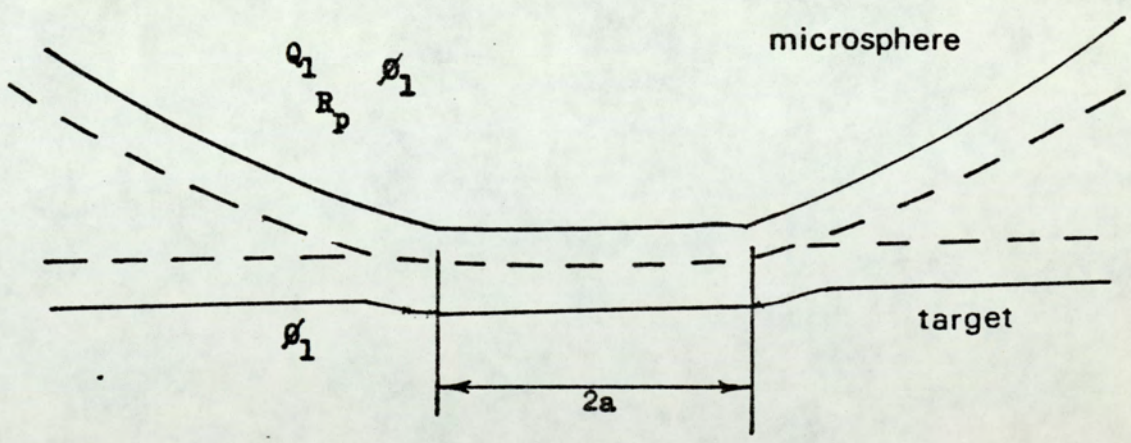

Figure 2.18 : Microsphere / plane separation

Once again the microscopic field Eg can be taken to be the resultant of components E_1 and E_2 (Section 2.3.0) with

$$E_1 = \frac{Q_i}{\bar{\varepsilon} C_o(g)\, g}$$

where Q_i is the equivalent induced charge on the sphere

$C_o(g)$ is the particle - plane capacitance in vacuum

and $\bar{\varepsilon}$ is the effective dielectric constant of the oxide film sandwich given by

$$\bar{\varepsilon} = \frac{\varepsilon_P \varepsilon_T}{\varepsilon_P + \varepsilon_T}$$

Using similar electrostatic solutions

$$E_2 = \frac{V_P}{g} = \frac{Q_P}{\bar{\varepsilon} C_o(g) g} \quad -- (73)$$

hence giving a total field Eg between the particle and target of

$$E_g = \frac{Q_P + 2{\cdot}6 \bar{\varepsilon} C_o(g) g (R_P/g)^{0{\cdot}8} E}{\bar{\varepsilon} C_o(g) g} \quad --- 2.33$$

The theoretical dependence of the localised gap field Eg on the gap separation g has been compared by Latham and Brah (43) and is illustrated below for $\bar{\varepsilon}$ = 1, 6 and 20

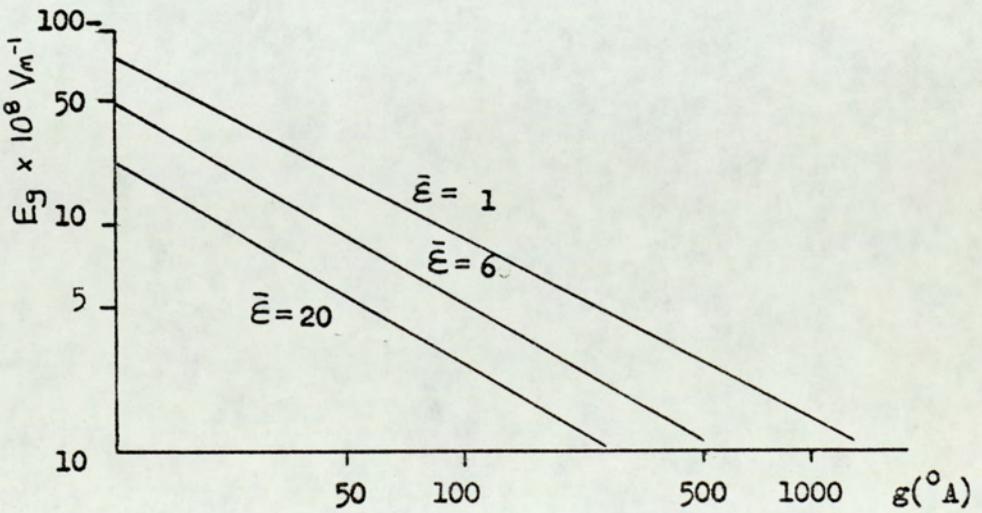

Figure 2.19 : Variation of field with gap

It can be seen from Figure 2.19 that $Eg < 10^9$ Vm^{-1} for all conditions thus excluding the possibility of inflight emission from the target and particle.

The total potential on the particle Vp is given by the equation $Vp = Eg.g$ and after substituting for Eg it becomes

$$Vp = \frac{Qp + 2.6\bar{\varepsilon}Co(g)g(R/g)^{0.8}E_o}{\bar{\varepsilon}Co(g)} \qquad --- 2.34$$

However since from Figure 2.19 it can be seen that E_1 is the dominant contributer for all values of g, Vp can be approximated to

$$Vp \sim \frac{Qp}{\bar{\varepsilon}Co(g)}$$

In addition it is evident from earlier considerations that although the process of electron tunnelling between dissimilar electrodes, separated by a thin oxide film can be independent of the film resistivity, it is greatly dependent on the tunnelling resistivity σ defined as

$$\sigma = \frac{Vp}{J}$$

where σ is in turn very sensitive to the film thickness S (68), its effective dielectric constant $\bar{\varepsilon}$ and the bias Vp existing across the film. By making appropriate estimates of the values of these parameters and adding the assumptions of

i) taking the effective contact area to be constant and equal to its mean value of $\pi a^2/2$

ii) approximating the linear dependence of the tunnelling resistivity to equal $\text{Log}\,\sigma \simeq \log\sigma_o - K\,Vp$ where σ_o is a constant depending on the thickness, band gap and dielectric properties of the film and

iii) assuming an exponential decay of Vp,

Latham and Brah (43) have derived an expression for the magnitude of charge transferred between the particle and target Q_r to be

$$Q_r = \left[\pi a^2 \, t \, c \exp (K \, V_{op})\right] \Big/ 2\sigma_o K \qquad \text{- - - 2.35}$$

This yields a value of Q_r of $\sim 10^{-16}$ C compared with a typical experimental value of $\sim 10^{-15}$C obtained in the present investigation.

To account for this discrepancy it should be noted that the above model does not take into account the non - planar microtopography of the target surface which would give rise to an additional local enhancement of E_g. In addition, the values for E and C_o as computed by Chakrabarti, Beukema and Lorraine and Carson are the values for an ideal sphere plane geometry whereas in the present investigation a more distorted system is probably in operation. Further, no account has been taken of the effect of differing work function values of the target and particle materials. These factors will be dealt with in more detail in section 5 where an improved model will be described.

CHAPTER 3

3.0 Experimental details

3.1 The vacuum system and experimental apparatus

Schematic representations of the detailed experimental regime used for studying the momentum and charge reversal associated with the bouncing impact of low velocity charged microparticles are shown in Figures 3.1 and 3.2.

The vacuum system is seen to consist of a bakeable stainless steel assembly pumped by a nitrogen trapped (N) Vacuum Generator four stage oil diffusion pump (Dp) (Edwards E106) which is backed via a sorption trap (ST) by a two stage gas ballasted rotary pump (Rp) with a pumping speed of 330 l/s. The diffusion pump is charged with a special poly-phenyl fluid, having a very low vapour pressure and thus making it ideal for clean UHV application. The function of the foreline trap between the diffusion and the rotary pump is to prevent any backstreaming hydrocarbon contamination from the rotary pump from reaching the diffusion pump. There is in addition a further safeguard against any accidental failure resulting in the system being contaminated with hydrocarbons from the diffusion pump in the form of an additional backing line incorporating a ballast reservoir tank fitted with a pressure protection switch (P). To aid a fast turn around of the system, a vitron sealed isolation valve (Va) can be operated for the purpose of separating the experimental chamber from the nitrogen trapped diffusion pump in order to maintain the pump under vacuum whilst allowing the direct use of the backing line,

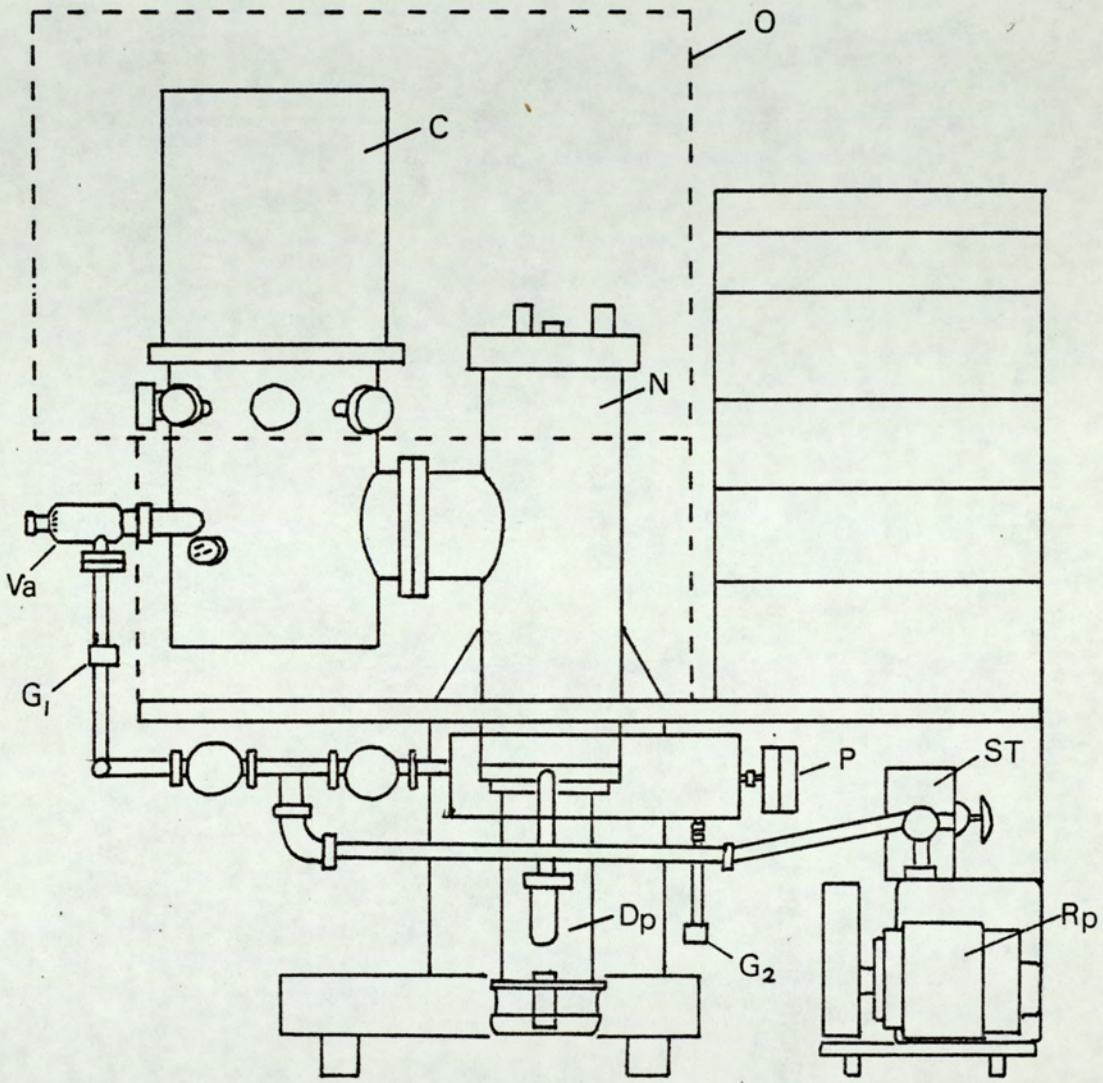

Figure 3·1: The vacuum system

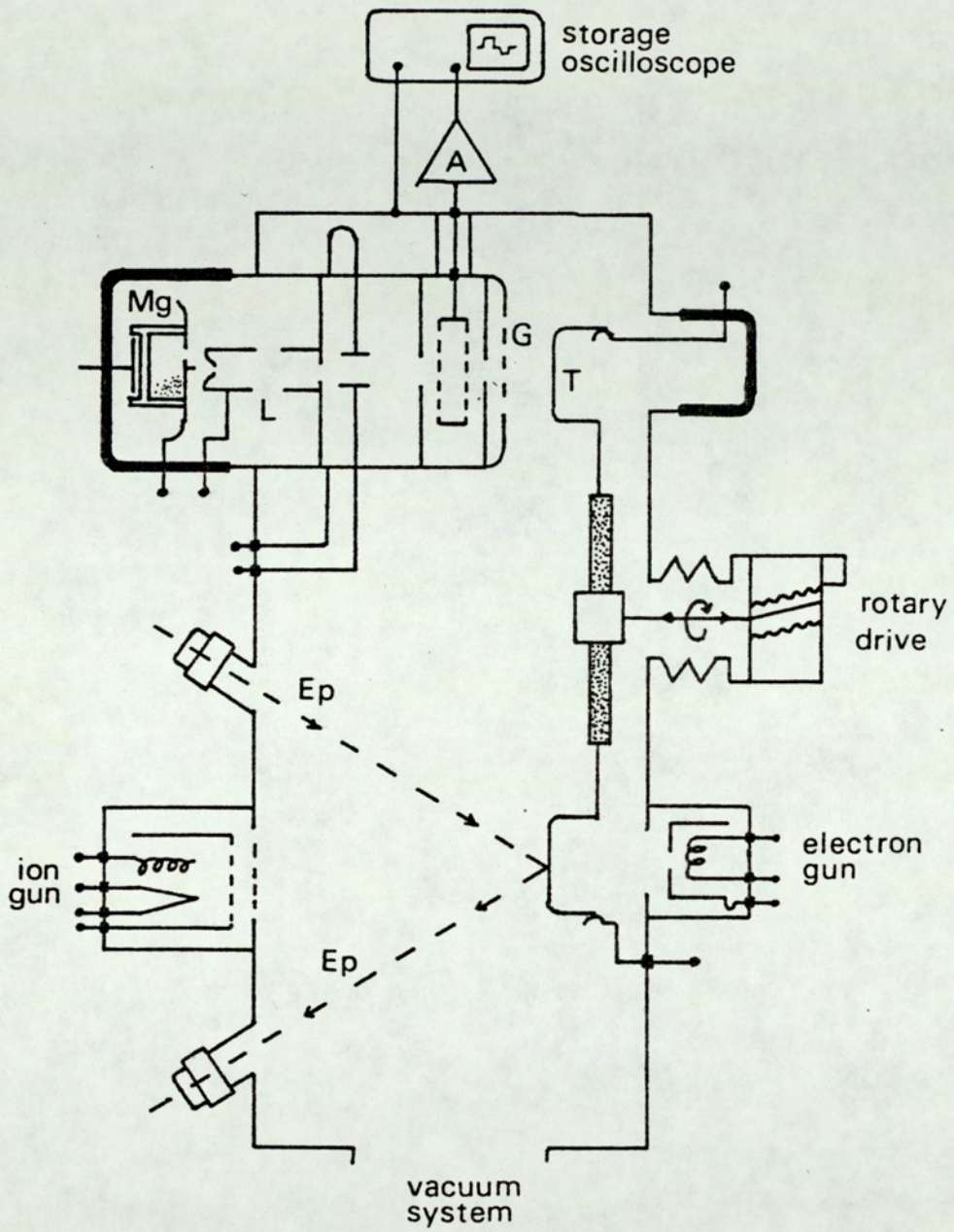

Figure 3.2 Schematic representation of the experimental regime

in roughing the chamber (C). The backing pressure is monitored by the use of two Pirani gauge heads (G_1), (G_2) whilst the pressure in the chamber is measured by an ionisation gauge. With the aid of ovens (O) for baking the stainless steel experimental system to approximately 200° C, an ultimate pressure of $\sim 1 \times 10^{-10}$ torr can be achieved.

of Fig 3·2

The experimental apparatus is based on a microparticle gun (Mg) that generates positively charged microspheres. This is followed by a symmetrical two cylinder electrostatic lens (L) which focuses and decelerates the microspheres for low velocity studies. The microparticles are characterised in terms of charge and velocity by a detecting system consisting of an electrostatically isolated drift tube that is connected to an external voltage sensitive amplifier (A). On leaving the drift tube the microparticles enter the experimental zone of a high field test gap which is established between a grounded stainless steel grid (G) and the target electrode (T). Prior to experiments, targets may also be rotated to another zone, for in situ 'servicing' by Argon ion etching and electron bombardment. In this zone an ellipsometer (Ep) is also incorporated to monitor the specimen surfaces and completes the experimental regime.

A detailed description of the above mentioned facilities is provided in the following section.

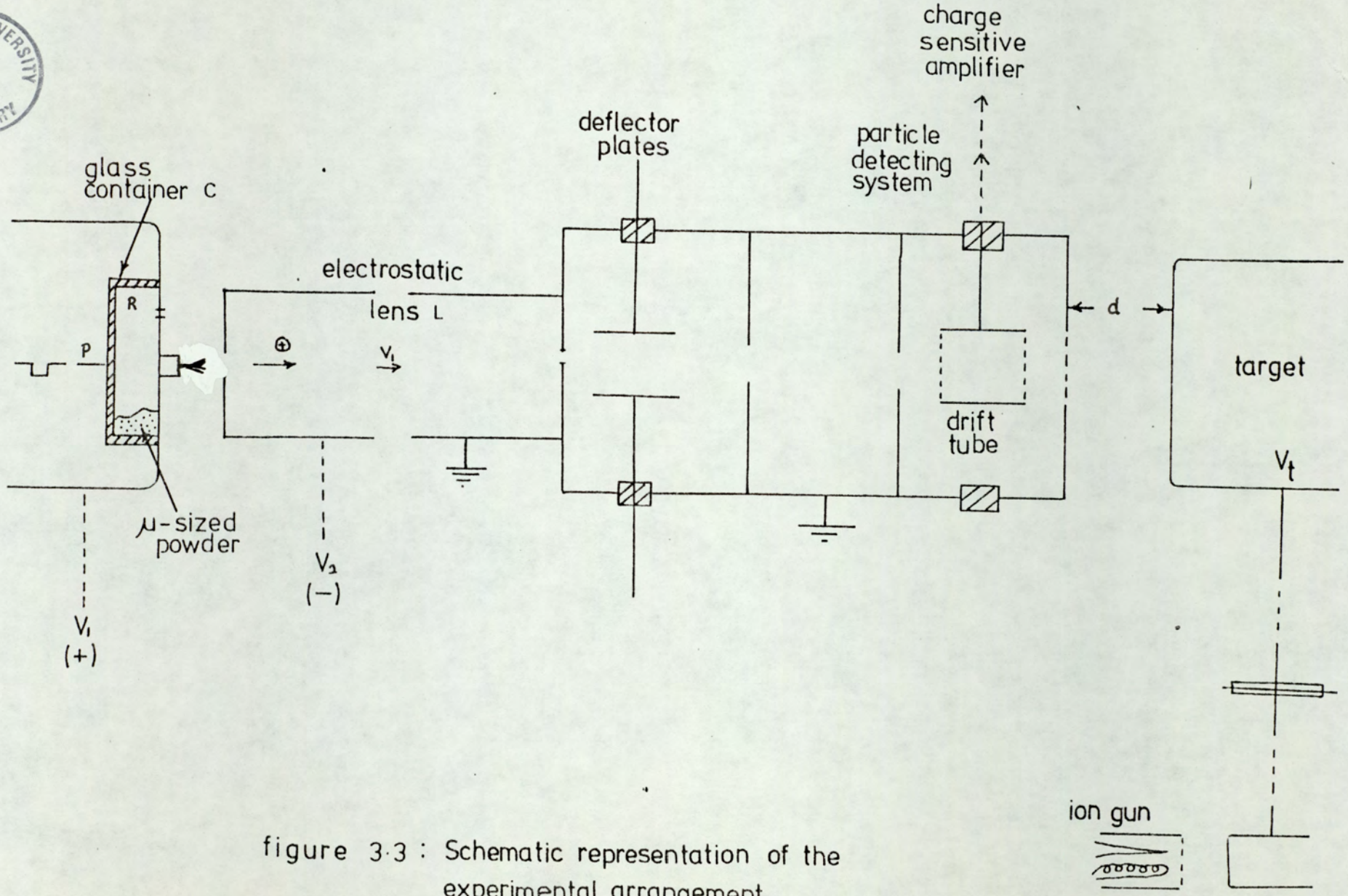

figure 3·3 : Schematic representation of the experimental arrangement

3.1.1 The microparticle gun

The device used for this investigation is a dust source type of gun based on the original design of Shelton et al. (76) and subsequently used by Friichtenicht and Slattery, 1965 (22, 37). It was however further developed for UHV applications and a full description of its construction and operational characteristics can be found elsewhere (43, 76). Accordingly only outline details of these aspects will be given in the present discussion.

Referring to Figures 3.3 and 3.4, the micron size powder charge is contained in a glass cup (C) which is located against the charging electrode assembly by a spring - loaded plunger. For the present investigation, this was charged with either carbonyl iron or gold microspheres having diameters ranging from .1 to 5μ m obtained commercially from GAF.

To help overcome an inherited operational problem of 'powder paralysis' (to be discussed more fully in section 3.1.2) a silver film was evaporated on the back face of the glass cup to improve the field distribution in the reservoir. It should also be noted that the inside surface of the charging electrode has to be carefully polished to avoid a second operational problem of powder adhering to this surface and 'clogging up' the gun.

To 'fire' a loaded gun, a negative - going square pulse (Figure 3.3) of amplitude $\sim$ 10 K V and duration $\sim$ 20 ms, derived from the high voltage switch circuit shown in Appendix 1, is applied to the

back electrode of the reservoir via the plunger electrode (P). This negative pulse establishes a temporary electric field across the powder reservoir which causes the individual particles to become charged by direct contact with the metal face of the charging assembly and hence are explosively agitated due to the mutual repulsive forces between them. In the course of this process they can undergo complicated bouncing sequences between the opposite faces of the reservoir (R) and are able to exchange charge involving the same type of basic charge exchange process that has been studied in this thesis. As a result of this explosive agitation some particles are able to escape via a small hole (H) and thus enter a high field region containing a radiused aperture (Ar).

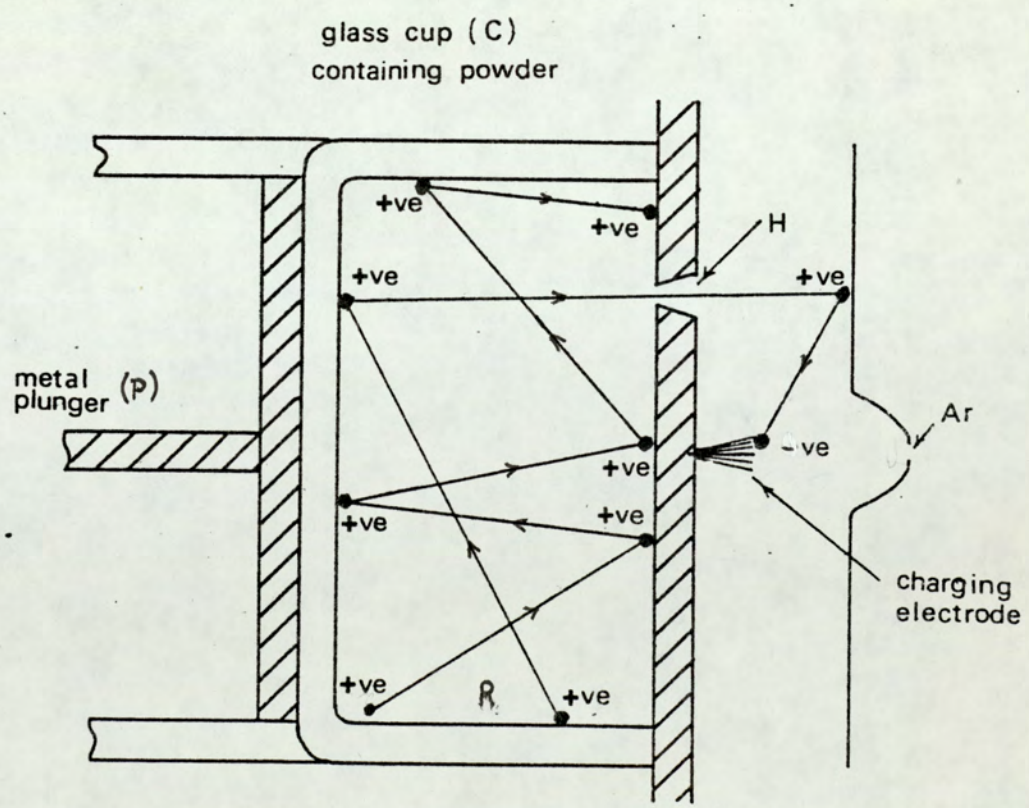

Figure 3.4 : Microparticle bouncing sequence

On entering the high field region the particles again undergo 'reflection' until they eventually impinge on the carbon fibres where as a result of contact electrification they acquire a charge of the same polarity as the carbon fibres. Due to the action of the approximately radial accelerating electric field existing between the tip and the radiused aperture the charged microparticles are then accelerated towards the aperture with a few particles escaping through it towards the electrostatic lens (L).

The use of a bunch of ~ 15 micron diameter carbon fibres instead of a conventional single mechanically pointed tungsten electrode results in a higher charging field due to an increased geometrical field enhancement at the tip of an individual fibre. This therefore enables lower gun voltages to be used in addition to having the important advantage for the present study of giving lower particle velocities (78). Due to the absence of electrically insulating oxide layers on carbon fibres normally present on conventional metallic tips the charging mechanism is further enhanced and thus constitutes an additional advantage of using carbon fibres. Furthermore, the charging probability is increased because of the multiplicity of charging 'points' which makes the gun a generally more efficient device. Depending on the polarity of V_2 relative to V_1 (Figure 3.3), where $(V_2 - V_1)$ is defined as the 'gun voltage' and corresponds to the voltage through which the particles are accelerated before passing through the radiused aperture (Ar), in principle, it is possible to generate positive or negative particles. However, due to

the damaging effect of excessive electron field emission from the carbon fibres when operated with $V_1 < V_2$ the negative function is intrinsically unstable. For this reason the gun has only been used to generate positively charged particles in the present investigation.

3.1.2 Problems associated with the particle gun

A major operational problem inherited with this type of gun, particularly when used with carbonyl iron spheres as the micro-particle source, was the tendency for the powder to become 'paralysed'. After the application of a number of high voltage pulses the powder ceased to be agitated so that the gun became inoperable. The onset of this condition generally proved to be irreversible so that the only solution was to dismantle, clean and reload the gun. However this meant that a particular experimental investigation could suffer from frequent interruptions so that it was very difficult to achieve continuity and reproducibility between measurements. In fact, this limitation of the gun facility was considered to be unacceptable, so that it was decided to investigate the possibility of implementing a more permanent remedy.

The initial approach to explain the 'paralysis' effect involved the assumption that it resulted from some sort of field induced effect within the glass container. This interpretation was however subsequently discarded as being unlikely. An alternative explanation assumed that during the course of the bouncing excursions of the charged microparticles (see Figure 3.4)

positive charge was dumped on the inner surface of the glass reservoir so that an internal fieldwas set up within the reservoir that would tend to oppose the applied negative pulsed field and thereby inhibit the agitation of the powder. Here again however, a number of routine tests indicated that this explanation was probably incorrect.

The third and most profitable approach to the 'paralysis' problem assumed it to be associated with the non-uniformity of the pulsed field within the reservoir, which stemmed partly from the severe 'edge effects' arising from the fact that the area of the plunger was smaller than the back face of the reservoir (see Figure 3.4), and partly from the inevitably uneven contact between the metal plunger and glass reservoir. To eliminate these features of the original design a conducting film of silver was evaporated onto the back face of the glass cup as shown in Figure 3.5, and as a result of this modification, no further 'paralysis' problems were encountered.

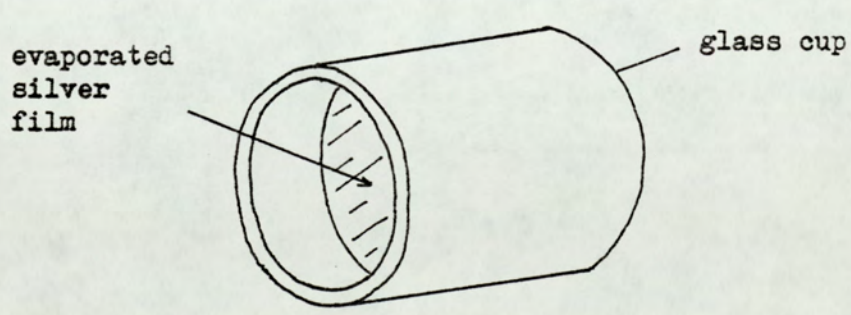

Figure 3.5 : Glass reservoir

3.1.3 Electrostatic decelerating and focusing lens

This has two main functions:

i) to reduce the particle velocities from $\sim$ 200 m/s to 300 m/s on leaving the gun to between 20 m/s and 100 m/s on leaving the lens.

ii) to increase the flux of microparticles reaching the experimental zone by using the focusing action of the lens.

Referring to Figure 3.6 the lens is in the form of a symmetric two - cylinder (C_1 and C_2) electrostatic lens supported and electrically insulated by vitroesil rods.

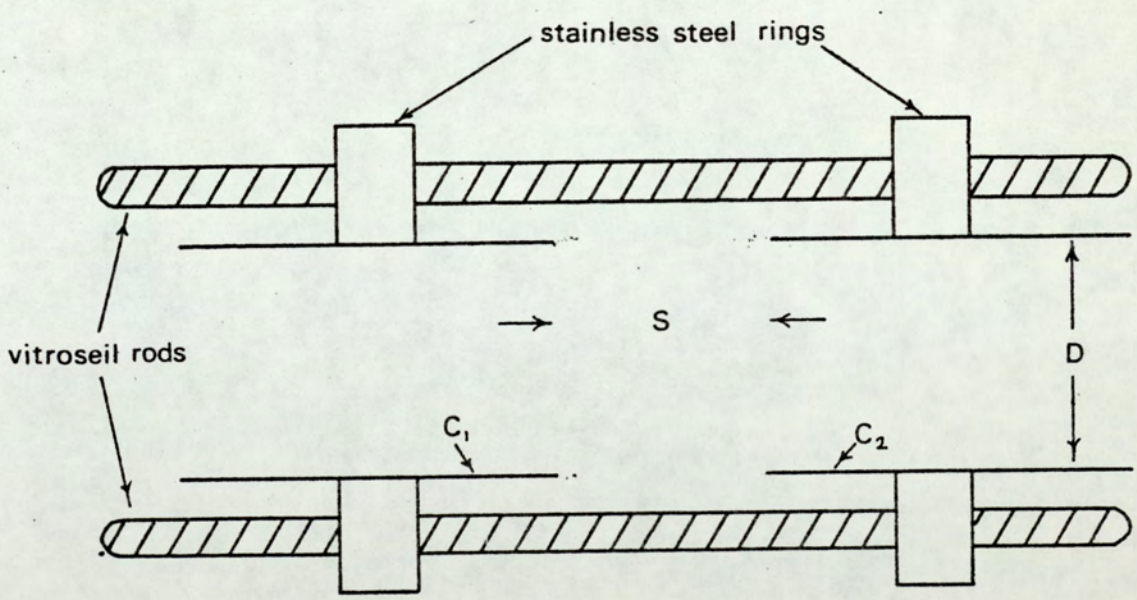

Figure 3.6 : The electrostatic lens

The lens separation S of 16 mm is equal to the internal diameter D of the two concentric cylinders i.e. S/D = 1. This geometry

is based on theoretical computations of Read et al. (79) and was chosen to give a weak lens configuration. Although the focal length of the electrostatic lens is independent of the charge to mass ratio (q/m) of the particles, it will however depend on the approach velocity of the microparticles and hence depends on the ratio of the voltages of the two elements: the latter being referred to as the source potential which in this case is the tip voltage. It follows therefore that since there is a considerable spread in the particle velocities emerging from the gun, then in the present investigation the lens will exhibit chromatic aberration with the lowest velocity particles being focused nearest to the lens.

3.1.4 Particle detecting system

This is basically a capacitance time - of - flight device in which, as shown schematically in Figure 3.7, an electrostatically shielded, low capacitance stainless steel drift tube of length $L = 3$ cm, is directly connected via a glass - to - metal lead through, to an external voltage sensitive pre-amplifier and finally a storage oscilloscope.

The drift tube is mounted concentrically with the particle axis in a ceramtec insulating ring. When a charged microparticle passes through the drift tube on its way to the target, it induces an equal charge on the tube and is thus detected on a storage oscilloscope as a trapezoidal signal shown in Figure 3.8.

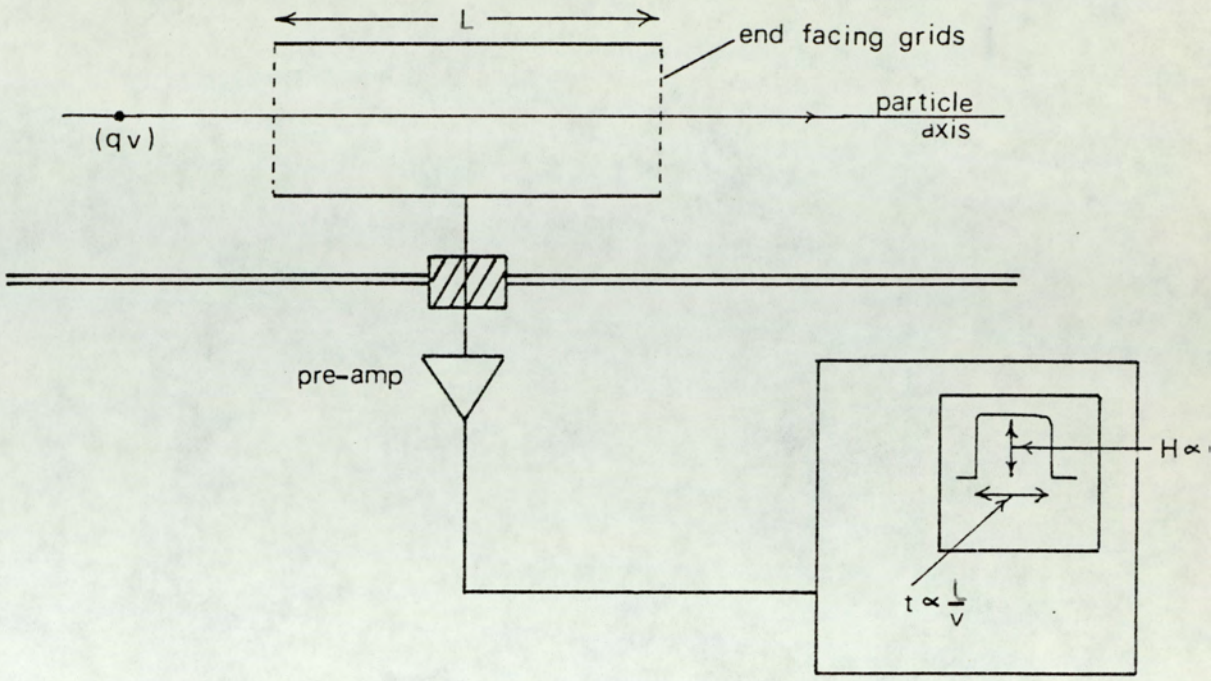

Figure 3.7 : Particle detecting system

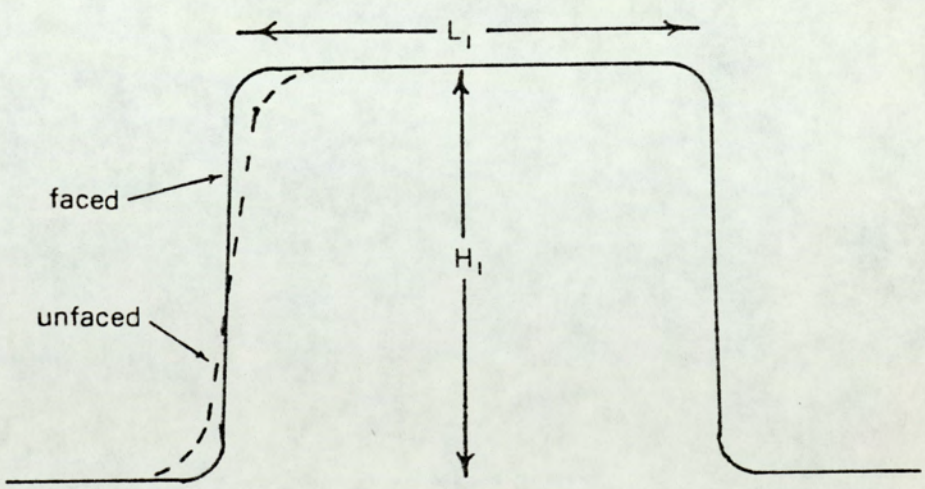

Figure 3.8 : Trapezoidal signal

To sharpen the leading and trailing edges of this signal and hence improve the time resolution, the tubes are faced with stainless steel grids having 90% transparency to the particles. By measuring t, the transit time of the particle in the drift tube the particle velocity v is thus given by 1/t, whilst the particle charge q is obtained directly from H and the sensitivity of the pre - amp. In addition, the mass m of the particle can be found using the energy conserving relation

$$q V_G = \frac{1}{2} m v^2 \qquad \text{- - - 3.1}$$

where V_G is the gun voltage or effective potential through which the particle is accelerated (see Section 3.1.1).

The preamplifier, which is basically a charge to voltage converting device, is capable of detecting a charge of 10^{-15} coloumbs. It was designed around a commercially available FET input integrated circuit as shown in Figure 3.9 which, as described below, has the advantage of maximising the sensitivity and giving a high signal - to - noise ratio. It also satisfies the basic requirements for the efficient detection of low charges. These can be summarised as follows:

1. A minimum input capacitance to maximise the input voltage signal per unit charge.
2. A high input resistance of $\sim 10^{12}$ ohm to avoid excessive pulse differentiation i.e. the input time constant is large compared with the transit time t of the microparticle through the drift tube.
3. A wide band frequency response to ensure smooth (undistorted) rise and fall of the pulses.

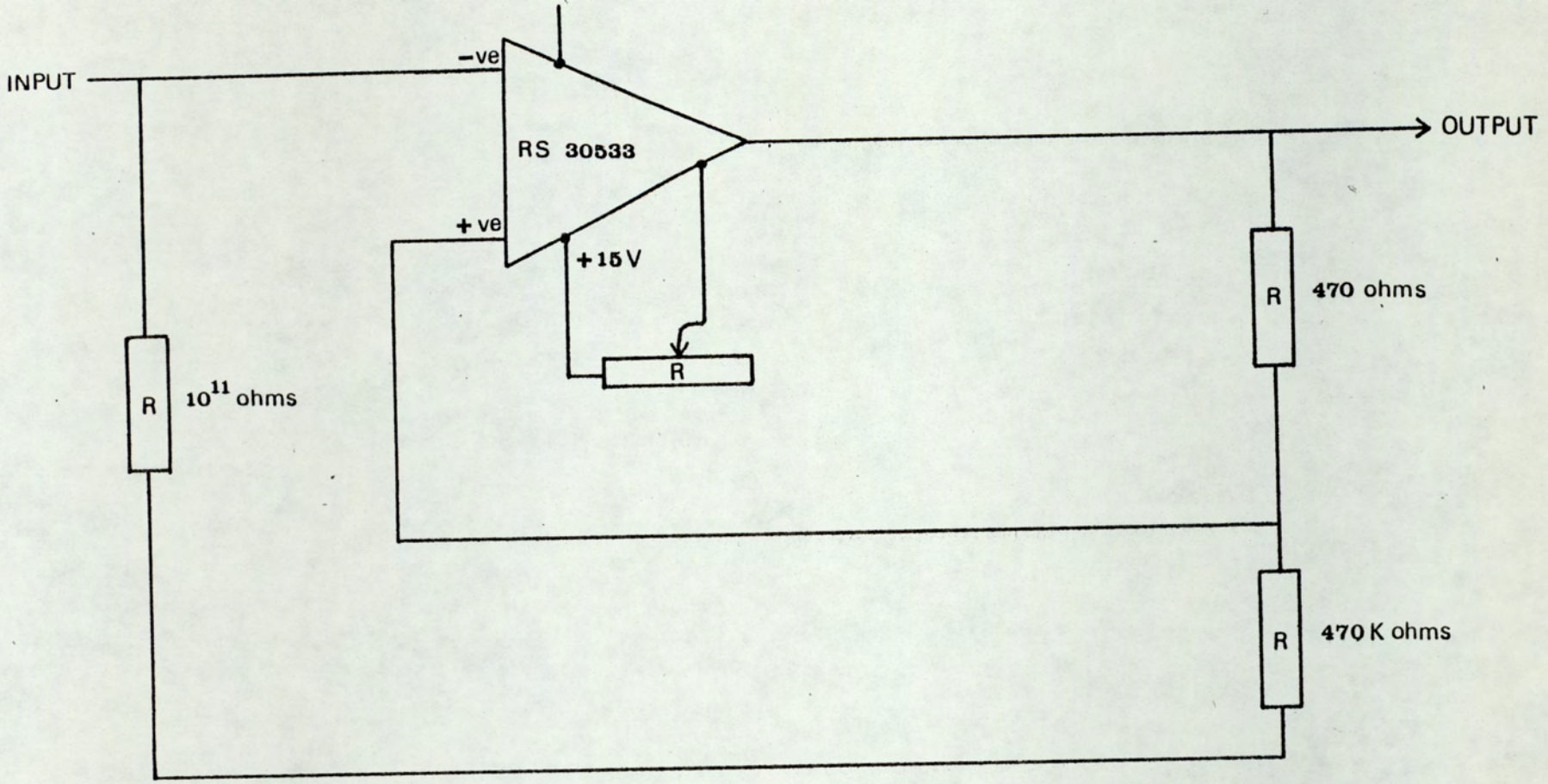

Figure 3·9: Voltage sensitive amplifier

The above requirements were met by using a Radio Spares FET 30533 integrated operational amplifier in the non inverting configuration shown below (Figure 3.9). To minimise electromagnetic interference the entire circuit was carefully shielded by mounting it in an earthed can.

3.1.5 The 'test' high voltage gap assembly

Since the purpose of this investigation was to study the bouncing impact behaviour of charged microparticles on broad area high voltage electrodes, a 'test' gap that closely simulated the conditions existing in a real operational gap was necessary, whilst also providing the facility for injecting microparticles.

Referring to Figure 3.2, this was realised by a stainless steel grid (G) that was almost transparent to the incident particles, and a planar target electrode (T). For the present study employing positive microparticles, a negative voltage V_T is applied to the target and produces a field E between the target and the grid which is parallel to the direction of the incident microparticle. The fine grid with a 0.5 mm mesh and a 0.043 mm grid wire diameter gives a transparency of 90% for the incident microparticles. It also ensures that the periodicity of the local grid field will be smoothed out sufficiently (80) to assume a uniform and well defined macroscopic field at the target surface.

The button shaped targets (Figures 3.18 and 3.19) were mounted on ceramtec insulating supports which formed the arms of a four

spoke externally rotatable turret assembly (Figure 3.10). This arrangement had the advantage of enabling several specimens of differing material and surface preparation to be studied at each pump down and allowing a particular target to be rotated from its 'test' position in the upper part of the chamber on the axis of the microparticle flux to the 'service' position in the lower part of the chamber. In this position there are an argon ion and an electron gun for in situ surface treatment of the electrodes (Figure 3.2) together with an ellipsometric facility for monitoring the surface (see Section 3.4).

The orientation and axial position of the target are controlled by means of an externally marked X, Y Z mechanism via a stainless steel bellows and a rotary drive (Figure 3.2). The range of the gap separation studied is between 2 mm and 5 mm.

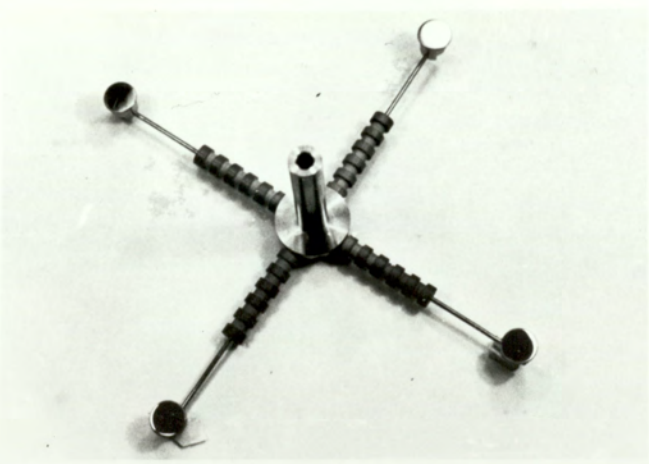

Figure 3.10 : Turret target assembly

3.2.1 Argon ion etching facility - Basic requirements

An essential aspect of the present study involved the removal of the surface contaminations, such as oxide films and adsorbed gas from the target surfaces in order to compare the impact behaviour of microparticles with oxidised and metallically clean targets. This was achieved by the use of a low energy argon ion gun which had the capability of

i) producing and accelerating an adequate flux of ions to the required energy for the present surface cleaning application,

ii) remaining in a stable operational state over the long periods of operation necessary for ion etching,

iii) using materials of high insulating ability so that it is quick and easy to outgas and clean in case of contamination.

These requirements were realised by a spherical source ion gun designed by Fitch et al. (81). This also provided the additional advantage of being small, thus making it particularly adaptable for use as an auxillary facility in a sophisticated UHV experimental regime for surface studies. Futhermore, since high etching rates on small surfaces are required for this study, the use of the spherical source avoided the severe surface damage to the electrode which normally results by the previously employed cylindrical source (77).

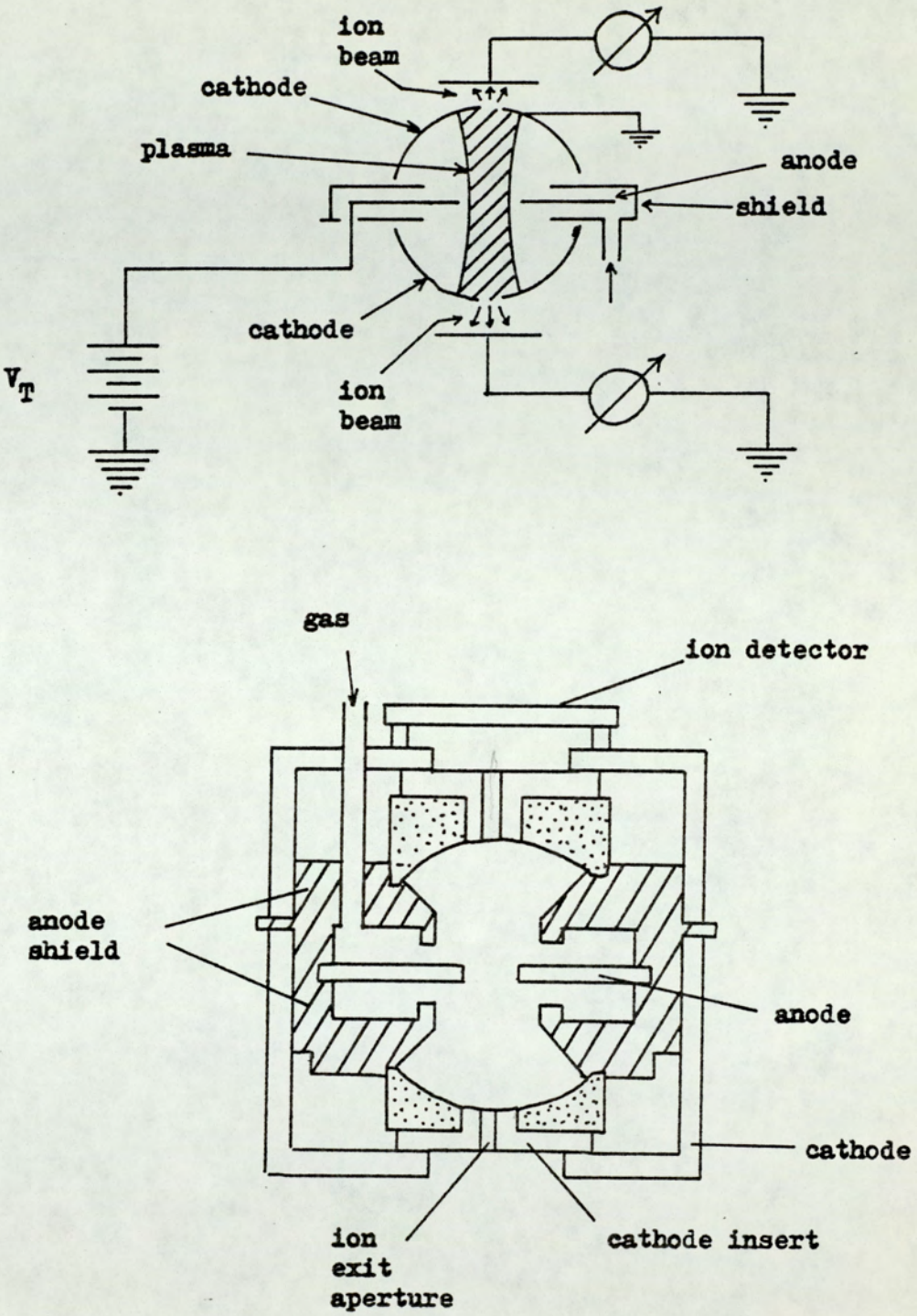

Figure 3.11 : Spherical Ion source

3.2.2 Details of the saddle field spherical ion source

This was based on a recent design of Franks (82) that produces a more intense and less divergent beam than the more commonly used cylindrical source. Referring to Figure 3.11 the spherical configuration is produced by using two stainless steel cylinders placed either side of the 5 mm diameter anode of the same material. The ends of the two cylinders are closed with aluminium cathode discs and the ion beam is allowed to escape through holes of 1.55 mm diameter in each disc. All the insulating components are made of ceramtec material and the entire assembly, including the gas inlet and H.T. leads to the anode are enclosed in an outer cylindrical Duralumin body. A nickel collector opposite one of the apertures is used to monitor the ion beam.

3.2.3 Modes of operation

It has been found (83) that the spherical source operates most efficiently at a pressure of between 10^{-4} and 10^{-5} torr together with an applied voltage of between 4 and 6 KV, resulting in an ion beam current varying from 40μA and 60μA. In the present investigation the source was operated at a voltage of 4.6 KV at 10^{-5} torr pressure resulting in a collected ion beam current of $\sim 30\mu$A. A voltage stabilised power supply incorporating meters to monitor the anode voltage and current was employed in this study. The collected ion beam current was measured using a micro-ammeter connected to the target under test via an electrical feed-through as illustrated in Figure 3.12.

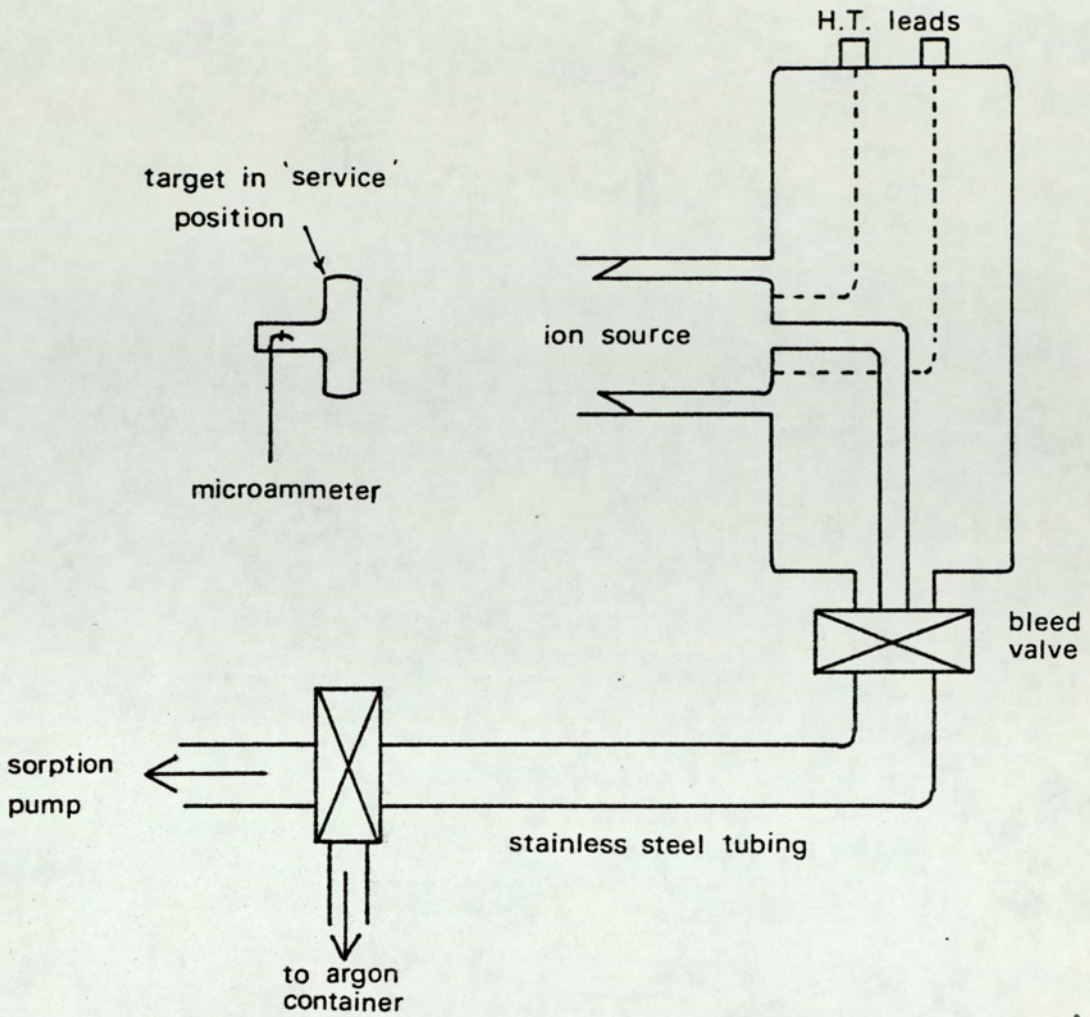

Experimental arrangement for the ion source

Figure 3.12

3.2.4 Experimental procedure

The ion source was cleaned thoroughly prior to its initial assembly in the purpose designed module shown in Figure 3.12. The latter also included the gas inlet system and the H.T. leadthrough thus enabling the ion source to be adjusted and assembled outside the main experimental chamber. To ensure that only pure argon and not a mixture of argon and air was allowed into the source, a subsidiary vacuum pump and specially fitted bakeable stainless steel pipes between the argon gas container and the ion source were employed (Figure 3.12).

After evacuation of the argon inlet pipes, argon gas was allowed into the system as far as the 'bleed' valve and the assembly again evacuated. On completion of this second evacuation argon gas was 'bled' into the experimental system until the pressure increased from $\sim 10^{-9}$ torr to $\sim 10^{-5}$ torr. The pressure was then allowed to remain at 10^{-5} torr and the voltage slowly increased to 4.6 KV when a stable low ion - beam current $\sim 30 \mu A$ was obtained. The surface was etched until, from ellipsometric monitoring, as described in Section 3.4, it was clear that the oxide film and surface contaminants had been removed.

3.3.1 Electron gun

Electron bombardment was used as an alternative facility for removing surface oxide films by heating the target electrode to a temperature of $\geq 700\ ^{o}$ C at a pressure of $\lesssim 10^{-7}$ torr. Under these conditions it can be assumed that the surface impurities decompose at temperatures below the melting point of the base material.

Referring to Figure 3.13 the electron gun used was of a triode design and consisted of a heated spiral tungsten filament (F), a concentric grid (G) and an anode cylinder (C). An electromagnetic focusing lens (L) with a maximum ampere turn rating of 300 was mounted externally on an orientation - adjustable Cardini ring system to enable focusing of the electron beam to a 1 cm^2 spot and directed to the centre of the target.

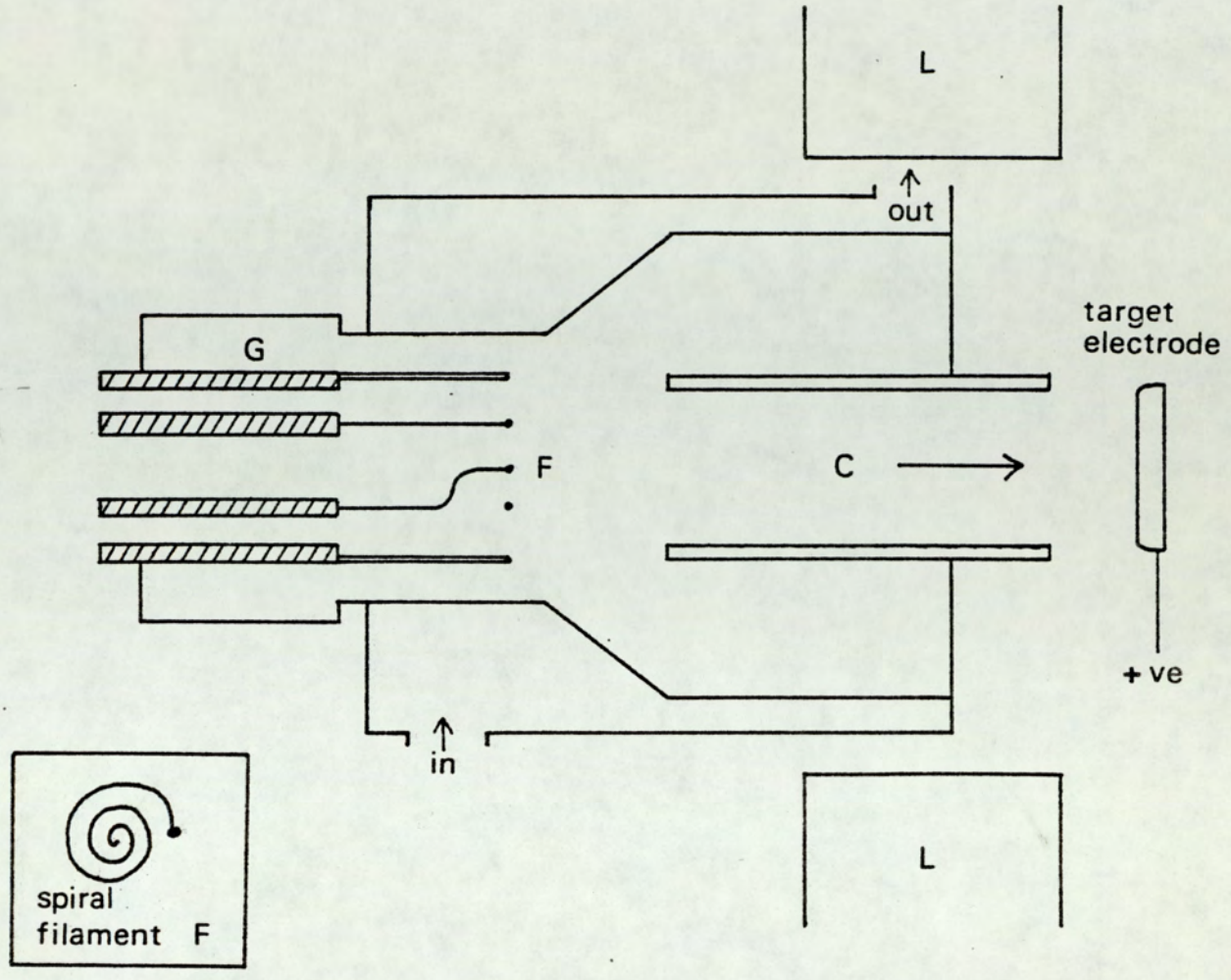

Figure 3.13 : Electron gun

An additional high current EHT, power supply was employed to provide a positive target potential variable between 0 and 3 KV. This had the effect of increasing the electron impact energy from -750 V at the gun onto the target and eliminating backscatter i.e. maximising the electron beam onto the target electrode. The grid was biased negatively with respect to the cathode and a maximum collected current of $\sim$ 8mA was obtained after focusing. Again the electrode was heated until ellipsometric monitoring, described in the following section, showed that the surface oxide film and contaminations had been reduced to a minimum.

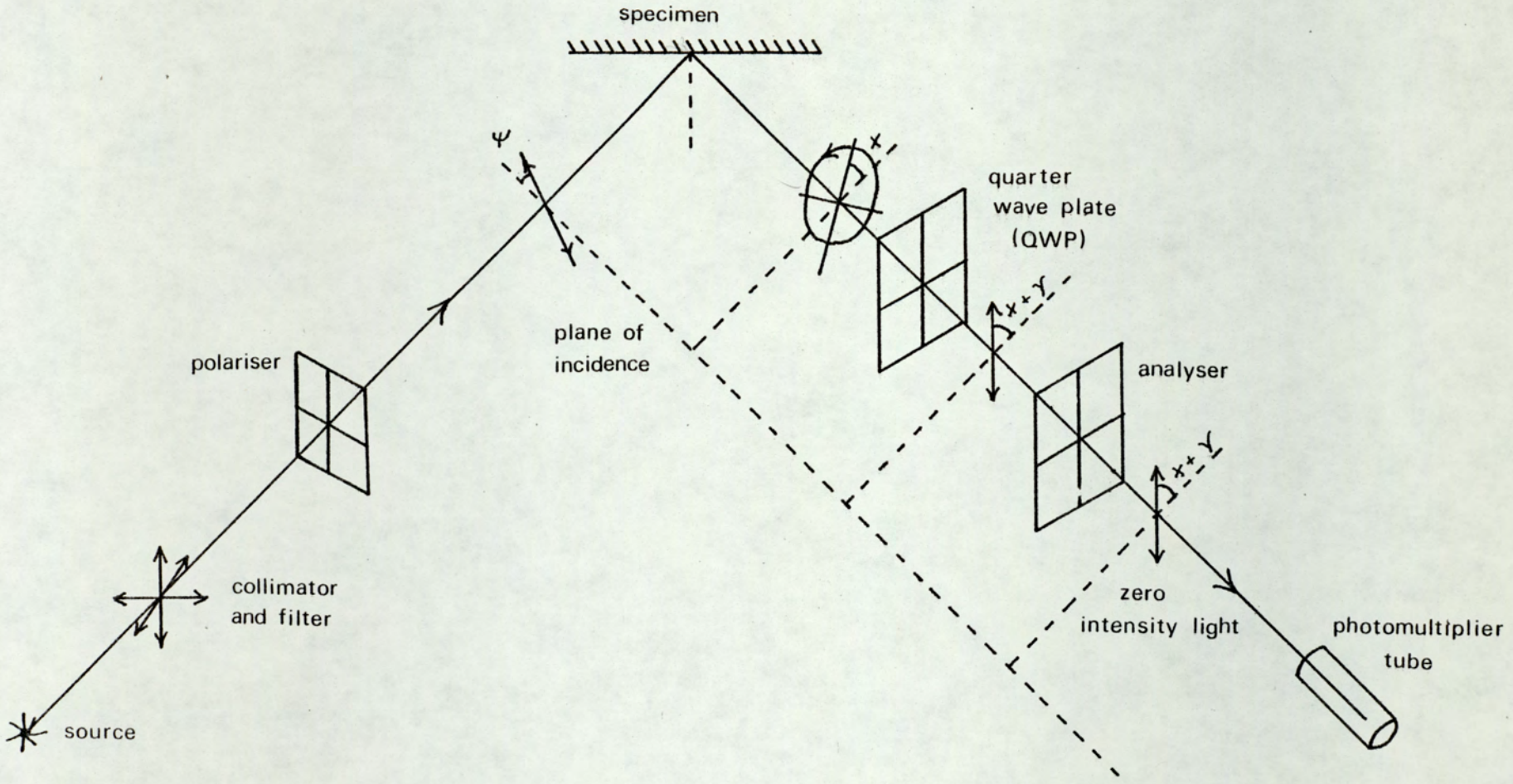

Figure 3·14 A schematic representation of the ellipsometer

3.4.1 The ellipsometer surface analysis facility

Ellipsometry is a technique which is suitable for the in situ non destructive examination of surfaces: in particular it is especially suitable for measuring the thickness of thin oxide films from a few angströms down to less than half a monolayer present on metal substrates. It depends on the principle that if initially plane polarised light is incident on a test surface, the reflected beam will generally be elliptically polarised. By measuring this ellipticity and knowing the optical constants of the film and substrate it is possible to determine the optical properties and thickness of thin films on reflective substrates.

3.4.2 Ellipsometric arrangement

Referring to Figure 3.14, the ellipsometer facility whose components are outside the vacuum system is essentially a polarising spectrometer consisting of a light source (12 V, 100 W tungsten filament projector lamp) followed by optical polarising and analysing elements and a light detector. The polariser and analyser are Nicol prisms (Glan - Thompson design) of variable azimuths and are mounted on commercially available vernier scales where readings of the change in polariser angle Ψ and analyser angle Δ can be made to an accuracy of $\pm$ 0.01°. The light detector is a photomultiplier tube supplied by E.M.I. and is used in conjunction with a 5 KV stabilised power supply.

Optically flat kodial glass view ports transparent up to 2 μm wavelength are used for transmitting the light from the polariser

to the specimen and the reflected beam back to the analyser. The quarter wave plate (QWP) consists of a bifringent sheet of mica of an exact thickness mounted on a vernier scale.

3.4.3 Principles of the ellipsometer

Classical electromagnetic wave theory provides the basic equations relating to the ellipsometer. Consider first a film free surface with plane polarised light incident on it, where the plane of polarisation is neither parallel nor perpendicular to the plane of incidence. If the two media involved are assumed to be isotropic and homogeneous then the problem of reflection and refraction of light at the plane boundary is usually solved by applying the boundary conditions to sinusoidal electromagnetic wave equations so that the case of plane waves with electric vectors vibrating parallel (p) to the plane of incidence is treated separately from those with vectors vibrating normal (s) to the plane of incidence. Due to the linearity of the wave equation, superposition is allowed so that other cases can then be conveniently analysed by decomposition into p and s components, followed by superposition of the resulting solutions. Thus in practice the angle of incidence is usually taken as 45° so that the amplitude and ratio of p and s components is unity. For the situation illustrated in Figure 3.15 of two isotropic and homogeneous media reflection will produce a phase difference between the p and s components of the incident and change the amplitude ratio.

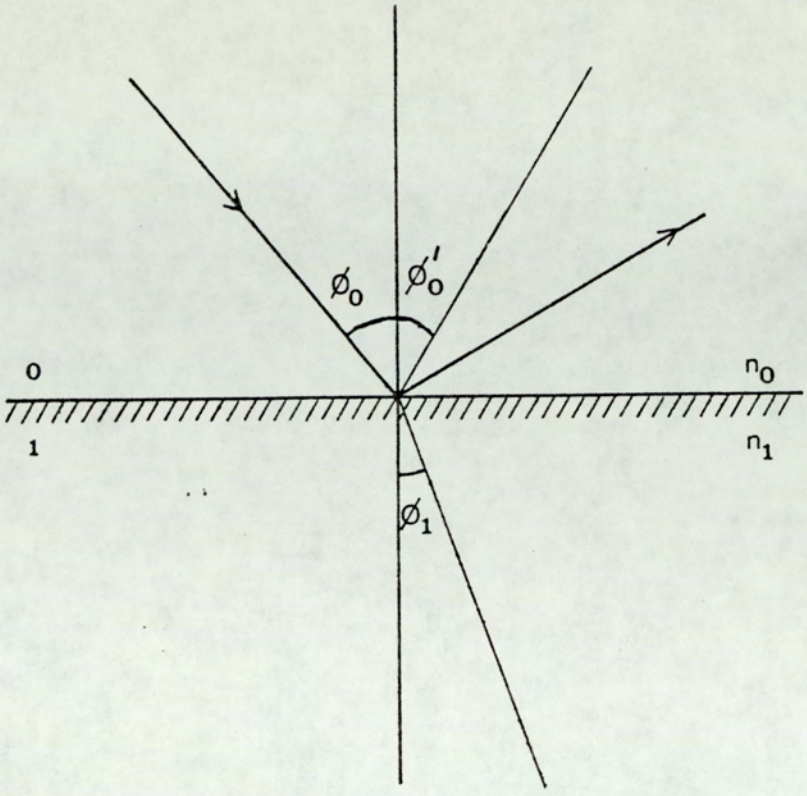

Figure 3.15 : Reflection from Homogeneous media

These changes can be expressed in terms of the following Fresnel coefficients for light travelling from medium 0 to 1 having angles of incidence and refraction ϕ_o and ϕ_1 respectively.

$$r_{o1}\ (p) = \frac{n_o \cos \phi_1 - n_1 \cos \phi_o}{n_o \cos \phi_1 + n_1 \cos \phi_o} \qquad \text{- - - 3.2}$$

$$r_{o1}\ (s) = \frac{n_o \cos \phi_o - n_1 \cos \phi_1}{n_o \cos \phi_o + n_1 \cos \phi_o} \qquad \text{- - - 3.3}$$

where n_o and n_1 are the respective refractive indices of the media.

Similar expressions are obtained for the transmission coefficients. The relationship of these reflection coefficients to the instrument

reading Δ and ψ the respective angles determined by the analyser and polariser, is given by the basic ellipsometry equation

$$\frac{rp}{rs} = \tan\psi\, e^{i\Delta} \qquad \text{- - - 3.4}$$

For a non absorbing surface film of refractive index n_1 on a substrate of refractive index n_2 the Fresnel coefficients are written as

$$rp = \frac{r_{01}(p) + r_{12}(p) \exp D}{1 + r_{01}(p)\, r_{12}(p) \exp D} \qquad \text{- - - 3.5}$$

with a similar expression for rs, where

$$D = \frac{4\pi n_1 \cos\phi_1 d}{\lambda} \qquad \text{- - - 3.6}$$

d is the film thickness and λ is the wavelength of light. For absorbing media such as metals or semiconductors a complex refractive index $N = n - ik$ replaces the real n - value used previously so that the Fresnel coefficients also become complex, as does the value of D which is given by

$$D = \frac{4\pi i N_1 \cos\phi_1 d}{\lambda} \qquad \text{- - - 3.7}$$

For opaque film free surfaces, n and k are related to ψ and Δ through equations 3.2, 3.3 and 3.4 and are given in the following form suitable for computation by Ditchburn (83).

$$n^2 - k^2 = \frac{\sin^2\phi_o \tan^2\phi_o (\cos^2 2\psi - \sin^2 2\psi \sin^2\Delta) + \sin^2\phi_o}{(1 + \sin 2\psi \cos\Delta)^2} \qquad \text{- - - 3.8}$$

and

$$2nk = \frac{\sin^2\phi_o \tan^2\phi_o \sin 4\psi \sin\Delta}{(1 + \sin 2\psi \cos\Delta)^2} \qquad \text{- - - 3.9}$$

With the presence of a surface film the computed values of n and k relate to a composite surface and are normally referred to as pseudo - constants.

3.4.4 The compensator

The basis of the compensator method used in the present study is illustrated in Figure 3.14 where it can be seen that the plane polarised light, transmitted by the polariser P is incident on the specimen with its plane of polarisation inclined at an angle Ψ to the plane of incidence.

On reflection the light will be elliptically polarised due to the electric vector moving in an ellipse with the azimuth of the major axis X, and the ratio of minor to major axes γ . Since the fast axis of the QWP is arranged to be parallel to the major axis of the reflected ellipse, the major and minor axes of the ellipse are again brought into phase to give plane polarised light. The azimuth of this 'compensated' plane polarised light, will therefore be at an angle γ to the major axis of the ellipse. To simplify the experimental procedure the QWP is locked with its fast axis at 45° to the plane of incidence. This ensures that the amplitude of the reflected p and s components are equal i.e. Ep = Es.

The ellipticity γ is related to the phase difference $\triangle$ between the p and s components, where in general

$$\tan \triangle = \frac{\tan 2\gamma}{\sin 2\times}$$

and since $x = 45^{o}$ $\sin 2x = 1$

$$\tan \Delta = \tan 2\gamma$$

then $$\Delta = 2\gamma$$

The azimuth of the compensated light is $45 + \gamma$, so that the azimuth of the analyser in its extinction position will be $45 + \gamma = x$ with respect to α_s, the perpendicular to the plane of incidence,

since $$x = 45 + \gamma = 45 + \frac{\Delta}{2}$$

$$\Delta = 2x - 90$$

The value for the film thickness is then obtained by computing the experimental values Ψ and Δ together with the optical constants obtained from existing literature and the angle of incidence also obtained experimentally (Section 3.4.6)

3.4.5 Ellipsometric experimental technique

The first step in setting up the ellipsometer is to correctly align the axis of the polariser and analyser since this is critical for the accurate determination of the optical constants of the surface. With the QWP initially removed from the experimental arrangement, the four extinction settings i.e. positions of minimum light entering the photomultiplier tube, corresponding to the two parallel and perpendicular axes - generally known as reference azimuths - were obtained. These reference azimuths, expressed relative to the plane of incidence, were later used to evaluate the Ψ and Δ values. The 'bracketing technique' (85)

was used to obtain the necessary extinction setting, whereby the analyser and polariser were set to give equal intensities of light on each side of the minimum so that the average of the two readings would be taken as the true minimum. These extinction settings were in all cases obtained by alternate adjustment of the analyser and polariser until minimum light transmission occurred. The QWP was then replaced in the analyser area of the ellipsometer and reference azimuths for the QWP corresponding to the transmission axis of the polaroids being parallel and perpendicular to the plane of incidence obtained. This was done by setting the polariser and analyser to a pair of related extinction positions and rotating the QWP through the minimum. Extinction by the analyser only occurs when light emerging from the QWP is plane polarised and for this to be so either the fast or slow axis of the QWP has to be parallel to the plane of incidence. To determine Ψ and Δ the QWP was locked at 45^{o} to a reference position and extinction positions obtained both before and after in situ treatment, again employing the 'bracketing technique'. These values were then used for film thickness computations as indicated in Section 3.4.1.

3.4.6 Measurement of angle of incidence

The angle of incidence was determined by removing the elector and replacing it with a small telescope. Four pointed spikes mounted on saddles were positioned on the ellipsometer benches as illustrated in Figure 3.16 so that they were all in line with the illuminated pin as seen through the telescope. The distances between the points were accurately measured and the angle of incidence, ϕ calculated by simple trigonometry.

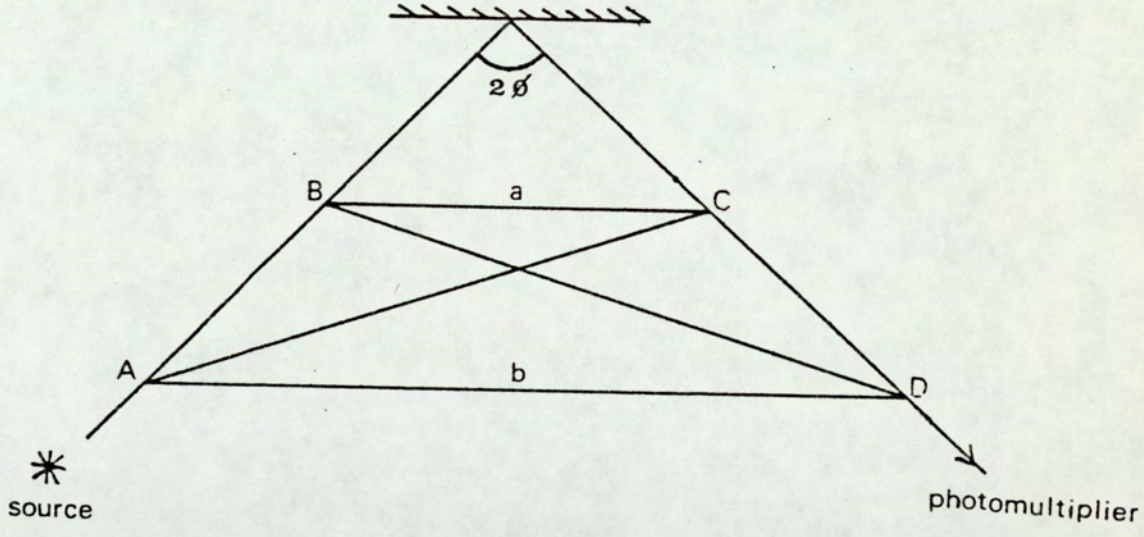

Figure 3.16 : Arrangement for measuring the angle of incidence

3.5. Experimental procedure

3.5.1 Specimen construction and surface preparations

The electrode materials selected for studying the impact behaviour of low velocity carbonyl iron and gold microspheres were machined to the required profile ready for mounting in the rotatable spoke (see Section 3.1.5) and as illustrated below.

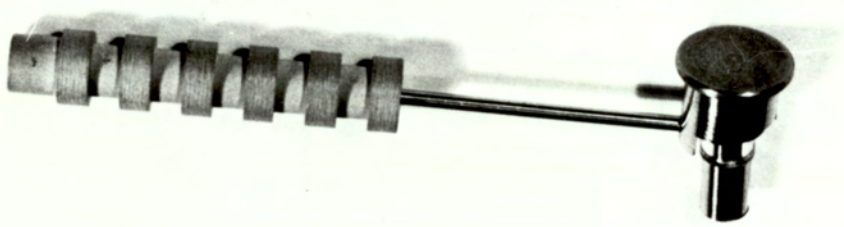

Figure 3.17 : Target mounting

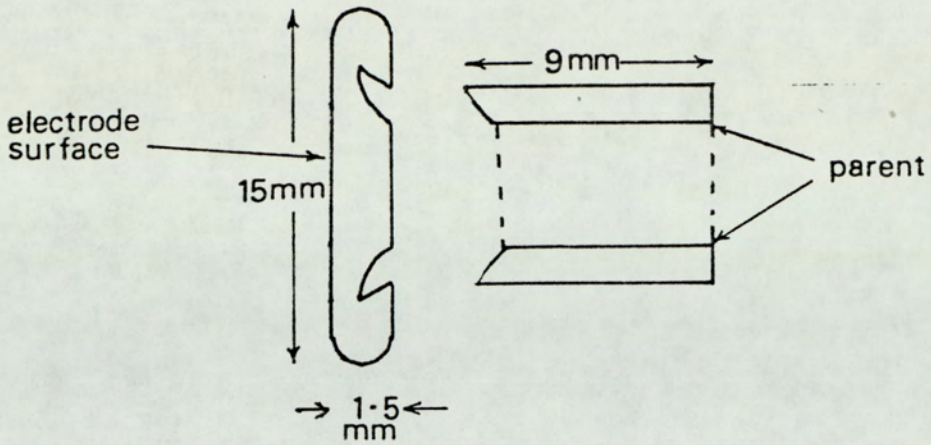

Figure 3.18 : Target construction A

The initial construction of the machined electrode detailed above was found to be of a design which was unable to provide adequate mounting strength between the target electrode and its parent mounting when subjected to very high temperatures. This resulted in the detachment of the electrode surface from the parent during in situ electron beam heating of the target. To overcome this problem the above constructional design was modified to that illustrated in Figure 3.19.

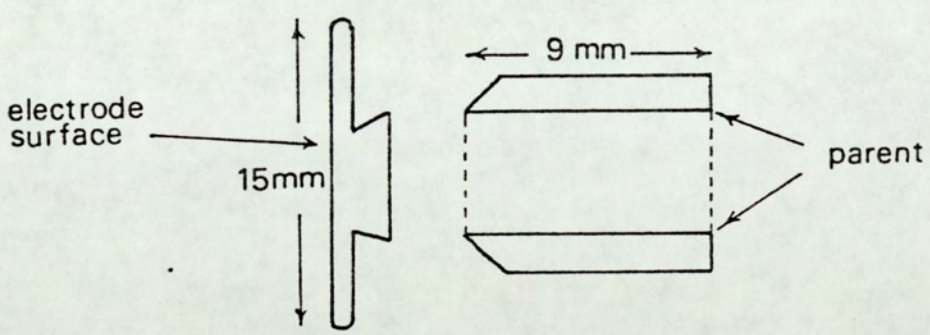

Figure 3.19 : Target construction B

This new design was found to provide the adequate mounting strength necessary for certain in situ surface treatments described later.

i) Commercial polishing

All target electrodes were subjected to metallurgical polishing prior to any additional surface preparation. To obtain a mirror finish on the freshly machined specimens it was necessary to start the polishing sequence at 600μm and finish it with a $\frac{1}{4}$ micron diamond paste. These were then rinsed ultrasonically with acetone, alcohol and deionized water to remove any residue diamond particles. Such a surface can now be assumed to consist of a microtopography characterized by a random array of grooves having typical dimensions of 0.1μm and other irregular features of larger dimensions.

ii) Electropolishing

This treatment was only applied to Ti 318 and Ti 115 specimens that were already in a 'commercially' polished state since metallurgical experience shows that the best results are usually obtained with relatively 'clean' surfaces. The electrolyte used was one recommended by Jacquet (86) of 1000 ml of glacial acetic acid and 60 ml of perchloric acid of specific gravity 1.54. This electrolyte bath avoids difficulties normally associated with the perchloric acid techniques i.e. its explosive tendencies are decreased and no particular precautions are necessary whilst mixing the acids. The electrolytic cell consisted of a glass tank, containing the electrolyte in which was suspended a titanium sheet cathode having an area greater than that of the target electrode. The anode and cathode were placed between 2 and 4 cm apart and the current which was allowed to flow for 2 - 3 mins was taken from the D.C. mains through a large resistance in series. The electrolytic

solution was stirred continuously with a glass stirrer to maintain the homogeneity of the solution.

iii) Evaporated specimens

To ensure even evaporation of a material on to the substrate, commercially polished specimens having reasonably flat surfaces were used. Copper was used as the most suitable substrate material for rigid transference to minimise the risk of the detachment of the thin evaporated films during their intense electron beam heating. The films of approximately 1000 Angström thickness were evaporated in a subsidiary vacuum system at a chamber pressure of between 10^{-6} and 10^{-7} mbar.

iv) In situ surface cleaning procedure

In addition to the above mentioned target surface states some of the specimen surfaces were subjected to in situ argon ion bombardment and electron beam heating using the facilities described earlier.

These surface cleaning procedures were carried out by rotating the target into the 'service' position in the lower part of the experimental chamber as illustrated in Figure 3.2 and monitoring the film thickness by using the ellipsometric facility described in Section 3. On completion of this 'cleaning' procedure the targets were rotated back to the 'test' position in the upper part of the chamber in readiness for carrying out the particle impact study.

The argon ion cleaning process involved the target surface to be etched with argon ion for approximately 1½ hours at a pressure of $\sim 10^{-6}$ torr when from ellipsometric analysis it was assumed that the target surface was atomically clean. The ion etching process however would leave a 'rough' surface consisting of many grooves and protrusions. The electron bombardment which involved heating the target specimen to $\sim 800^{\circ}$ C at an ultimate pressure $\sim 10^{-7}$ mbar whilst acting as an additional in situ surface cleaning mechanism also had the effect of annealing the ion etched surface.

3.5.2 Target surface notations

The following notation for the characterisation of the various surface states mentioned above will be used throughout the remainder of this thesis.

Commercially polished surface - - - - - State A

Argon ion bombarded surface - - - - - - State B

Electron beam heated surface - - - - - State C

Electropolished surface - - - - - - - - State D

Evaporated surface - - - - - - - - - - State E

3.5.3 Experimental procedure for particle bouncing measurements

All measurements were carried out in the 'test' position in the upper part of the experimental chamber illustrated in Figure 3.2. Prior to any measurement being taken the gun voltages required to produce an 'optimum' flux of microparticles

was obtained. In addition, a negatively biased power supply in series with a large resistance of $\sim$ 80 M ohm to prevent flashovers was used to provide a variable target potential V_T. The electrode gap separation, d ,of between 2 and 5 mm (Figure 3.20) was obtained by careful adjustment of the set of externally marked bellows in conjunction with a vernier telescope whilst looking through the view ports. On achieving the optimum conditions, the microparticle gun was used to fire single paraxial particles into the high field test gap as shown in Figure 3.20.

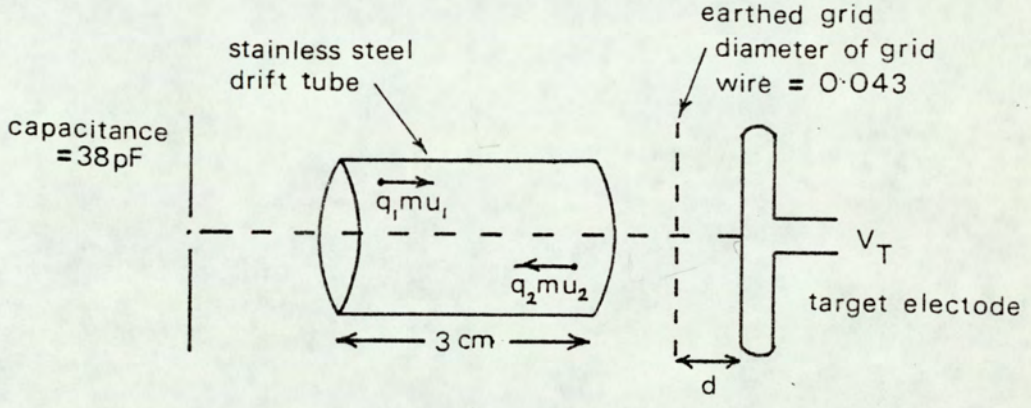

Figure 3.20 : High field test gap

d = electrode separation

m = mass of microparticle

q = charge on microparticle

Every particle undergoing charge reversal and subsequent reflection from the target electrode constituted an event and each event was recorded and displayed as two sequential trapezoidal pulses (see below) on a Hewlett Packard storage oscilloscope.

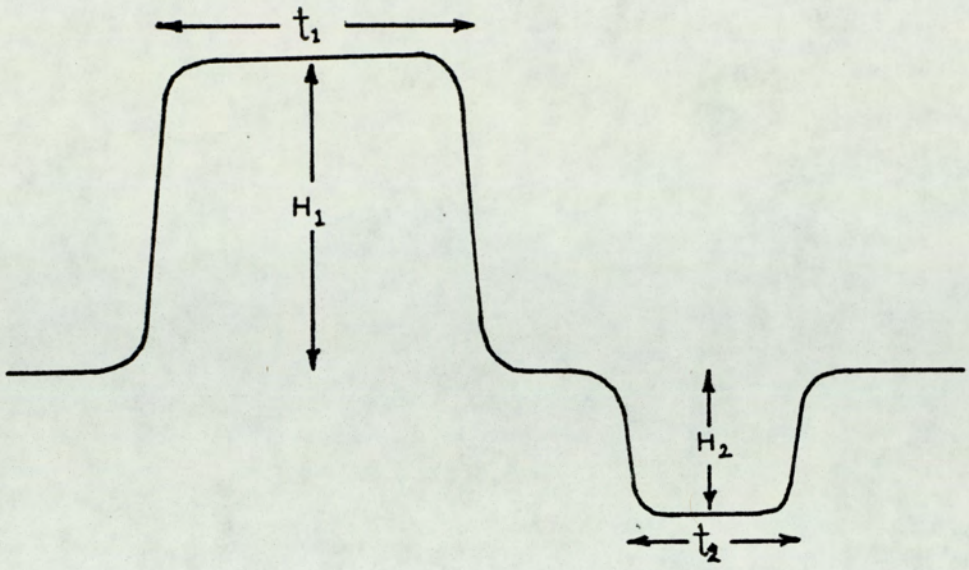

Figure 3.21 : Oscilloscope signal

This enabled the measurement of the height, width and various parameters such as velocity and charge of the incident and returning particle.

The observed initial velocity of the microparticle before entering the high field gap = u_1 and is given by

$u_1 = \frac{L}{t_1}$ where L is the length of the drift - tube.

Similarly the final velocity on leaving the gap = V_2

so that $v_2 = \frac{L}{t2}$ - - - 3.10

Using the classical equations of motion, the impact velocity of the particle on the target U_2 is thus given by

$$u_2^2 = u_1^2 + 2a_1d \quad \text{- - - 3.11}$$

where d = width of high field test gap

and $a_1 = \frac{qi}{m} \frac{V_T}{d}$

where qi and m are charge and mass of incident particle

and V_T = target potential

Similarly the rebound velocity of the reflected particle is given by

$$v_1^2 = v_2^2 - 2a_2 d$$

where $a_2 = \frac{q_2}{m} \frac{V_T}{d}$

The charge ratio of the incident to reflected particle is obtained from the two heights of the trapezoidal pulse

$$\text{giving} \quad \frac{q_1}{q_2} = \frac{H_1}{H_2} \qquad \text{- - - 3.12}$$

These values were later fed into a specially written computer program (Appendix 2) so that the particle size, mass, charge and other relating parameters such as the ratio charge to mass and the coefficient of restitution could be evaluated. For every measurement being undertaken approximately fifty such bouncing events were recorded.

On completing the impact studies on a given target careful stereoscan examination of each target surface using a Cambridge 600 electron microscope was carried out. Micrographs were obtained for each target surface and further examination of the surfaces was carried out to identify any substantial alteration in the microstructure of the target electrodes.

3.6. Measurement of contact time

Referring to the theoretical considerations in Section 2, it can be seen that the time of contact between the microsphere and target electrode plays a major rôle in determining the magnitude of charge exchanged. It therefore seemed appropriate to try and devise a method of measuring this contact time. To facilitate this measurement and to gain some idea of the problems involved, a macroscopic analogue was set up. This involved the use of a large spherical ball bearing ($\sim$ 1 cm diameter) charged to a high potential ($\sim$ 60V) which was then allowed to collide with a plane surface constituting the target electrode. To monitor such an event, an amplifier was attached to the target and the resulting signal recorded on a storage oscilloscope. This had the general form illustrated in Figure 3.22 and shows in region (i) the approach of the charged sphere to the target, in (ii) the dwell or contact time tc and in (iii) the bouncing particle receding from the target. However, to resolve tc it

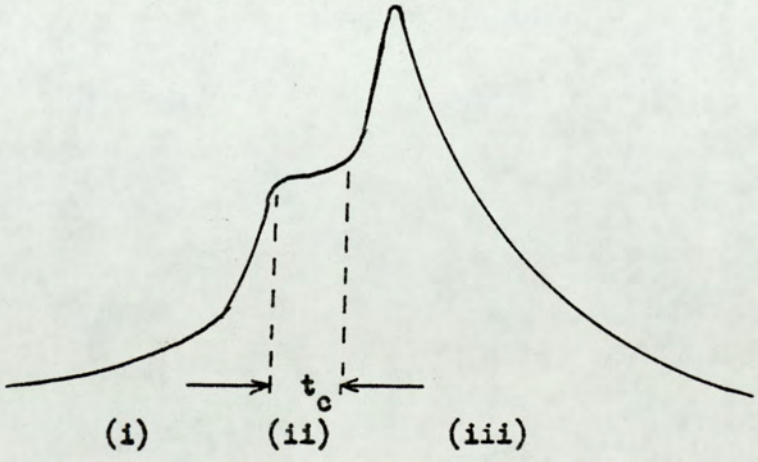

Figure 3.22 : Contact time signal for macroscopic analogue

was found necessary to use an artificially 'soft' target in the form of a weak leaf spring, since for solid targets, tc was found to be $<$ 1 microsecond and difficult to discriminate

from the noise and pick - up inevitably present with such a crude arrangement unless special precautions are taken. It should also be noted that the final spike arises from a capacitative effect associated with the particle dumping off its charge on the target. Having thus established the viability of such a technique, attention was turned to realising a similar regime on the microscopic scale.

As previously, the approach followed was to add a second voltage-sensitive amplifier to the target electrode, as illustrated in Figure 3.23, so that it was possible to record the approaching impacting and receding particle.

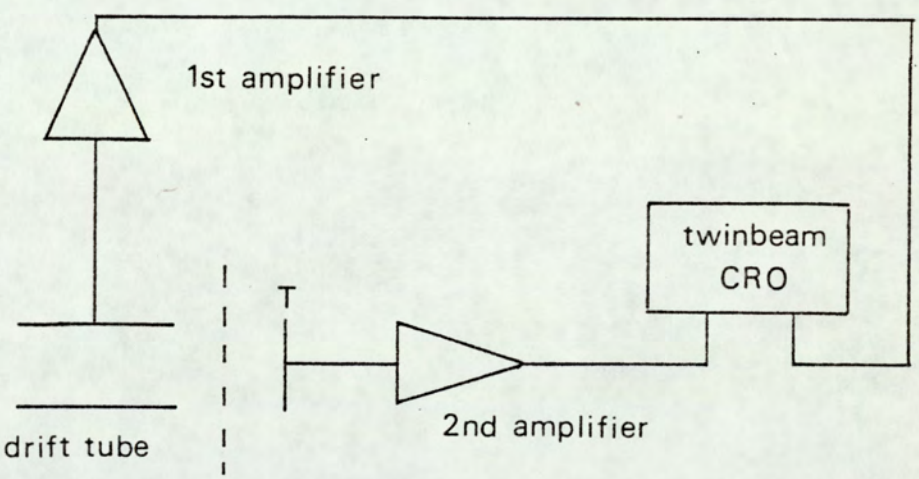

Figure 3.23 : Twin amplifier system

By using the twin - beam facility of the Hewlett Packard storage oscilloscope, it was possible to record consecutive traces of the microsphere i) passing through the drift tube and ii) impacting on the target electrode. Since however the contact time in the present investigation is assumed to be of the order of micro-seconds or less which is very much faster than the normal

millisecond sweep speed used for recording drift tube traces it was necessary both for the oscilloscope to be operated on a fast scan speed and to use the built in trigger delay facility set to a point high on the leading edge of the target signal.

The basic requirement of the target amplifier was that it should be capable of recording sub-microsecond signals. Since it also had to be a FET input device for satisfying the input impedance requirements for detecting charges $\leq 10^{-15}$C(see Section 3.1.4), considerable problems were encountered in its design; in particular these were associated with electronic noise, shielding and the effective input capacitance of the device. The final amplifier selected for recording the target signal employed on ultra fast FET operational amplifier (LH 0032 C) which has a high slew rate, high input impedance and a bandwidth of approximately 100 MHz with a rise time of 10 - 100 microseconds. Figure 3.24 shows the arrangement of this device as a target amplifier.

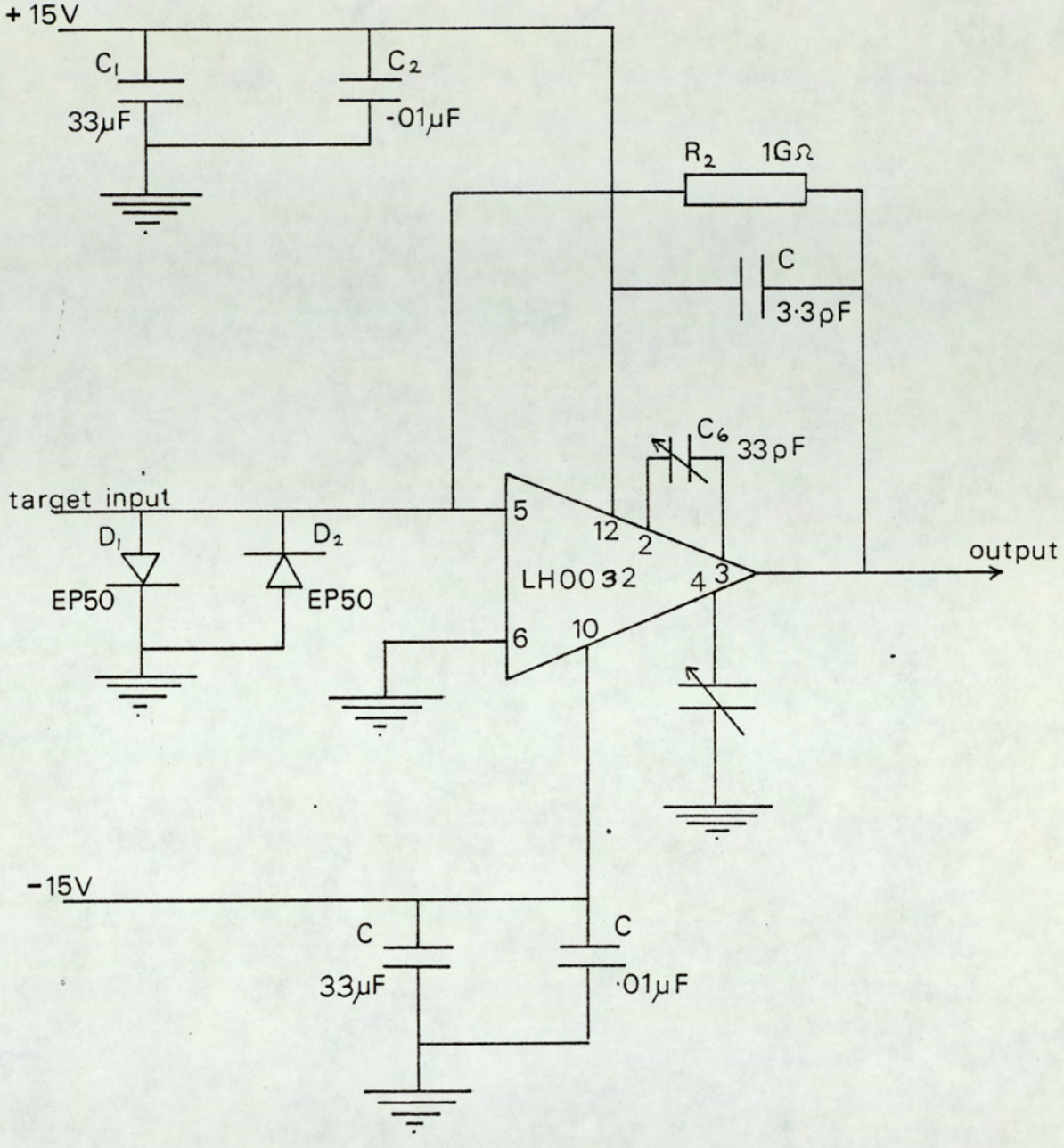

Figure 3.24 : Voltage sensitive target amplifier

Although it had been hoped to measure the contact time of the microparticles bouncing in a high voltage gap by isolating the amplifier via a blocking capacitor as shown in Figure 3.24, it was found impossible to stabilize the EHT supply sufficiently to reduce the noise level to an acceptable level for detecting the small signal generated by the impacting particle.

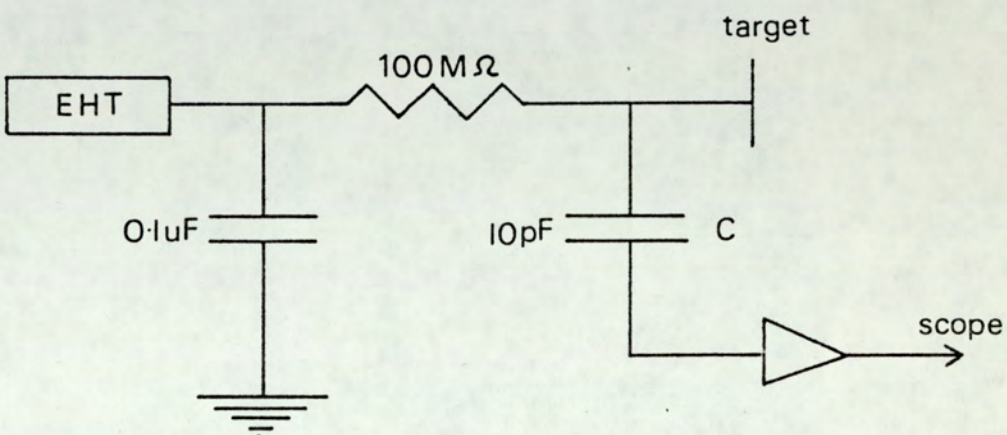

Figure 3.25 : Target amplifier isolation arrangement

Accordingly, it was decided to restrict measurement to a zero-field regime. It should be noted therefore that the only events that may be observed are those in which either no charge exchange has taken place or where the particle sticks to the target. Figures 3.26 and 3.27 are schematic representations of the expected traces from the twin amplifier system of Figure 3.23 for such events. It should also be noted that the difference between the target signals of Figures 3.22 and 3.26 for the macro and micro bouncing events can be explained in terms of the differing capacitative effects associated with the two regimes. Whereas in the former case, the capacitance of the sphere is comparable

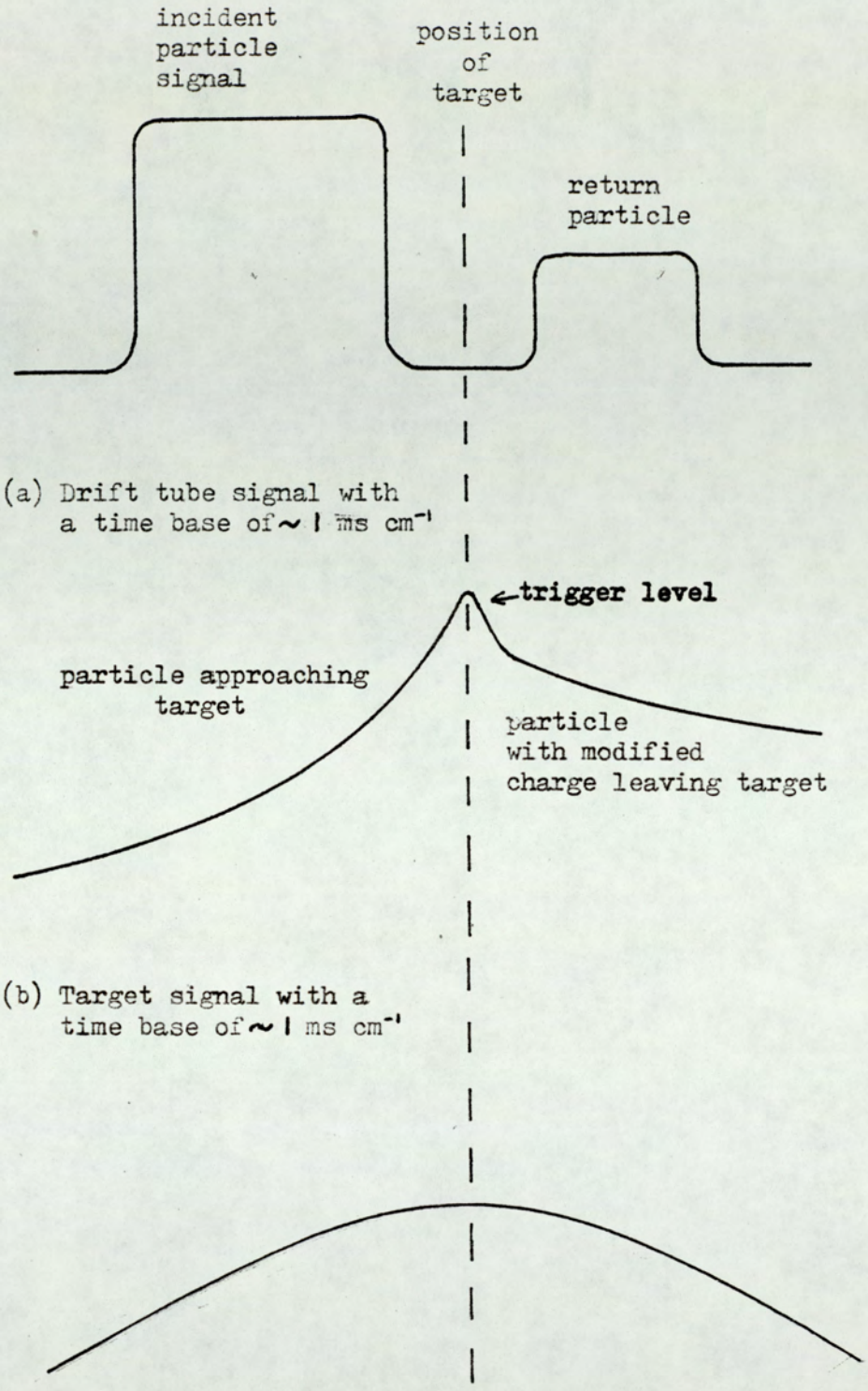

Figure 3.26 : Particle 'Bouncing' event

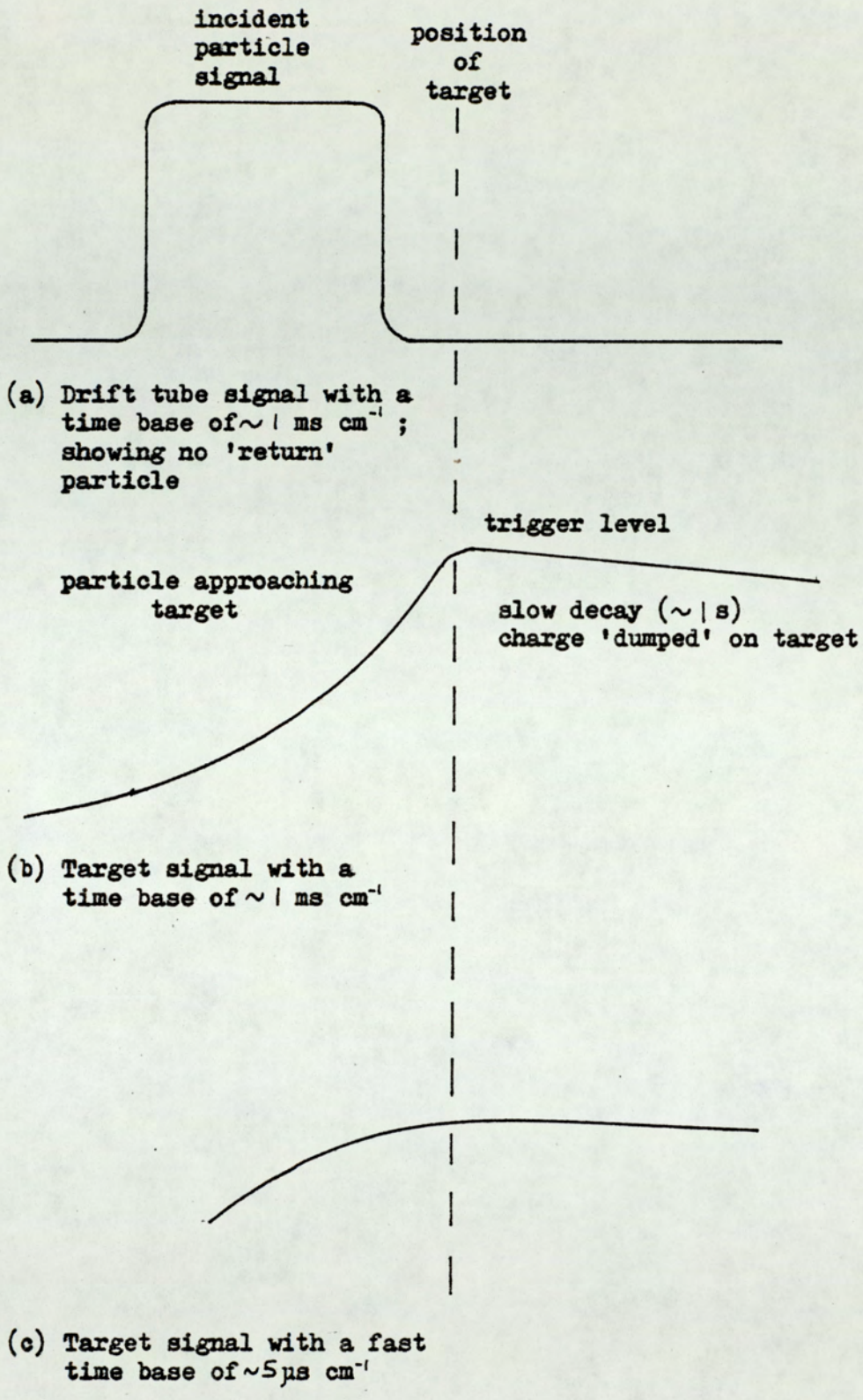

Figure 3.27 : Particle 'sticking' event

to that of the target, in the latter it will be very small and therefore have little influence on the shape of the signal.

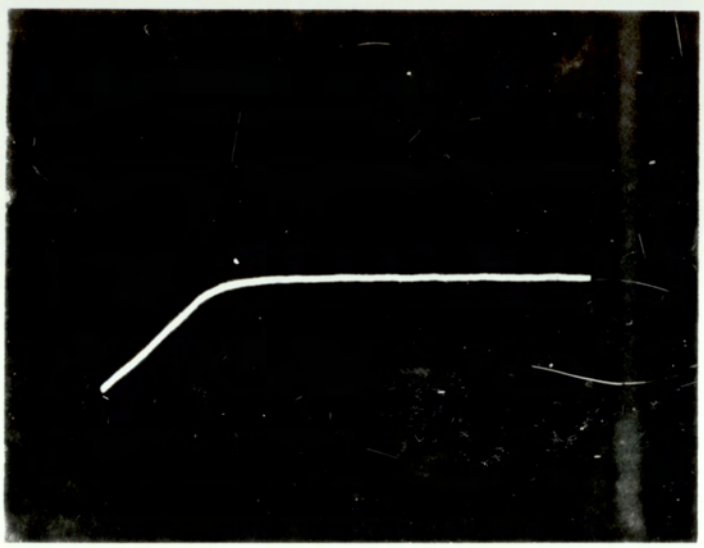

Figure 3.28 : Oscilloscope trace with a fast time-base of $\sim 5\mu s$

Figure 3.28 illustrates the actual type of trace that was consistently obtained in the present investigation. Since it is similar to the expected trace for a sticking event shown in Figure 3.27 (c), and because no return particle was observed on the drift tube trace, it was concluded that the particle bouncing phenomenon did not occur for this type of zero - field regime.

In fact, it has since been confirmed (87) that for target surfaces such as titanium, copper and stainless steel, it is typical for over 99% of low velocity particles to stick to these surfaces under zero - field conditions. This would therefore indicate that even at subcritical velocities, the impact at zero - field is not always elastic, but that more complicated processes are involved whereby the particle is able to weld to the surface and is only pulled off when there is a high field present. One possibility is that in - flight field electron emission raises the temperature of the particle surface sufficiently to cause local melting and hence welding on impact.

In conclusion, it has to be said therefore that even though a suitable technique for measuring the contact time was developed, it was not possible to apply it since no particle bouncing events were observed with the experimental conditions used.

CHAPTER 4

4.0 Results

The major part of the present investigation was dovoted to a fundamental study of the low velocity, bouncing impact behaviour of positively charged micron sized spheres. In general, particles that undergo such an event under high - field conditions also exhibit charge reversal so that the signal recorded from the drift tube detector of Figure 3.20 appears as illustrated in Figure 4.1, i.e. as two sequential trapezoidal pulses of opposite sign, corresponding to the passage of the incident and reflected particle.

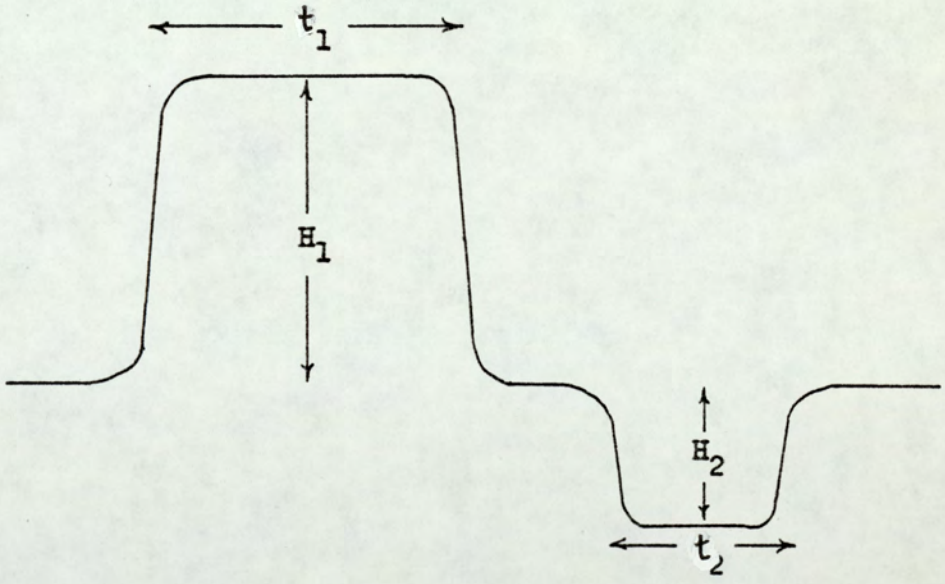

Figure 4.1 : Oscilloscope signal

From the heights H_1 and H_2 and the durations t_1 and t_2 of these pulses it is possible to calculate the charge and velocity of the incident and reflected particle using the equations

mentioned in Section 3.5. However, since this would have been a tedious and time consuming procedure if performed 'manually' for each of the many thousands of events, a computer program specially written around these four input parameters was used: details of this are given in Appendix 1. Apart from drastically shortening the processing time of the impact data, this program also provided additional data such as the microparticle mass, radius and charge to mass ratio. From this data the mechanical and electrical aspects of individual impact events have been analysed respectively in terms of the coefficient of restitution or e - values, and the ratio q_2/q_1 of the reversed to the initial charge or Q - values.

From the theoretical considerations discussed in Chapter 2 it is clear that the most important parameters affecting the charge reversal process are i) the particle, charge and its impact velocity, ii) the combination of the particle and target materials and iii) the microscopic state of the target surface. Accordingly, four main lines of investigation have been followed in these studies. Firstly, the impact behaviour of carbonyl iron microspheres on targets of the two titanium alloys, Ti 318 and Ti 115 has been recorded for surface states designated as A, B, C and D, where state A refers to a commercially polished surface, B to an ion etched surface, C to an electron beam heated surface and D to an electropolished surface. (The preparation and monitoring procedures of these states has been detailed in Section 3.5). Secondly data has been obtained for the impact of carbonyl iron microspheres on evaporated copper and

gold films. Thirdly, to represent the extremes of electrical stability and mechanical hardness of certain materials when used as high voltage electrodes, a comparison is also made of oxidised and atomically clean surfaces of copper, stainless steel and Ti 318.

Finally, detailed investigations have been made of the impact behaviour of various particle/electrode combinations so that the rôle of differing work functions on the charge reversal phenomenom as outlined in Section 2 can be studied. This has been achieved by the use of gold microspheres on commercially polished electrodes of Ti 318, nickel, copper and on an evaporated gold film as well as the impact of iron microspheres on the various targets as detailed above.

As stated already, the impact data obtained has been evaluated in terms of e and Q - values, representing respectively the mechanical and electrical aspects of the impact. Each experimental point on the following plots represents the average of approximately fifty individual particle impact events covering a range of particle velocities from 20 to 100 ms^{-1} and particle diameters from 0.5 to 5 microns so that the plots of figure 4.1 to 4.13 can be considered to illustrate the mean behaviour.

4.1 Mechanical responses

Figures 4.2 a and 4.2 b represent the variation of the coefficient of restitution e with the particle impact velocity v_i for the four different surface states of the two titanium

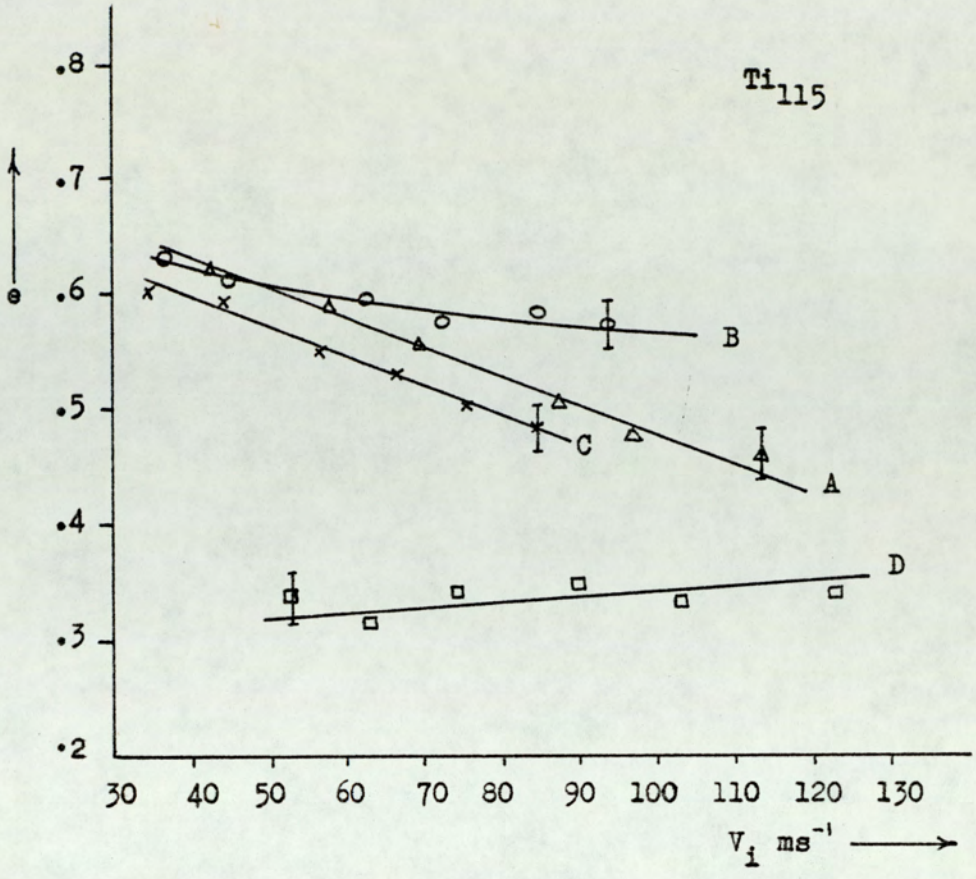

Figure 4.2a

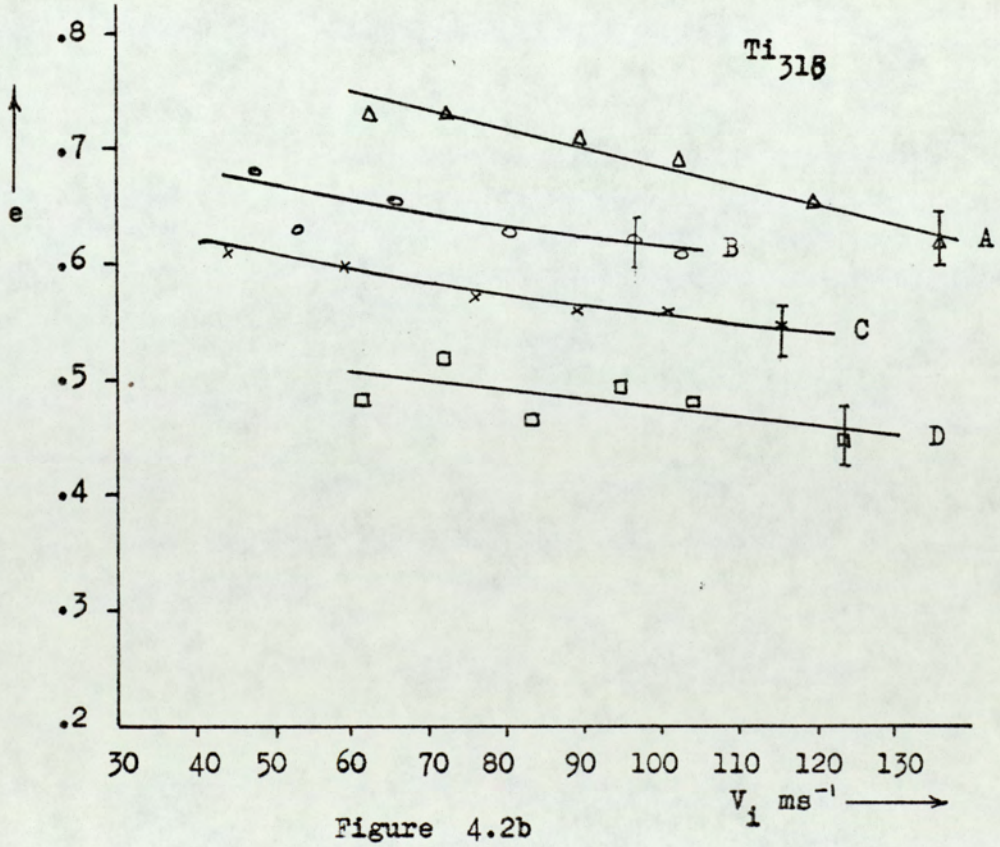

Figure 4.2b

alloys, whilst Figures 4.3 a and 4.3 b illustrate the variation of e as a function of v_i for oxidised and atomically clean surfaces of copper 1), stainless steel 2) and titanium 3) respectively. It can be seen that in general, for all cases, the e - value decreases with increasing particle impact velocity and that the e values of Ti 318 are much higher than those of copper and stainless steel. In addition, the relative microscopic hardness of all materials, as measured by the mean microscopic e - values have been found to be in good agreement with their corresponding macroscopic hardness values (44). Referring to Figures 4.2 a and 4.2 b it will be seen that the e - values for Ti 115 tend to be generally lower than those for Ti 318 and that the removal of the oxide film in the second case has resulted in a significant lowering of the e - values for each material. This is not entirely unexpected since it is well known that metal oxides generally exhibit much harder surfaces than their respective base metal substrates (88), hence promoting elastic reflections with higher coefficients of restitution.

The lowering of e - values with surfaces which are not commercially polished is also evident in Figures 4.2a and 4.2 b where it can also be seen that electropolishing results in a very much reduced e - value. Figures 4.4 a and 4.4 b represent data obtained by the impact of gold microspheres on commercially polished and atomically clean surfaces of copper (2), titanium(3), gold(4) and nickel(5) respectively. Again, whilst very similar trends to those mentioned previously are evident, it is clear

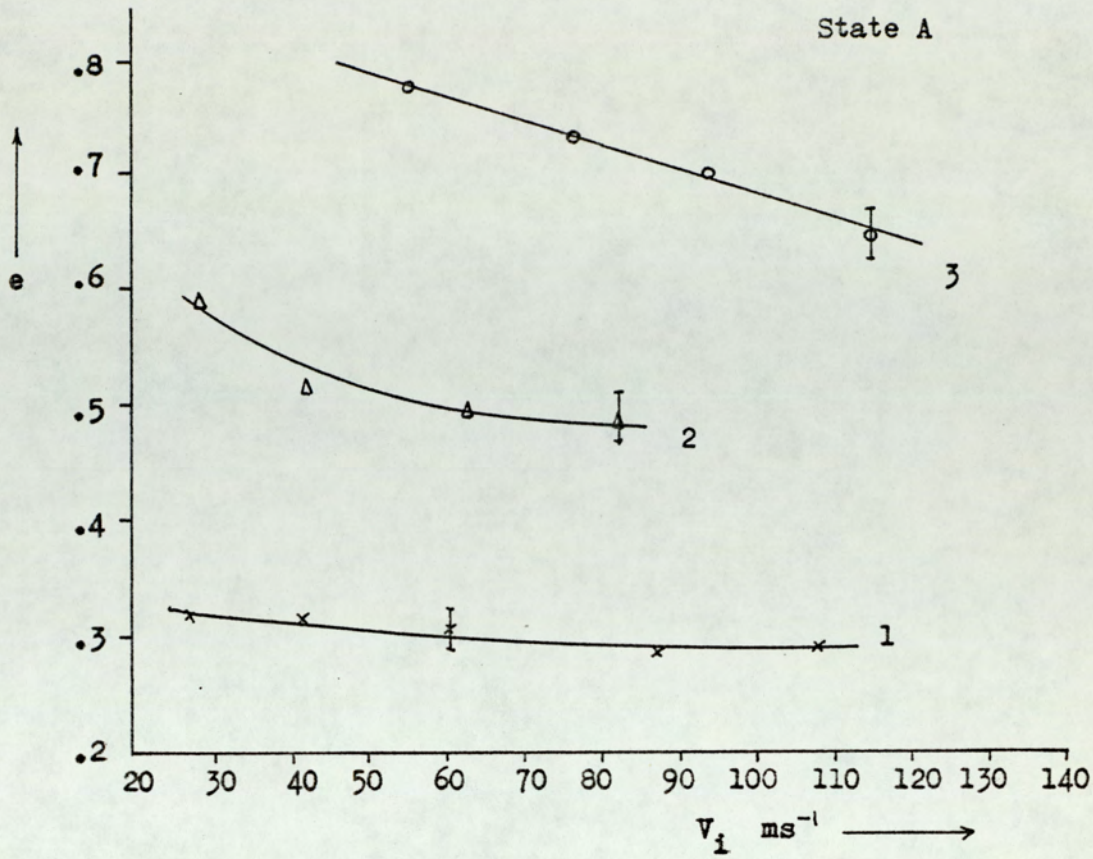

Figure 4.3a

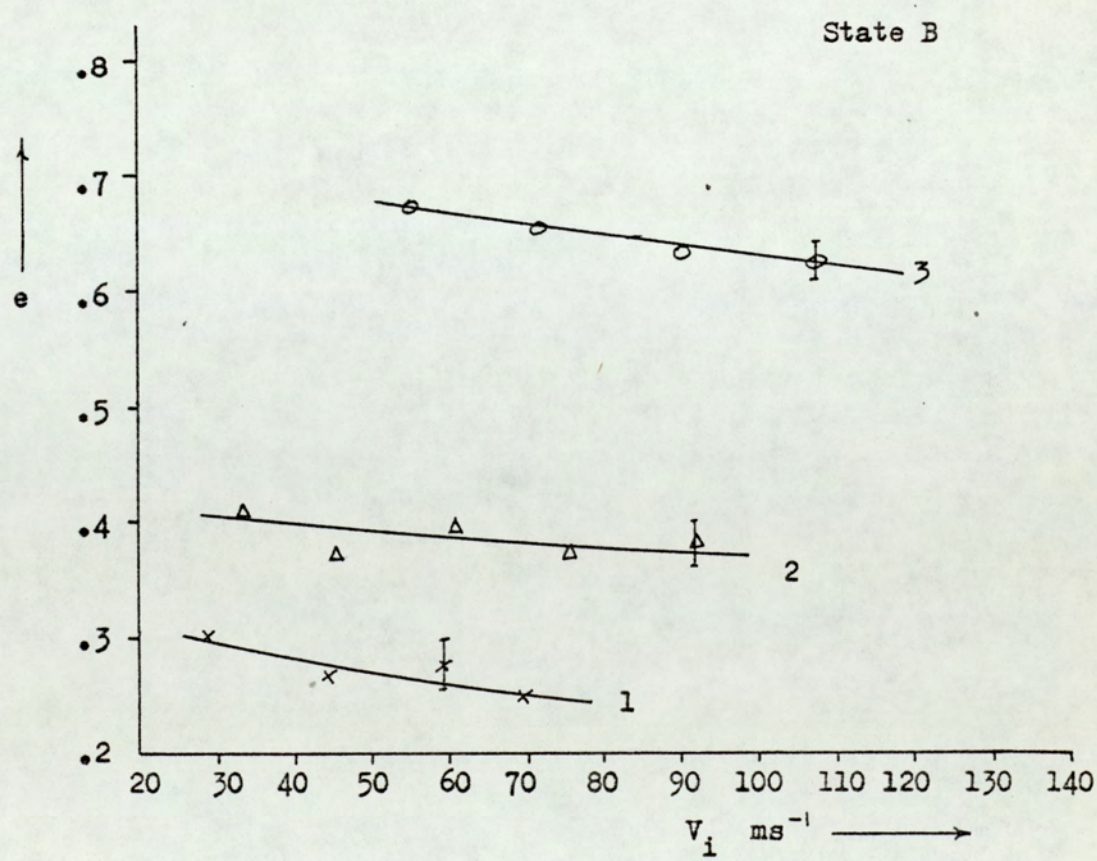

Figure 4.3b

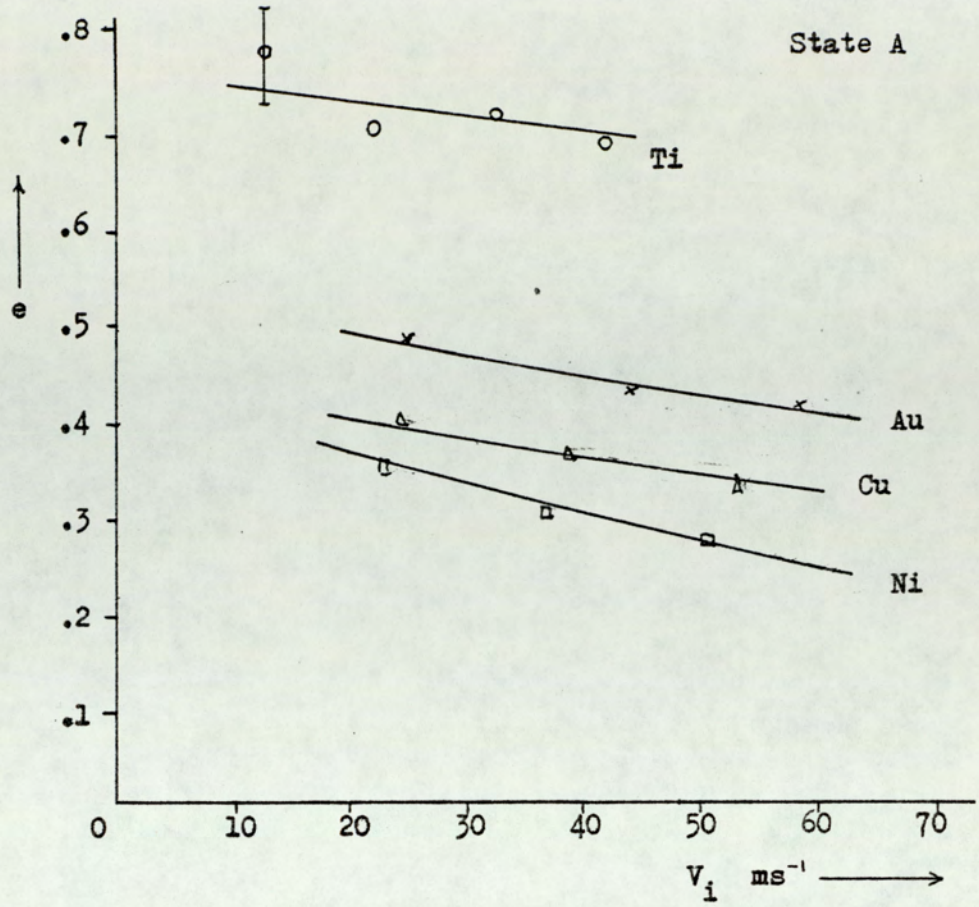

Figure 4.4a

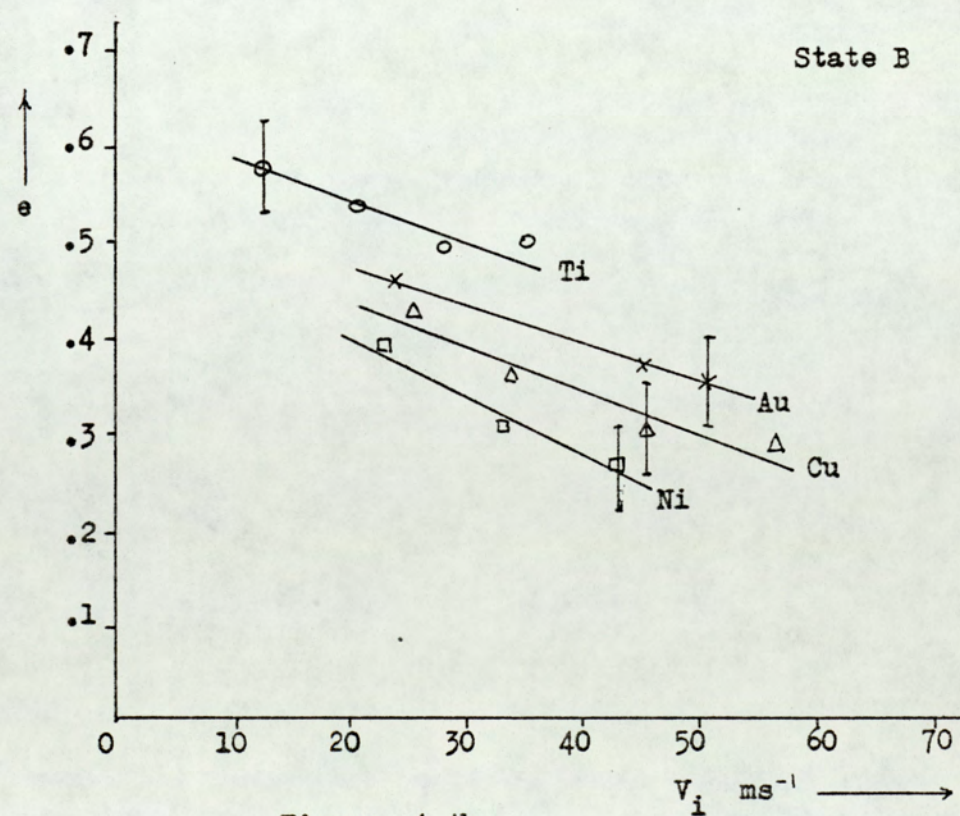

Figure 4.4b

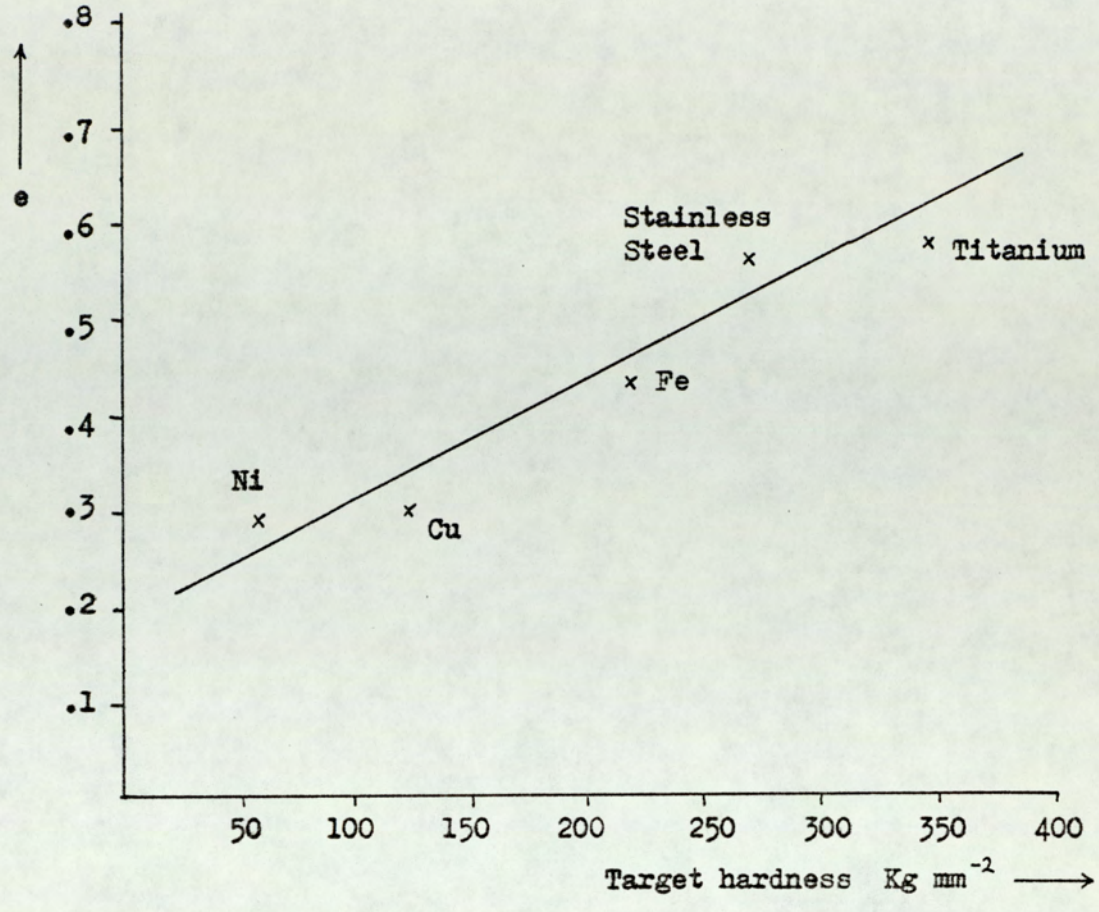

Figure 4.5

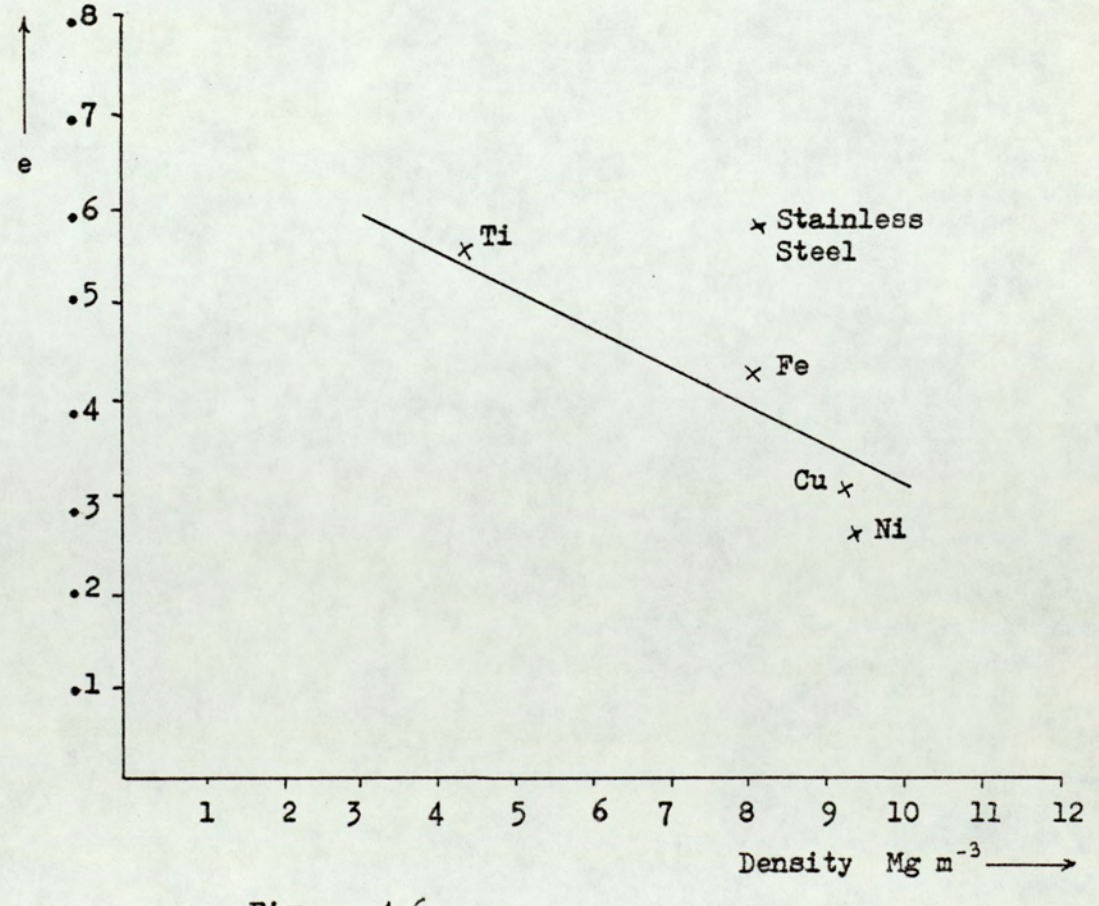

Figure 4.6

that, although titanium, nickel and gold appear to lead to a gradual lowering of the e - value, those of copper are subject to a much sharper lowering.

To compare the elastic behaviour of all target materials studied, their mean e - values as calculated from all impact events occurring within the velocity range 20 - 100 ms^{-1} have been plotted in Figures 4.5 and 4.6 as a function of a) the 'hardness value' of each material as measured directly on the Vickers scale and b) the density of each target material. The physical significance of the linearity of these two plots will be considered in Section 5.

Figures 4.7 and 4.8 illustrate the variation of the particle radius r with impact velocity v_i and the charge to mass ratio q / m for randomly selected titanium targets. An increase in incident impact velocity with 'smaller' particles is indicated in Figure 4.7 which is not entirely unexpected since it can be seen from equation 1.3 that larger particles are normally associated with lower velocities. An almost inverse relationship of r and q / m is indicated in Figure 4.8. Again this is not entirely unexpected since the charge q induced on a sphere varies with the radius by the relation $q \propto r^2$ whilst the mass varies by the relation $m \propto r^3$. Therefore as r increases, m will increase by a greater amount than q leading to a decrease in q / m.

Figure 4.7 : Variation of r with impact velocity

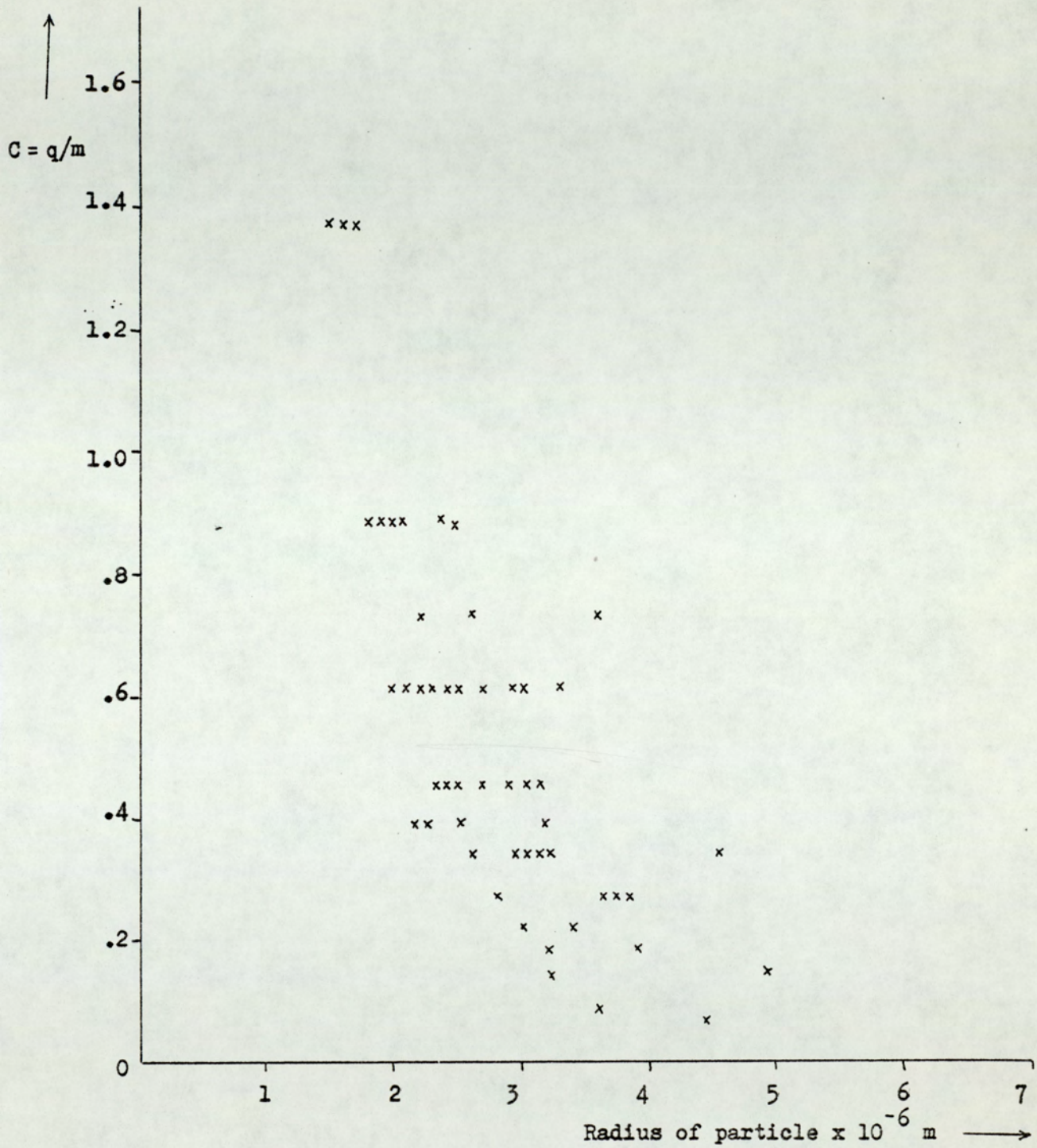

Figure 4.8

4.2 Electrical responses

The main charge reversal data obtained for the different surface conditions of Ti 115 and Ti 318 has been collated in Figures 4.9a and 4.9b respectively. In each case these plots show how the ratio q reflected / q incident i.e. $Q = \frac{q_2}{q_1}$ varies with the macroscopic field E, for target surfaces that are commercially polished (curve A), argon ion etched (curve B), electron bombardment heating (curve C) and electropolished (curve D). Again an averaging technique in presenting the data was adopted so that each point plotted in the foregoing figures represents a mean of approximately fifty impact events with the spread in the observations being accounted for in the error bars. Since high q_2/q_1 values correspond to efficient charge reversal, it follows from Figures 4.9a and 4.9b that for both target materials and for all surface conditions the exchange process is enhanced with increasing gap field. In addition, the responses obtained from the atomically clean surfaces of states B and C, indicate only slight differences for both alloys of titanium. Finally it should also be noted that there is a restricted range of the macroscopic E - fields for which measurements could be made on the atomically clean surfaces. For example, whilst $\sim$ 10 KV can be supported by a 2.5 mm gap with state A and D targets, only a $\sim$ 5 KV can be used for states B and C if breakdown of the gap is to be avoided. From Figures 4.10a and 4.10b which illustrate the variation of q_2/q_1 with the impact velocity, it can clearly be seen that the charge reversal process is inhibited at high impact velocities. Since high particle impact velocities are

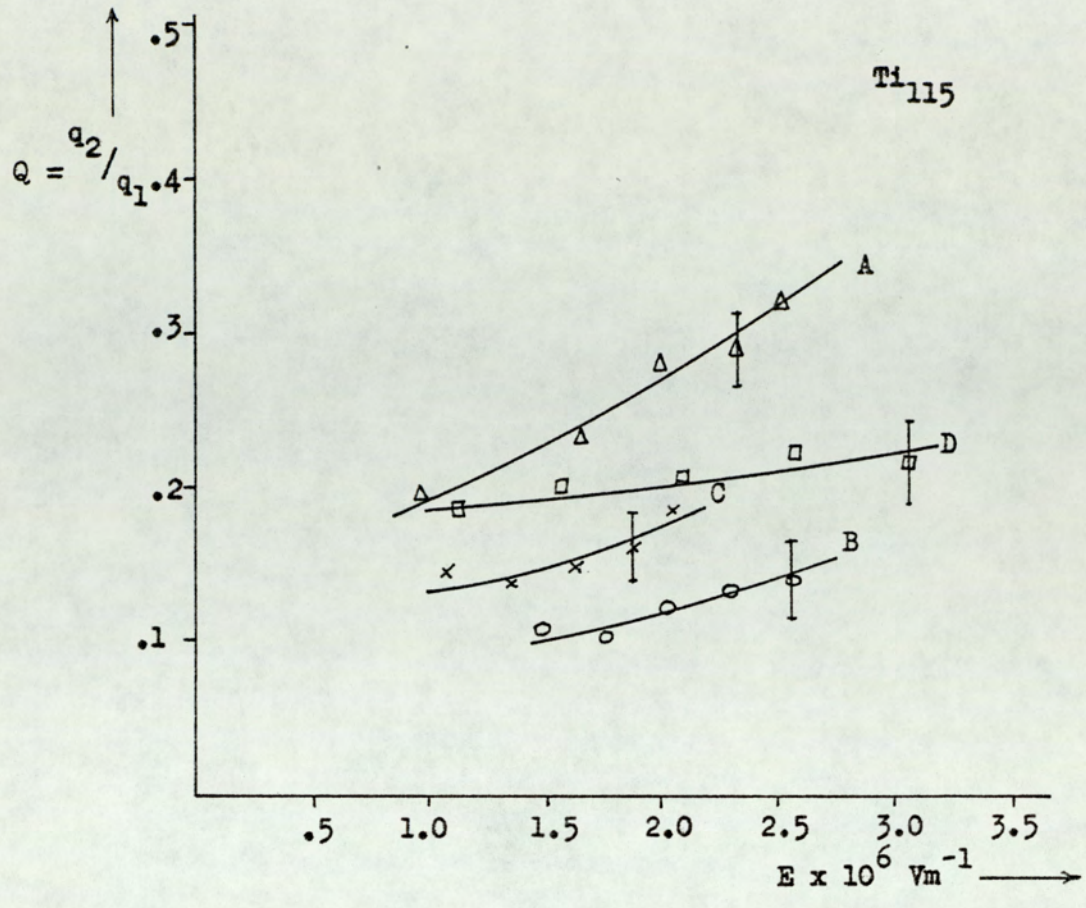

Figure 4.9a

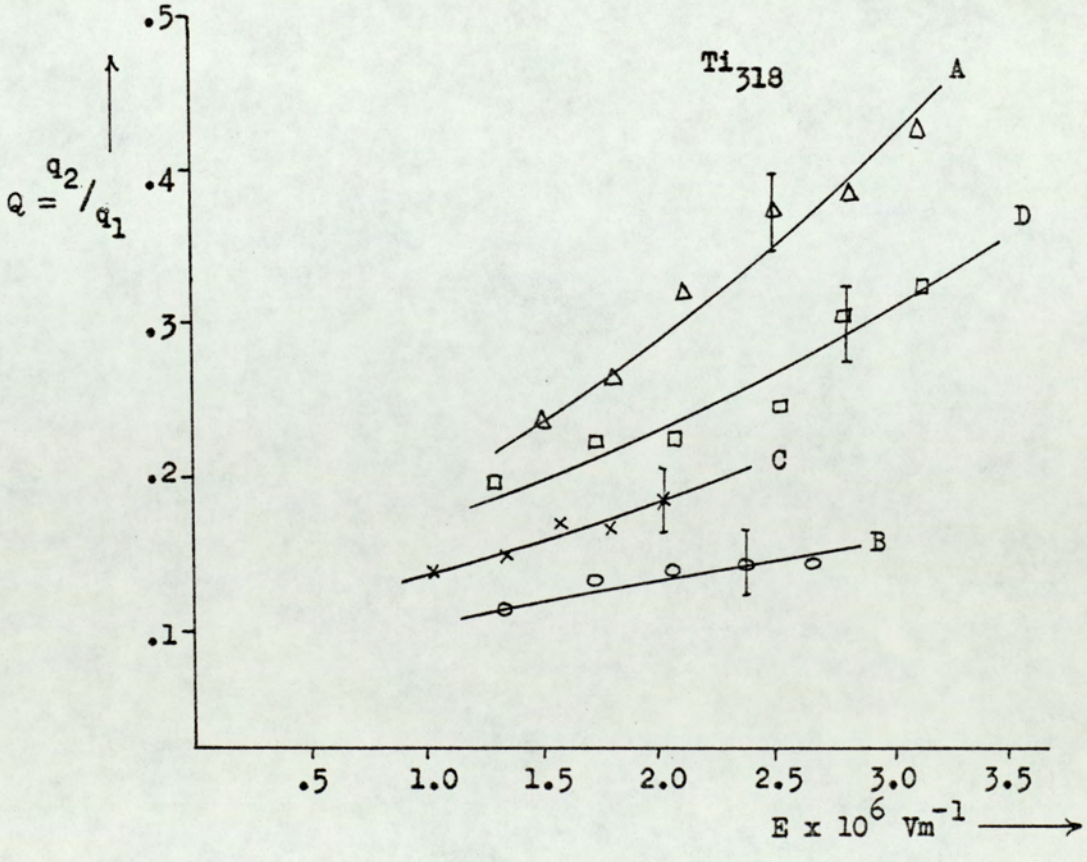

Figure 4.9b

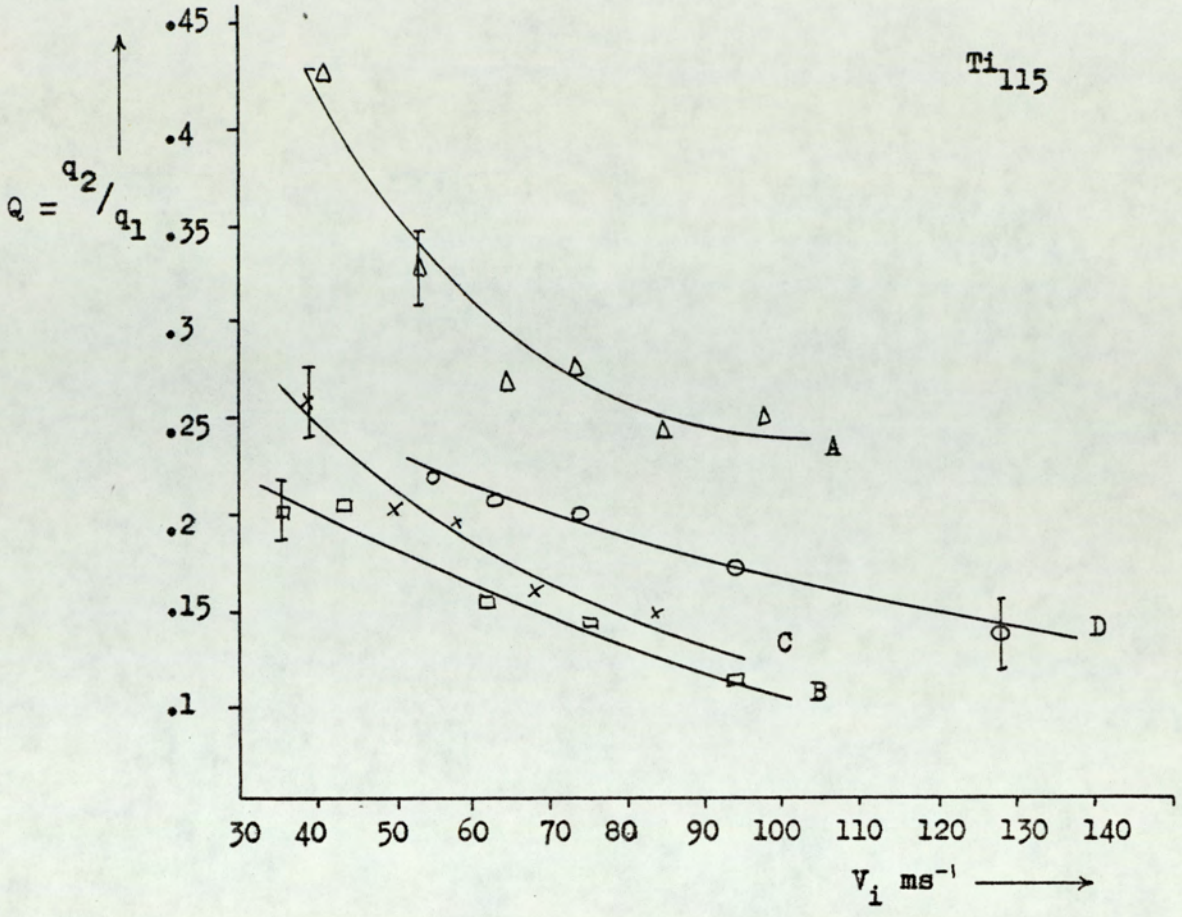

Figure 4.10a

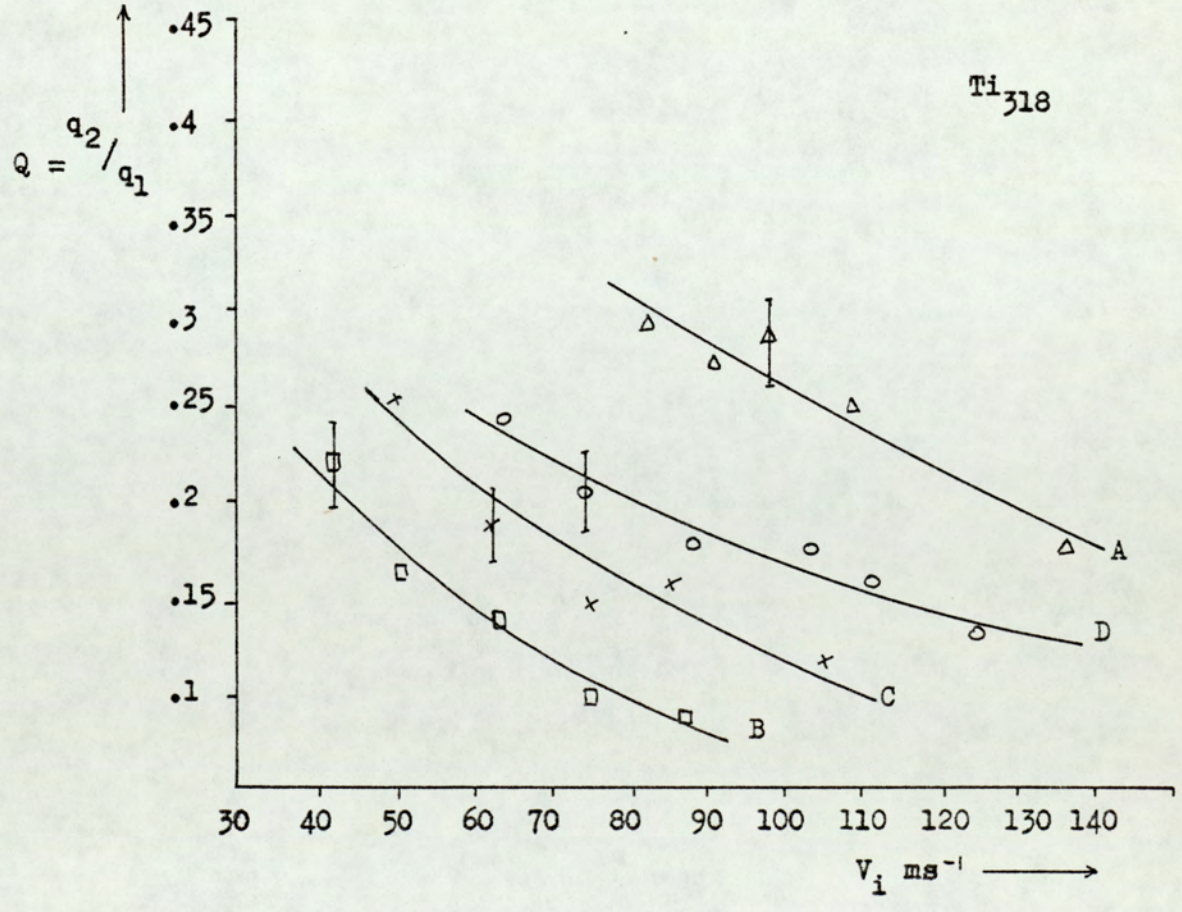

Figure 4.10b

associated with lower coefficient of restitution values (see earlier) it would appear that the impact behaviour is likely to be mainly inelastic resulting in a low energy enhancement.

Comparing now the charge reversal data for ambient oxidised (state A) and atomically clean (state B) surfaces of copper (1) stainless steel (2) and titanium (3) as illustrated in Figures 4.11a and 4.11b respectively, it can be seen that whilst the variation of q_2/q_1 with E is similar to that of the titanium alloys for state A, the removal of the surface oxide from the targets (state B - Figure 4.11b) results in the charge exchange process becoming more efficient for stainless steel and copper and less efficient for titanium. This is in contrast to the commercially polished surfaces of Figure 4.11a where titanium is clearly the most efficient in promoting the mechanism and stainless steel the least effective.

Figures 4.12a and 4.12b, and 4.13a and 4.13b represent the variation of q_2/q_1 with E and v_i respectively when gold spheres ranging in diameter from 1 to 5 micron were used as the microparticle impacting material. Again the general trend is for the charge exchange process to be enhanced with increasing gap field and decreasing impact velocity. However, whereas for copper and gold removal of the oxide layer has resulted in a slight enhancement of the exchange process, in the case of titanium and nickel the process appears to be inhibited.

Supplementary scanning electron micrograph evidence of the surfaces of various target materials used is illustrated in Figures 4.14

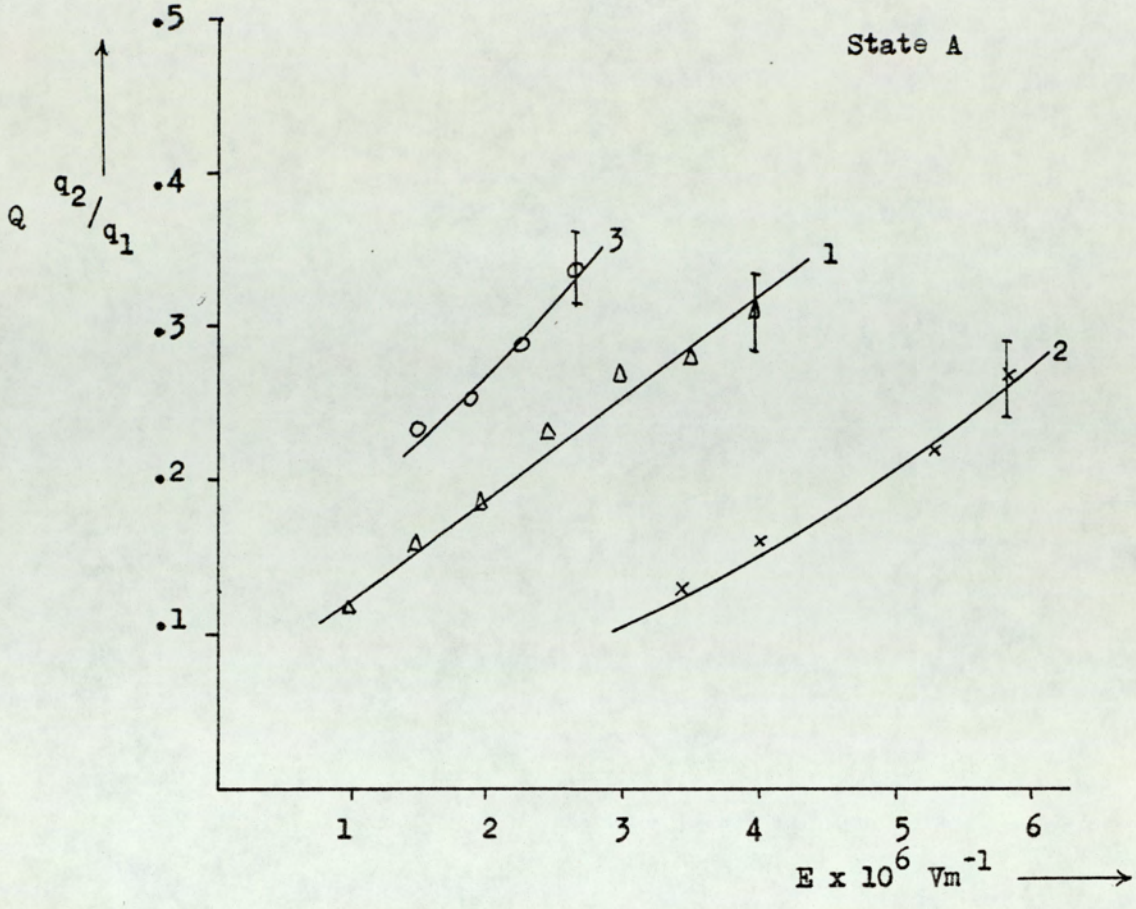

Figure 4.11a

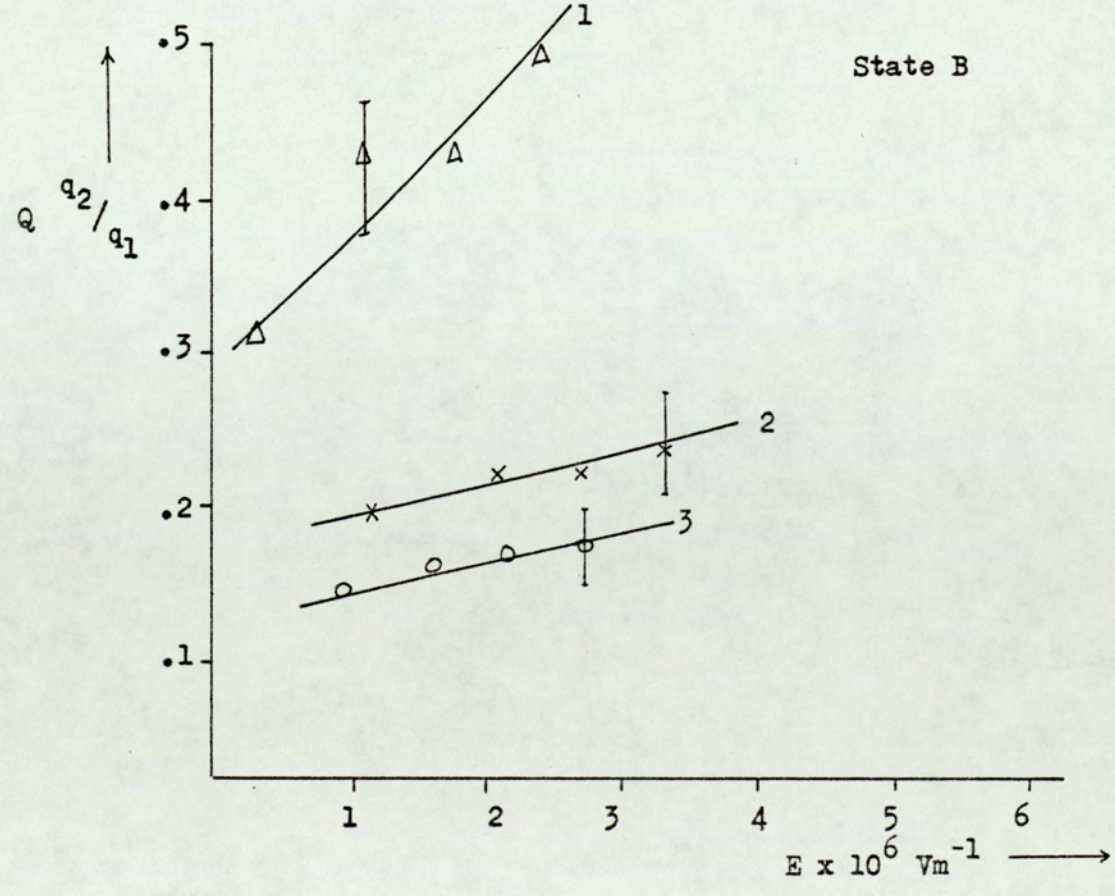

Figure 4.11b

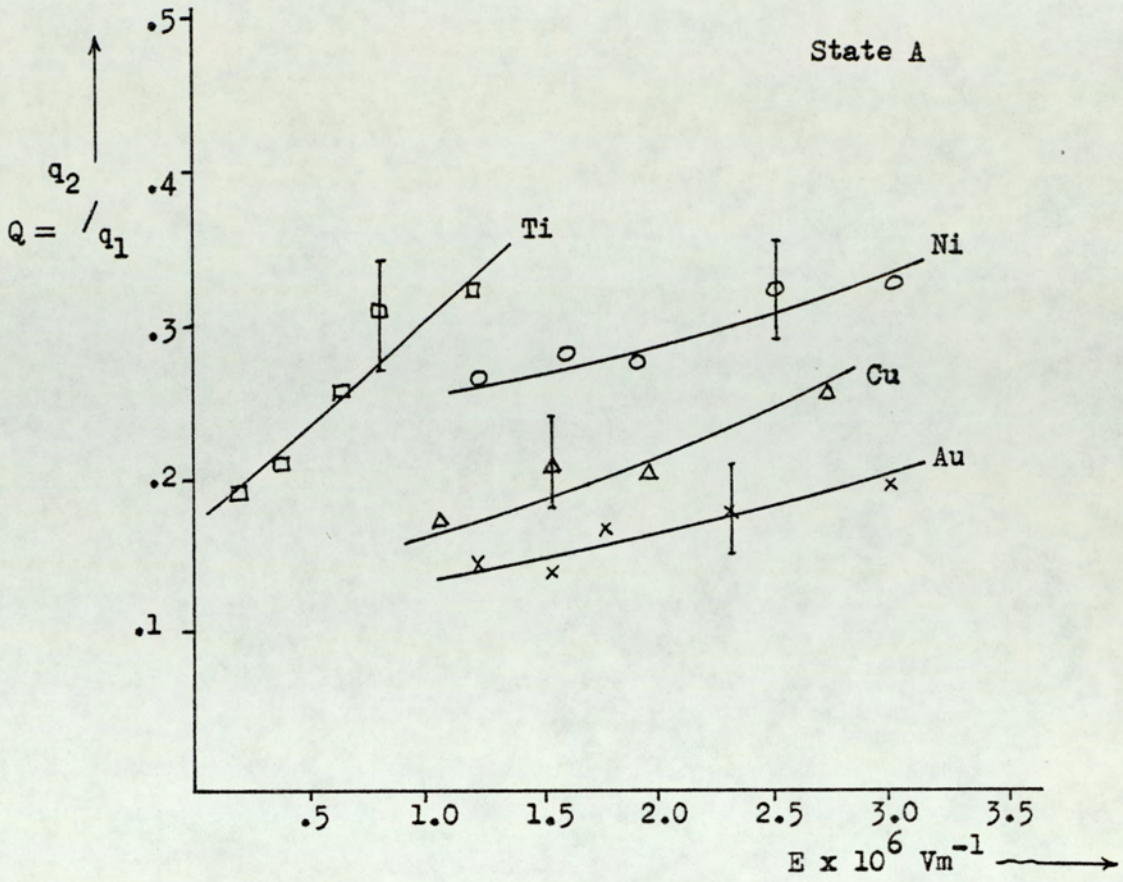

Figure 4.12a

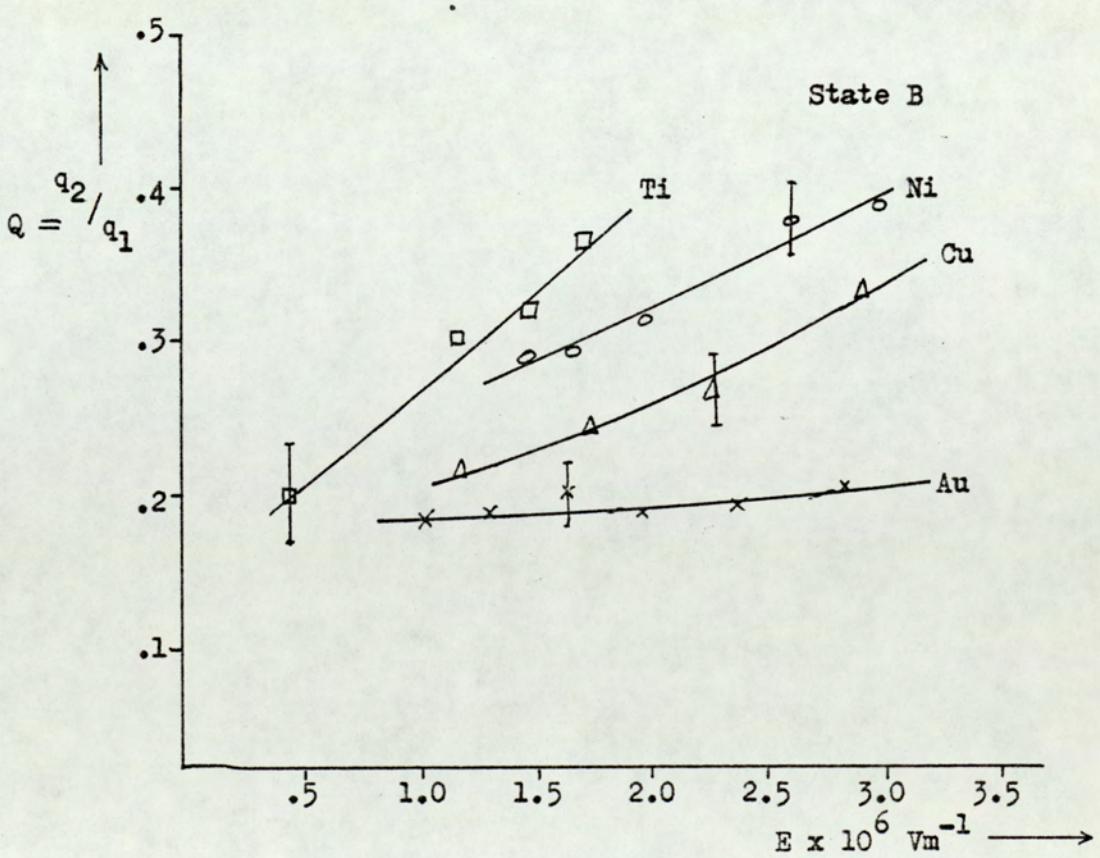

Figure 4.12b

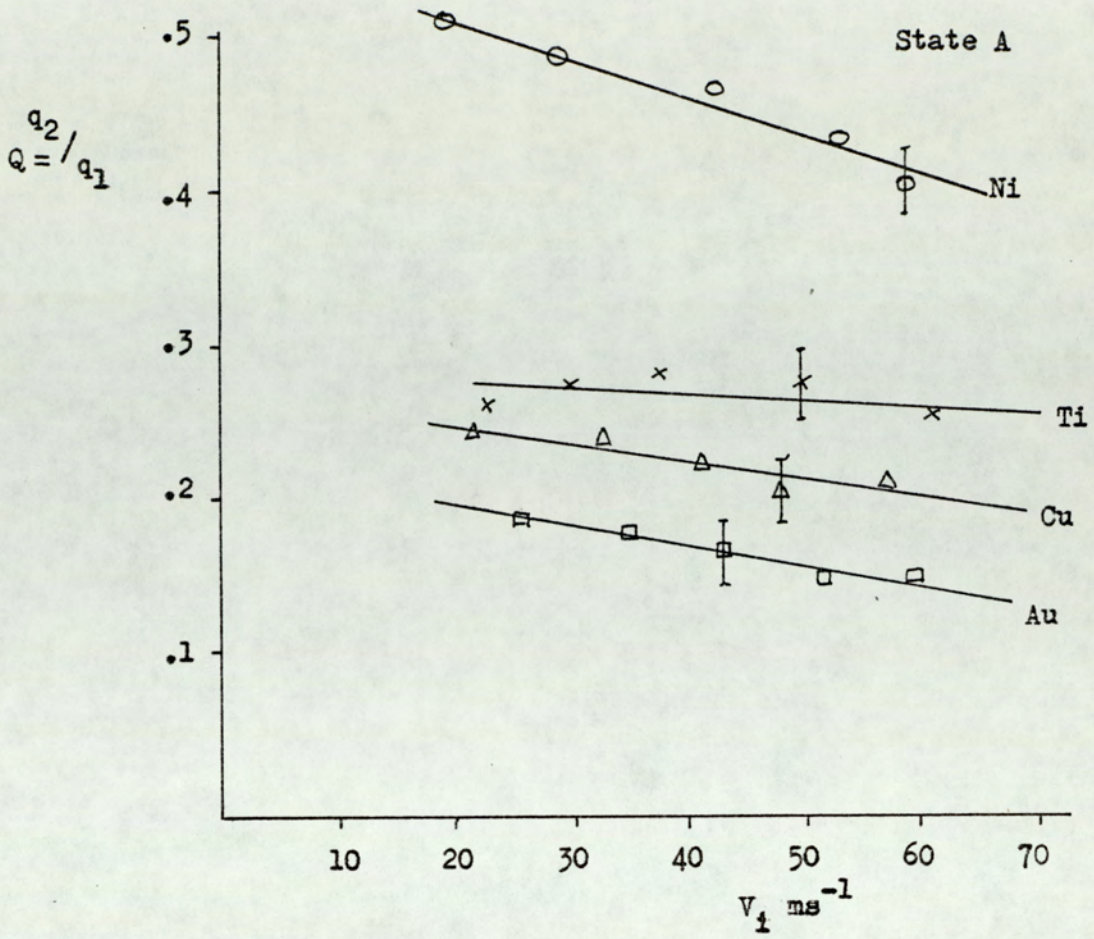

Figure 4.13a

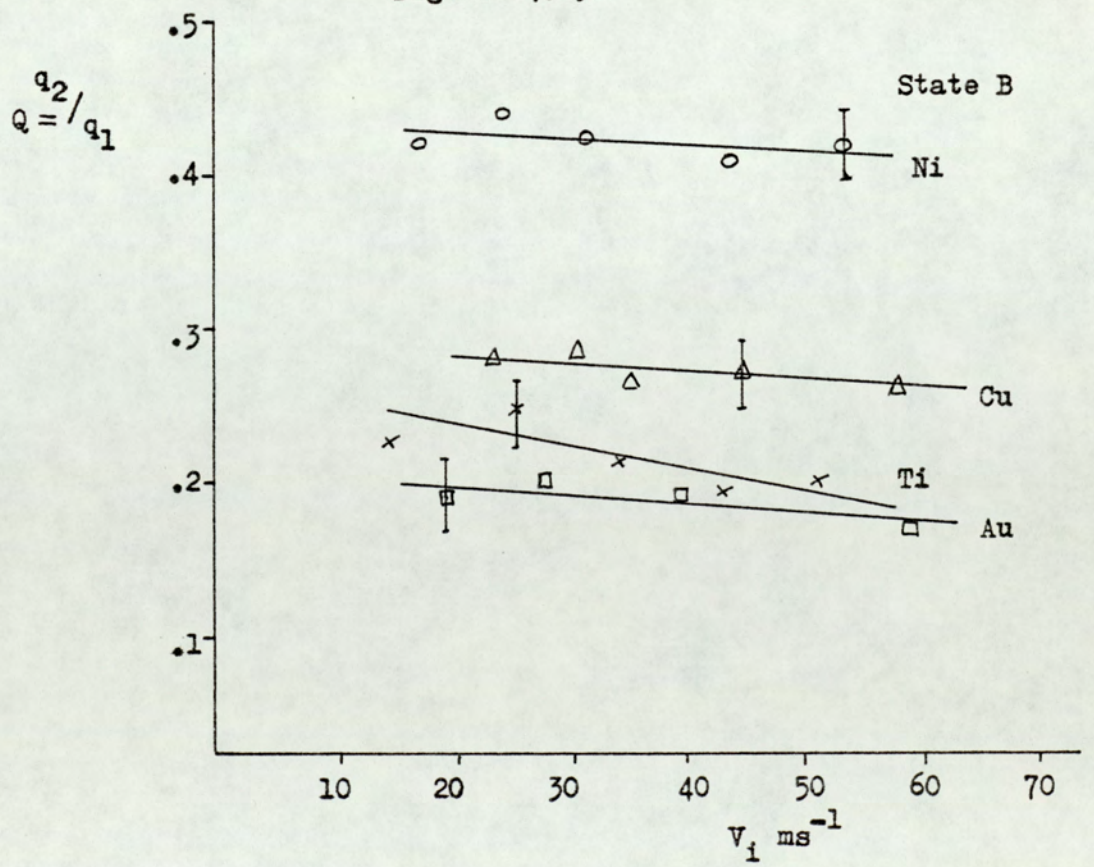

Figure 4.13b

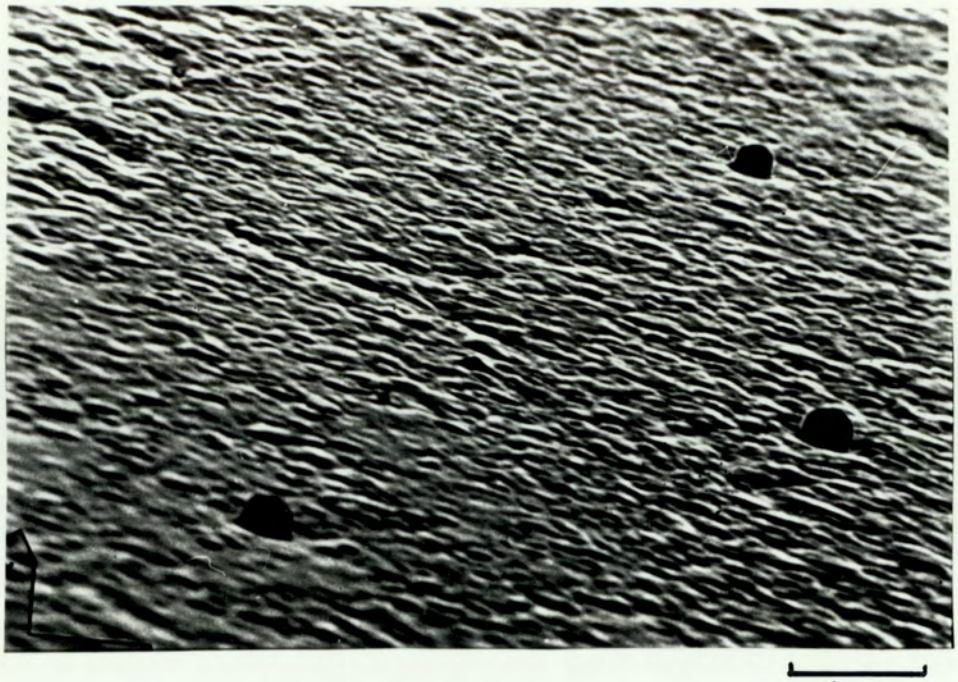

Figure 4.14 : Gold microspheres on an evaporated gold surface

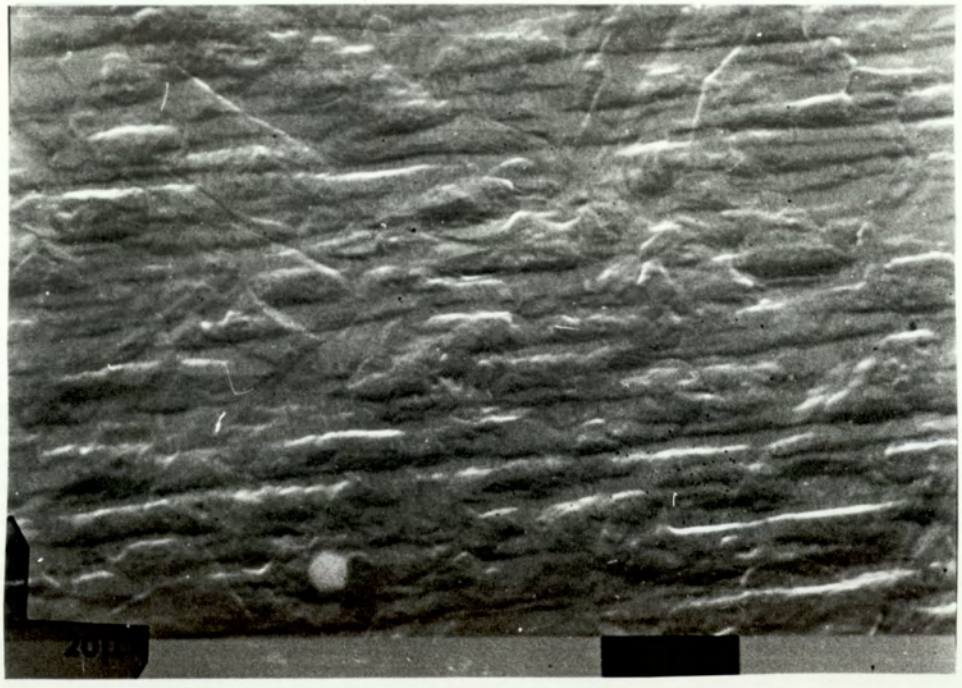

Figure 4.15 : Typical microtopography of a mechanically polished Titanium surface

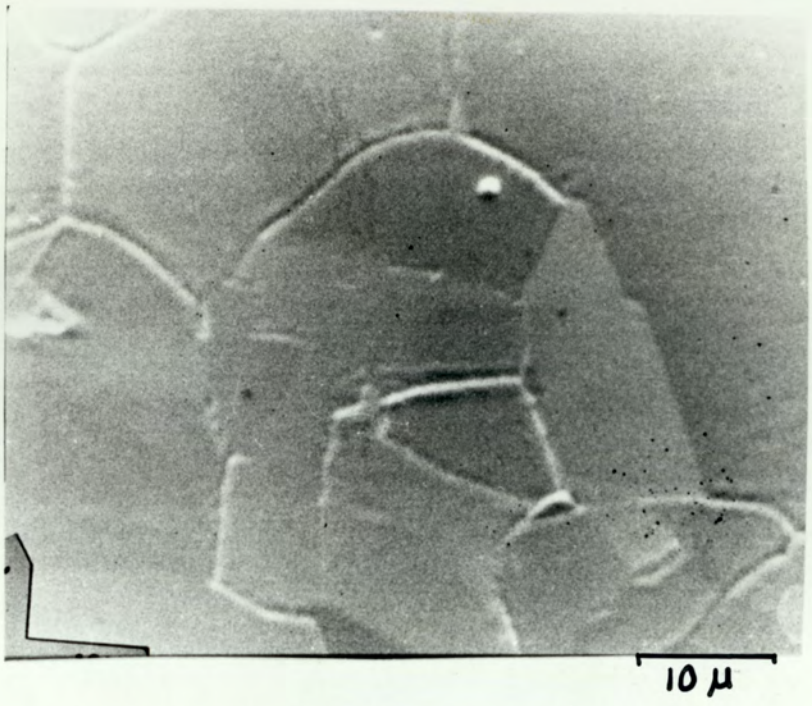

Figure 4.16 : Nickel surface characterised by grain boundaries

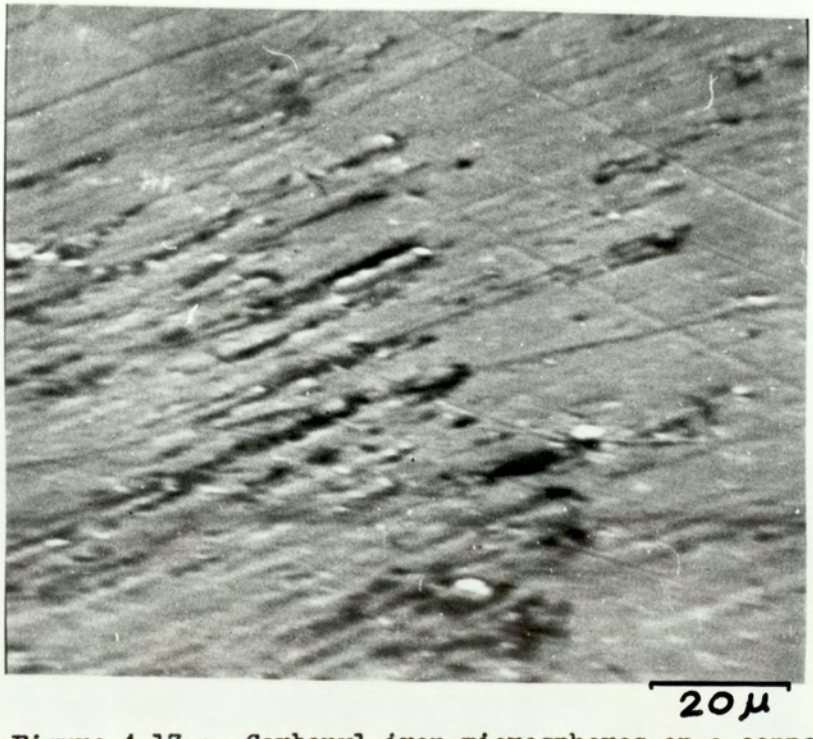

Figure 4.17 : Carbonyl iron microspheres on a copper target

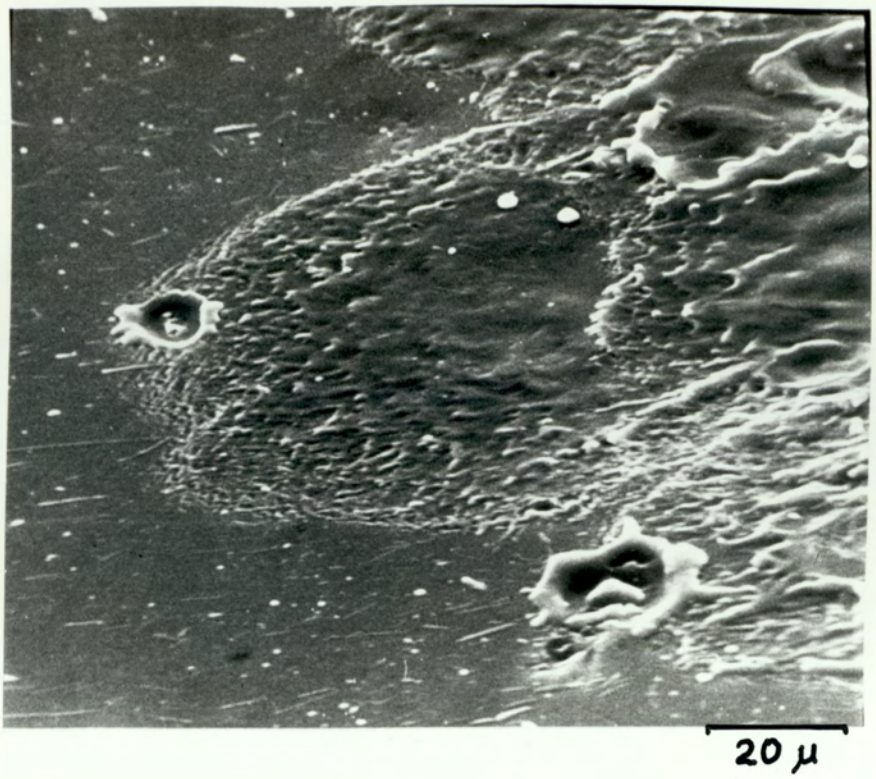

Figure 4.18 : Damage to an electrode surface following electrical breakdown

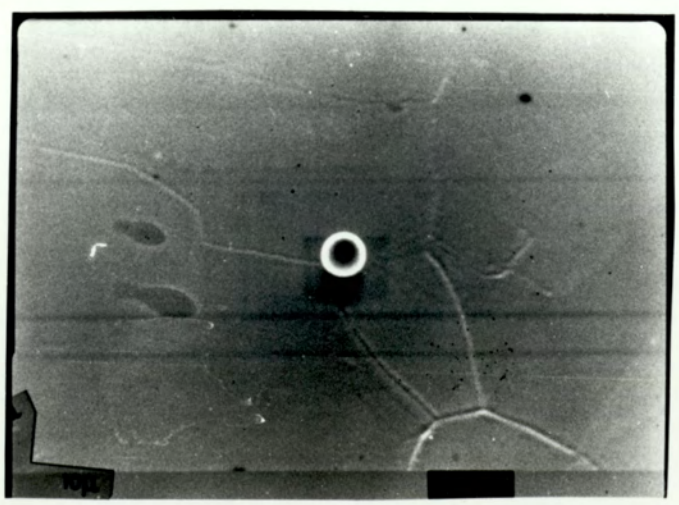

Figure 4.19 : Isolated microsphere on an electrode surface

to 18. Examination of the evaporated gold electrode surface reveals the embedding of the gold microspheres (Figure 4.14). Further analysis of these surface features using Kevex confirms the assumption that the embedded particles are indeed gold and not 'dust'. The typical microtopography of a diamond polished titanium target surface, characterised by a random mesh of scratch grooves and ridges, is illustrated in the micrograph of Figure 4.15. Similar microtopographies were also observed for commercially polished copper and stainless steel electrode surfaces. The nickel surface on the other hand is seen to be characterised by numerous grain boundaries as illustrated in Figure 4.16. Whilst very few microspheres appear to stick to the nickel surface, Figure 4.17 clearly shows microspheres tending to become 'stuck' to the copper surface where they impact directly on a scratch groove. Finally, the micrograph of Figure 4.18 illustrates the extensive damage that is possible to an electrode surface under electrical breakdown conditions.

4.3 Interpretation of ellipsometric data

4.3.1 Titanium alloys

The complementary ellipsometric data relating to the target surfaces of the two titanium alloys, together with the estimated thickness of the oxide films, are presented in tables 4.1 and 4.2. Using the measured values of Ψ and Δ, the optical constants of titanium - which are readily available from existing literature (89, 90, 91): a computer program (see section 3.4) was used to calculate the thickness of the ambient oxide layer present

on the titanium targets. This was found to be of the order of $20 \sim 30^{\circ}$ A which compares favourably with that reported by Menard (89) and Hass and Bradford (92). Numerous other investigations have been carried out on oxides of titanium (90, 93, 94, 95) where it is generally established that the protective crystalline oxide present on titanium forms instantaneously on exposure to air at a thickness of $\sim 10 - 30^{\circ}$ A but then only grows very slowly on further exposure (96). In addition the structure of this oxide film is quite complex and it is generally believed that the air - formed oxide is of the strongly insulating Rutile Titanium dioxide form. However details of the complex titanium oxides will be presented in the discussion. It must also be noted that since film thicknesses and hence optical constants vary with the crystallographic orientation (97, 98) the results obtained above must be interpreted as giving an average value for the thickness of the oxide film. It should be further noted from tables 4.1 and 4.2 that during a cleaning sequence small changes in the ψ value indicates very small changes in the chemical composition and microstructure of a surface whilst the larger changes in $\triangle$ indicate the removal of the oxide film.

4.3 Ellipsometric data

Ti 318 target

	Target surface Treatment	System Pressure (mbar)	Ψ (degrees)	Δ (degrees)	Film thickness ^{o}A
1.	Commercially polished i.e. ambient oxide layer present	2×10^{-9}	31.42	128.60	26
2.	Argon ion bombarded for 30 mins. ion current $\sim 50\mu$A at 4.7 KV	4×10^{-6}	31.98	129.82	18
3.	Further ion bombarded for 45 mins. ion current $\sim 50\mu$A at 4.7 KV	4×10^{-6}	32.02	133.04	2
4.	Commercially polished	3×10^{-9}	33.41	132.2	32
5.	Electron bombarded for 5 mins. beam current$\sim$15mA at 2.5 KV	2×10^{-7}	33.59	136.4	12
6.	Electron bombardment for further 5 mins. beam current$\sim$15mA at 2.5 KV	2×10^{-7}	33.6	138.2	3

Ti 115 target

	Target surface Treatment	System Pressure (mbar)	Ψ (degrees)	Δ (degrees)	Film thickness ^{o}A
1.	Commercially polished i.e. presence of an ambient oxide layer	4×10^{-9}	31.4	128.6	25
2.	Argon ion bombarded for 30 mins. ion current 42μA at 4 KV	10^{-6}	31.52	129.82	18
3.	Further ion bombarded for 50 mins. ion current $\sim$ 45μA at 4.0 KV	10^{-6}	31.55	133.12	2
4.	Commercially polished	4×10^{-9}	33.62	131.20	34
5.	Electron bombarded for 10 mins. beam current $\sim$ 15mA at 2.5 KV	4×10^{-7}	33.81	135.52	13
6.	Further electron bombarded for 5 mins. beam current $\sim$ 15mA at 2.5 KV	4×10^{-7}	33.83	137.01	3

4.3.2 Copper, stainless steel, nickel and gold targets

Detailed independent ellipsometric studies on the target materials listed above were not carried out in the present investigation, mainly due to the time limitation. However, such studies can be found elsewhere (43, 95, 99) where the structure, thickness and optical constants of the air formed oxides corresponding to the present experimental conditions are clearly detailed.

CHAPTER 5

5.0 Discussion of experimental findings

The principal aim of the following analysis is to draw upon the fundamental theoretical concepts discussed in Chapter 2 to provide a plausible interpretation of the experimental findings detailed in the last chapter. A further objective is to assess how the results of these simulation studies might provide an insight into how naturally occurring microparticles behave in a real high voltage gap. For both purposes, the previous format will be followed of treating the mechanical and electrical aspects of particle impact behaviour independently.

5.1 Mechanical interpretation

From the experimental findings presented in Figures 4.2 - 4.4 in the preceding Chapter, it can first be noted that the mean mechanical impact behaviour as designated by the e - values of carbonyl iron and gold microspheres on a range of target materials prepared with various surface states, exhibit general trends which are in broad agreement with previous observations on equivalent macroscopic systems (47, 50, 100). However, there are two important differences:

i) the critical velocity (v_c) heralding the onset of inelastic deformation is > 200 ms^{-1} for micron sized particles compared with 10 cms^{-1} for centimetre - size metal spheres (101) and

ii) for all cases the present microscopic results are characterised by a very large scatter that can reach as much as 50% at the higher impact velocities.

To obtain a plausible explanation for these differences between the macro and micro behaviour, it is necessary to enquire more closely into the detailed nature of the microscopic properties of typical electrode surfaces. Accordingly, a number of effects that could contribute to the observed behaviour will now be reviewed.

5.1.1 Non - planar target surface

It is well known that the mechanical polishing of a material results in a very severely deformed zone near the surface. This zone, commonly referred to as a 'Beilby layer' (102) is highly inhomogeneous and is characterised by a random array of grooves having typical dimensions of say ~ 0.1 micron for $\frac{1}{4}$ micron diamond polished surface, and other irregular features (such as undulations) of somewhat larger dimensions. It could therefore be anticipated that for a field free target surface, a significant number of wide - angle ($>15^{o}$) particle bouncing events would be observed. However, even with the strong collimating effect of the high axial electrical field associated with the present target assembly, it is possible for some reflected particles to acquire off - axis velocity components which would significantly influence the measured values of the rebound velocity v and hence e.

It can be seen from Figure 3.20 (Section 3.1.1) that the collimating aperture in front of the particle detecting drift tube will only transmit paraxial microparticles that will subsequently

undergo impact events which are within a localized region at the centre of the target. However as a result of non - normal impact from the undulations it is possible for the 'reflected' particles to have non - axial trajectories. Such trajectories would therefore be common for the electropolished surface of State D (Figure 4.2) where the effect of such a treatment is known to produce numerous undulations (88). It has been found (44) that the finite aperture of the detecting tube will only accept reflected particles which have an off - axis divergence,

$$\tan^{-1} \frac{D}{2(L+\ell+d)} \leq 11^{\circ} \qquad \text{--- 5.1}$$

where D, L, l and d have all been previously defined in Section 3.1.3. This therefore implies that the measured 'axial' values of the rebound velocity could be liable to an error $(1 - \cos 11^{\circ})v_2$ with a corresponding error in e of approximately 2%. It should also be noted that, in addition to the above considerations, gravity would have a considerable effect on the trajectories of these microspheres. For instance, as a result of gravitational forces the sphere would be deflected in a downward direction (as illustrated below) so that it would again have a non normal impact with the target surface.

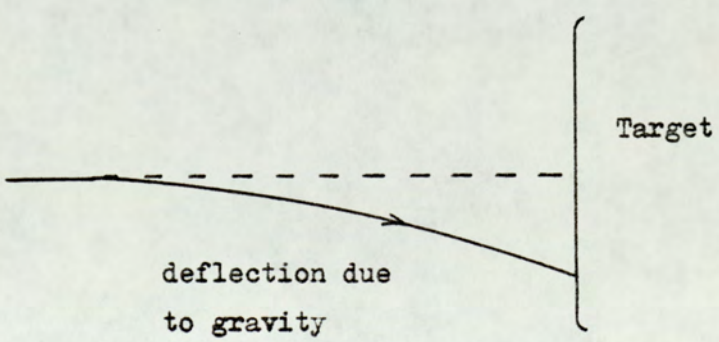

Gravity correcting plates or a vertical system of particle detection would therefore be more appropriate.

Apart from the possibility of oblique reflection from a non - planar microfeature, the microtopography of a target surface may also give rise to impact events where the microparticle makes simultaneous multipoint contact. Thus, as illustrated in Figure 5.1a it may strike the target surface in such a way that there is direct impact on a steep - sided polishing groove, thereby giving rise to a greatly enhanced contact pressure and likelihood of plastic deformation. Accordingly, such an impact would

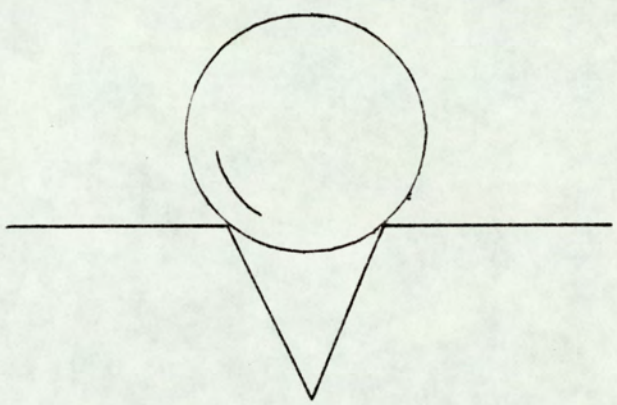

Figure 5.1a

be characterized by a reduction in e of up to $\sim 60\%$ (99). On the other hand, when the impact is such that the microsphere is in the 'valley' between two surface protrusions (Figure 5.1b) an equipartition of impact momentum can be assumed, so that since θ varies from 0 to 45° the measured e' values will vary from e to $e/\sqrt{2}$. A similar result would also be observed if the microparticle was to have an impact with a hole or void present

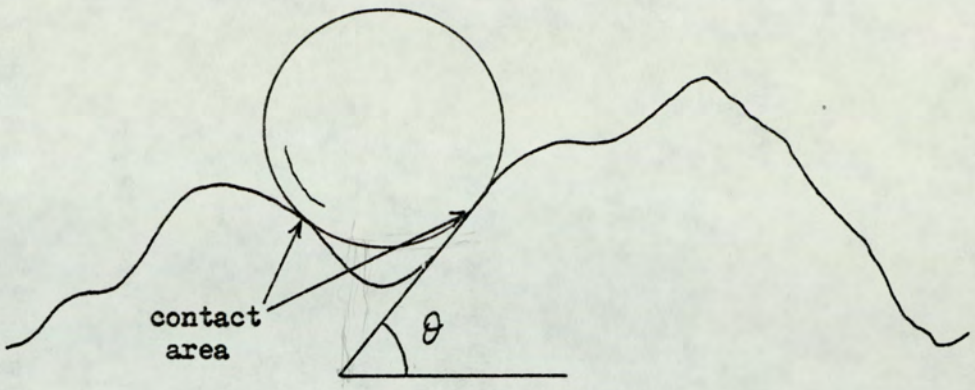

Figure 5.1b

in the microstructure of the target electrode. In addition, since the presence of a grain boundary is a weakness or a strained region in the metal structure it follows that if the microparticle was to impact with an energy sufficient to cause a 'tear' in the grain boundary, energy would be dissipated. As a result the rebound velocity would have a much lower value thus leading to a lower e - value. This effect is clearly illustrated in Figure 4.2 for the argon ion - etched surface of State B, where it is known that such treatment leads to the formation of holes and grain boundaries (105). The low e - values for the nickel target, as illustrated in Figure 4.4 can again be explained by such an effect since it is evident from the micrograph of Figure 4.16 that the nickel surface is characterised by numerous grain boundaries.

5.1.2 Microscopic inhomogeneities

It is clear that in addition to the superficial surface grooves, intensive polishing of a metal surface will profoundly affect the mechanical properties of the surface. It has been shown (47,103, 104)

that in the case of diamond polished surfaces, changes of structure are detectable to depths of many microns. In, addition it is known that such a polished surface will exhibit a variety of micro - regions with differing hardnesses and is therefore likely to produce a large scatter in the coefficient of restitution measurement. These include micro - regions which are

i) work hardened
ii) have undergone changes due to thermal processes during the polishing treatment
iii) consist of a fudge of metal, metal oxide and in some cases the impurities of the polishing medium, and
iv) consist of holes, dislocations and grain boundaries.

The impact behaviour of microparticles with such surfaces would therefore be much more complex compared with the impact on 'dislocation free single crystals'.

The scatter in the measured e values as a result of impact with such micro inhomogeneities for the mechanically polished State A has also been observed for the argon ion etched surface of State B (Figure 4.2). This is not unexpected since it is a clearly established fact that the bombardment of surfaces by ions can also lead to extensive defects such as dislocation loops, voids and stacking faults (105). As the surface is eroded, these defects are in time exposed and act as nuclei for the growth of larger - scale surface structures. In addition, small impurities in the surface can give rise to regions having a much lower sputtering coefficient than the bulk material, which leads to

non - uniform etching of the surface. It has also been shown that ion bombardment can lead to cone formation and also leave further impurities in the form of argon ions in the surface (106). All these effects would therefore account for the large scatter in the measured e values.

5.1.3 Target hardness and density

The linear dependence of e of the target hardness as illustrated in Figure 4.5 can be explained qualitatively using the macroscopic analogy of the Shore (107) solarscope dynamic method. Here the hardness measurement is made by recording the rebound height of a standard sphere after falling through a fixed vertical distance on to a plane anvil of the material. Since the changes in potential energy are related to the kinetic energy, the changes in velocity of impact and reflection and hence e must also be interrelated. A hard material will therefore result in less deformation of the target and a greater recovery of energy from the elastic impact stresses, which is observed as a high rebound velocity and hence a high coefficient of restitution. This is in agreement with the findings of present investigation where as illustrated in Figure 4.5, the softer materials such as gold, copper and nickel yield lower e values than the much harder titanium.

The variation of e with density as illustrated in Figure 4.6 is more difficult to quantify. In a study by Maurer and Rhinehart (108), where large diameter, high velocity (> 9 Kms^{-1}) spherical steel projectiles were fired into sandstone and granite, an

expression for the instantaneous force F per unit projected area i.e. area of impact, was derived by the authors, to equal

$$F = k_2 \rho_t c v_o \qquad \text{- - - 5.2}$$

Here k_2 is a shape factor equal to approximately 0.3 for spherical particles, ρt is the density of the target material, v_i is the velocity of the incident particle. In using this expression to explain the results of Figure 4.6 it can be seen that for a high density material F will be large. Hence a greater deformation and loss of energy will result leading to a lower rebound velocity and thus a lower e value. Maurer and Rhinehart have also provided an expression for the penetration P_n (see Figure 5.2) of a spherical projectile into the target material given by

$$P_n = \frac{1}{\rho_t c k_2} \cdot \frac{M}{A} (v_o - v_c) \qquad \text{- - - 5.3}$$

where $\frac{1}{\rho_t c k_2}$ is a constant characteristic of the target material and involves the elastic constant, M is the mass of the particle, A is the area and v_c is the critical impact velocity at which penetration would rest.

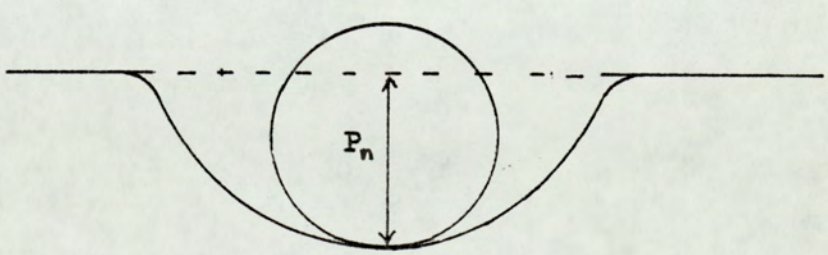

Figure 5.2 : Spherical projectile penetration

Again it can be seen that the higher the density ρ_t the greater the penetration and loss of energy resulting in lower e values.

Dietzel et al. (36) discuss the impact behaviour of similar microparticles in terms of a characteristic product $B\rho$ where B is a shock parameter and ρ is the density of the target material. This product is related to the fraction of the incident kinetic energy of the microparticle which is irreversibly converted to and lost as heat during an impact. Thus, as the density of the target material and B the shock parameter get larger more energy is lost due to the heating effect and less energy is available for rebound. This therefore results in a lower value of the coefficient of restitution. More recently, Smith and Adams (39) have discussed the dissipation of the kinetic energy of the particle on impact in terms of the shock waves that are generated at the point of contact between the microparticle and target respectively. The velocity of these shock waves is dependent on

i) the instantaneous angle of contact θ between the surfaces at the edges of the disc of contact and

ii) the physical properties of the microparticle and target materials.

Since for small values of θ , the velocity of the contact points is greater than the velocity of either of the shock waves, the latter will remain attached to the contact points so that no shocked and thus high - energy material is exposed to the surface. No ejection of liquid, vapour or plasma from either the particle

or the target is therefore possible. However, as the particle penetrates the target, the angle θ increases until a critical angle is reached whereby the process is reversed, i.e. velocity of one of the shock waves becomes greater than that of the contact points. Under such conditions, the shock wave becomes detached from the contact points and highly shocked, so that it is possible for high - energy material to become exposed to the surface resulting in the ejection of vaporized and ionized materials. The question of whether the particle or the target material is ejected is dependent on the physical properties of the two impacting materials. It must be noted however, that these effects were observed by the authors and several other researchers only when velocities in excess of ~ 5 Kms^{-1} were used. This would therefore imply, that in the present low velocity investigation, a dissipation of energy in the manner suggested above would not be applicable.

5.1.4 Impact velocity

Figure 4.2 and 4.3 show a common non - linear variation of e with the impact velocity v_i for the various target materials investigated. By the nature of the particle source, it should be noted that the impact velocity is in turn dependent on the particle size as illustrated in Figure 4.7. This dependence of e on v_i is similar to results reported by Latham et al. (44) where again considerable scatter was found in the coefficient of restitution values. This is unlike the results found by Hutchings (51) who, when investigating the impact of millimetre sized steel particles onto steel targets (i.e. a macroscopic study) reported the gradual decrease of e with a corresponding

increase in v_i from 50 to 90 ms^{-1}. Tabor (46) considers the impact of a sphere of velocity v_i on to the surface of an anvil so that the yield pressure P essentially remains constant. A value v_2 for the rebound velocity can then be obtained from the following relation

$$v_2 = k(v_i^2 - 3/8\ v_2^2)^{3/8} \qquad \text{- - - 5.4}$$

This relation clearly shows the v_2 is no longer proportional to r but dependent on v_i. The ratio $e = v_2/v_i$ will now not be constant. A gradual decrease in e with increasing impact velocity was confirmed by Tabor by experiment. Several other studies (50,100) have been carried out on the macroscopic scale to show the impact behaviour of macrospheres on planar targets. One significant difference between the microscopic and macroscopic studies however, is the variation in the range of impact velocities for which surface deformation is elastic. From scanning-electron-microscopy studies of the permanent target indentations resulting from the impact of high - velocity microparticles, Dietzel et al. (36) have established that the critical velocity v_c heralding the onset of permanent elastic deformation is $\geqslant 500$ ms^{-1} compared with 0.1 ms^{-1} for centimetre sized particles. Using an entirely different approach of the hydrodynamic theory, for the impact pressures of fluid jets to the situation of a continuous stream of spherical particles, Cook has obtained an expression for the critical velocity v_c given by

$$v_c = 2.7\ (\frac{\sigma}{\rho})^{\frac{1}{2}} \qquad \text{- - - 5.5}$$

where σ is the yield strength of the colliding material.

This expression predicts values of $v_c \simeq 1$ Kms^{-1} for titanium and nickel. From these results it would appear that in the case of the micro - system where a microsphere impacts on a plane metal electrode, the impact will be purely elastic and any severe deformation is unlikely for any combination of colliding materials used in this investigation. This is in agreement with the supplementary micrograph evidence of Figures 4.14 - 4.17 which illustrate a distinct lack of impact craters as long as breakdown has not been initiated.

Following an alternative approach, Tabor (46) has considered the average pressure Pe developed between a spherical indenter and an anvil in a purely elastic collision and assuming a value of 0.3 for Poisson's ratio found Pe to equal

$$Pe = \frac{1}{26.6r^3} \frac{mgh_1}{(1/E_1 + 1/E_2)^4} \qquad - - - 5.6$$

where mgh_1 is the potential energy of the indenter when dropped from a height h_1. This is equivalent to the kinetic energy of the sphere when impacting with the electrode. Thus if h_1 is 1 m and the indenter is a steel ball of mass 4×10^{-3} Kg, diameter 1 cm and $E_1 \simeq E_2 \simeq 10^{10}$ Pa a value of $Pe \simeq 1.2 \times 10^{10}$ Nm^{-2} is obtained for nickel. The critical pressure Pc at which plastic deformation will occur is obtained from equation 2.2 provided the critical velocity v_c is known. Hence by substituting in values for v_c from above it is seen that for nickel this equation yields a corresponding value of $Pc \simeq 7.8 \times 10^{10}$ Nm^{-2}. Since $Pc > Pe$ it is clear that the impact velocity is not critical.

5.1.5 Surface films and mechanical strength

When in a practical situation, a particle impacts on to a surface covered by a surface film, frequently in the form of an ambient oxide layer, it may undergo severe deformation over the regions of contact. Thus the influence of such films on particle impact behaviour is clearly relevant and needs to be considered. If the film is ductile, it will deform with the metal and retain its integrity, thus preventing intimate metal - metal contact. If it is brittle, it will crack and the metal will tend to flow through the cracks themselves (109). However, even though a film may undergo plastic deformation, it is found that very high strengths (i.e. yield stresses) are obtained in these thin films with values up to 200 times as large as those found in the corresponding bulk material (110). This strength appears to arise in part from the restraint which the film surface exerts on the motion of the large number of grown - in dislocations. It is also well known that the mechanical strength of most polycrystalline solids, when measured on a bulk scale, is very much smaller than the theoretical strength of a perfect crystal. This is due to the presence of defects within the crystal and on its surface. It is these defects in the form of dislocations and cracks which form the basis of the bulk mechanical behaviour of solids, for example, in the case of ductile metals the bulk strength is primarily determined by the generation and propagation of dislocations. Since these dislocations have a spacing which may be considerably larger than the atomic dimensions(e.g. about 5000 atomic spacings apart in an annealed metal), the strength properties might be expected to depend on the scale of the

experiment. Experimental verification that strengths approaching the theoretical value can be achieved in nearly perfect crystals has come with the discovery of the high strength of metal whiskers. This is in agreement with previous studies on the mechanical strengths of metals on a small scale which all show increasing strength with decreasing size. Studies in the form of sub - micrometre indentations have been carried out by Gane (111) to investigate the strength properties of annealed metals. His results showed that although strengths similar to theoretical values could be achieved, the strength was strongly dependent on the condition of the interface when stress was applied at an external surface. Gane has also shown in the same study that surface films can have a profound effect on the mechanical strength. Absence of surface films have produced large stress concentrations at the interface and a high strength is no longer observed. Finally since surface oxide films are generally known to have higher mechanical strengths than the bare substrate (see earlier) it is not surprising to find that the presence of surface oxide films can substantially increase the surface hardness. This is clearly illustrated in Figures 4.2 and 4.3 where it can be seen that the coefficient of restitution is significantly lowered with the removal of the contaminating film.

5.1.6 Temperature variation with impact: Impact heating

As mentioned previously, it is clear that even for low velocity impacts, a portion of the available kinetic energy will be dissipated as heat. Hence, depending on the magnitude and rate of

release of the available kinetic energy, and the thermal properties of the microsphere and anvil, there could be a situation where high temperatures are generated at the contact surface. If the heating were to be concentrated to a small volume of the material it could result in localised melting. In addition, it is fair to assume that this transient temperature is a function of the impact velocity and many studies have been carried out to investigate this relation. Smith and Adams (10) have determined temperatures of the order of 2000 to 4000 K for particles with velocities in the range 2 to 4 Kms^{-1}. This is in broad agreement with the findings of Hansen (112), who, from his experimental data, obtained temperatures varying from about 3000 to 20,000 K for particle velocities varying from several kilometres per second to 40 Kms^{-1}. At low velocity impacts, however, it has been found (113) that during normal impact of spheres the temperature rise is only a few degrees whilst for the case of a sphere impinging on a sharp spike the increase in temperature is $\sim$ 5 - 10° C. More recently Chakerabarti (114), investigating the impact of microspheres on rigid inclined planes for both elastic and semi- elastic low velocity impacts, has calculated the temperature rise for a 100 ms^{-1}, 100 micron sphere impacting at an angle of 45° to below 250° C. Under identical conditions for a much smaller sized sphere this was found to decrease to below 100° C. In addition, he found a further decrease with increasing values of e and decreasing values of the incident velocities. It can therefore be assumed that in the present investigation where much smaller, low velocity particles have been used, the contribution due to temperature rise is unlikely to play a significant rôle in the energy enhancing and subsequent electrical breakdown processes.

5.2. Electrical responses

The experimental findings presented in Figures 4.9 to 4.13 indicate that the mean electrical impact behaviour as designated by the ratio q_2/q_1 (i.e. the Q value) exhibits general trends which are similar for all particle/target combinations. Thus referring to Figures 4.9, 4.11 and 4.12 it can be seen that for all cases, q_2/q_1 increases with increasing macroscopic gap field, indicating that the charge reversal efficiency improves with increasing field. This is in contrast, to the variation of Q with impact velocity where, as illustrated in Figures 4.10 and 4.13, the general trend is for charge reversal efficiency to decrease with increasing impact velocity. However, looking at this data more closely, it can be seen that the mean electrical impact behaviour varies considerably for the differing surface states of individual electrode materials. For instance, referring to Figure 4.9 and 4.10 it can be seen that there is a marked lowering in the Q - values for the two titanium alloys when their surfaces have been subjected to particular treatments, suggesting a suppression of the charge exchange mechanism. As illustrated in Figure 4.11, this is in contrast to the behaviour observed with copper and stainless steel where a marked increase in Q - values for the corresponding 'clean' electrodes indicates a promotion of the exchange mechanism. In addition, from the experimental findings of Figure 4.9 and 4.11 it would appear that the commercially polished surface (State A) of titanium is a much more efficient promoter of the exchange mechanism than the similarly polished surfaces of copper and stainless steel. This is an entirely unexpected finding since practical experience has shown titanium

to be the most stable of high voltage electrode materials and presumably therefore the least efficient promoter of the charge exchange mechanism. From the foregoing summary, it is therefore clear that there are a number of conflicting factors inherent in these experimental findings which require clarification and analysis. Accordingly, the aim of the following discussion is to

i) compare the overall experimental trends with theoretical values derived from the model discussed in Section 2; and

ii) modify the theoretical model where necessary by referring to related phenomena cited in literature which might have bearing on the theory.

5.2.1 Comparison of experimental and theoretical Q - values

Figures 5.3 to 5.4, present comparisons of the experimental findings with those calculated from existing theoretical models. Thus Figure 5.3 illustrates the variation of Qr, the magnitude of charge exchanged between the particle and target as obtained from equation 2.35, with the macroscopic gap field E_o for several particle radii and particle/electrode gap separations. Also shown on this figure are the corresponding Qr - values for the experimental results. From an inspection of the theoretical plots a number of factors are clearly apparent:

i) there is 'size effect', where it can be seen that the magnitude of Qr clearly increases with particle size,

ii) there is a marked increase in the gradient of the slope, particularly at larger gap separations and particle radii,

iii) Qr - values fall off rapidly with a thicker oxide film and,

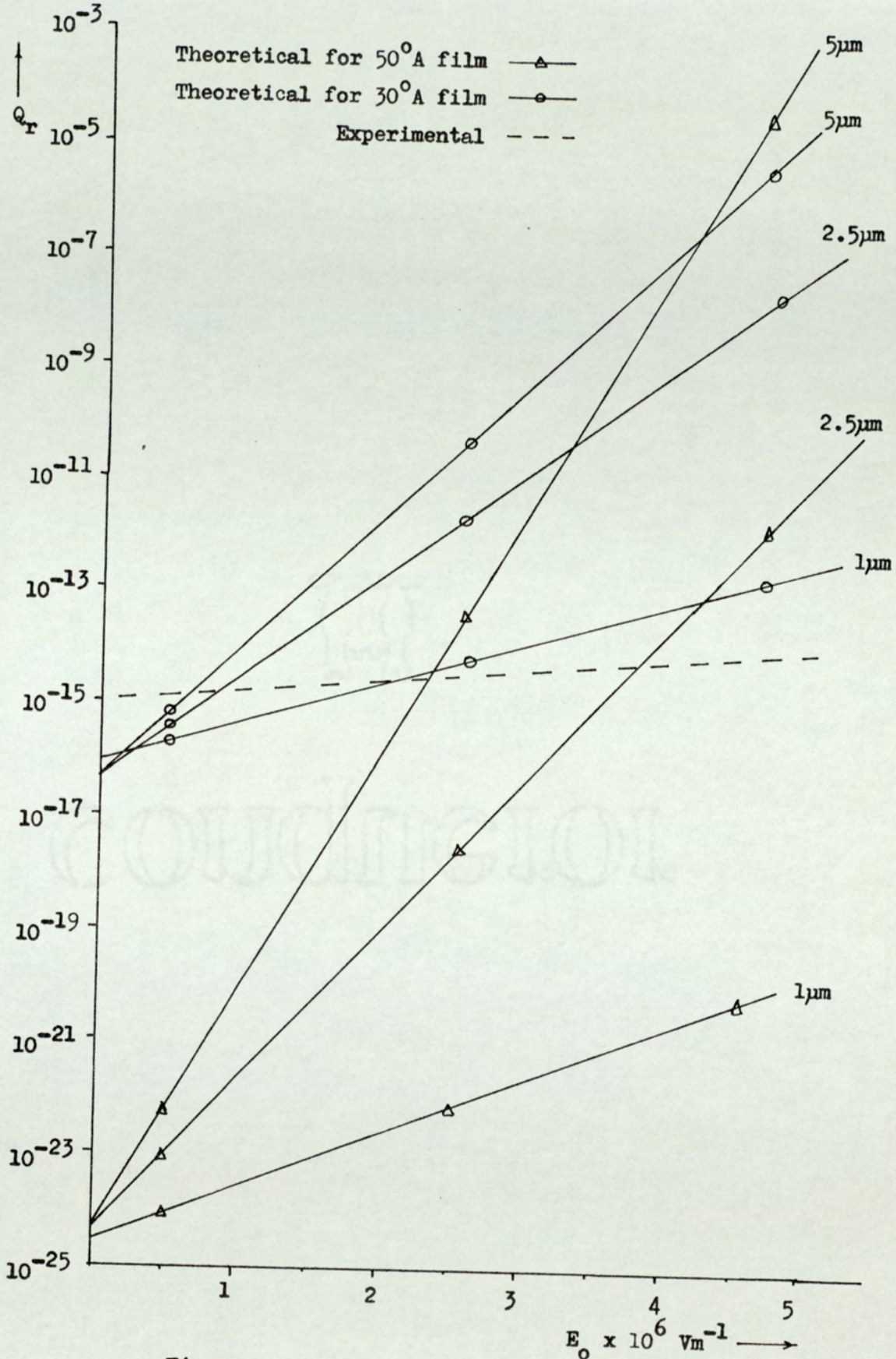
Theoretical for 50°A film
Theoretical for 30°A film
Experimental
Q_r
10^{-3}
10^{-5}
10^{-7}
10^{-9}
10^{-11}
10^{-13}
10^{-15}
10^{-17}
10^{-19}
10^{-21}
10^{-23}
10^{-25}
5μm
5μm
2.5μm
2.5μm
1μm
1μm
1
2
3
4
5
$E_o \times 10^6$ Vm^{-1}

Figure 5.3

iv) there is a marked discrepancy between the theoretical and experimental plots.

In order to explain these factors it is first necessary to look more closely at the derivation of the expression for Qr, viz.

$Qr = \pi a^2 t_c \exp(KV_{op}) / 2\sigma_o K$ From section 2.3 it is clear that V_{op} is a function of the actual field Eg existing across the tunnelling junction and the junction thickness g. Eg is in turn the sum of the two external components E_1 and E_2 which have both been previously defined. However, it is necessary to consider a third component E_3 (115) which is derived from the internal bias arising from any differences in the substrate work functions ϕ_p and ϕ_T. (See Section 2.2 equation 2.17). The effect of this intrinsic field is, as discussed in Section 2.2, twofold; i.e. it can either augment or reduce the gap field. Accordingly, the effect on Eg will be such that three types of tunnelling regime may now be considered:

i) $Eg = E_1 + E_2$, corresponding to $\phi_p = \phi_T$ so that $E_3 = 0$

ii) $Eg = E_1 + E_2 + E_3$, corresponding to $\phi_p > \phi_T$ so that the junction is 'forward - biased'

iii) $Eg = (E_1 + E_2) - E_3$, corresponding to $\phi_p < \phi_T$ so that the junction is 'reverse - biased'.

This would therefore result in expression 2.35 becoming

$$Qr = \frac{\pi a^2 t_c}{2\sigma_o K} \exp \underbrace{Kg\left[\frac{Q_p}{\bar{\varepsilon} C_o(g) g} + 2{\cdot}6\left(\frac{R_p}{g}\right)^{{\cdot}8} E \pm \frac{\Delta\phi}{eg}\right]}_{V_{op}} \quad ---5.6$$

which in logarithmic form will be

$$\log Qr = \log \frac{\pi a^2 t_c}{2\sigma_o K} + Kg\left[\frac{Q_p}{\bar{\varepsilon} C_o(g) g} + 2{\cdot}6\left(\frac{R_p}{g}\right)^{{\cdot}8} E \pm \frac{\Delta\phi}{eg}\right] \quad ---5.7$$

This expression would therefore indicate that the slope of Figure 5.3 is controlled by the parameters K, g and R_p where K also controls the intercept of the slope. It must be noted here that the experimental slope has a value which is > 0 and < 1. At first sight it would appear from the published data of Simmons (69) that since at low bias voltages (i.e. <1.0 volts) the tunnelling resistivity σ stays constant, so that $\sigma \simeq \sigma_o$, and K can be assumed to be negligible: with this assumption it is possible to obtain an almost perfect match between the theoretical and experimental slopes. However, since the new expressions for Eg yield values for the bias voltages V_p which are greater than 1.0 volts, a constant value for σ cannot realistically be assumed. On the other hand, the linear dependence of σ with V_p assumed by Latham and Brah (43) would appear to be an extreme approximation. Thus looking more closely at the published data of Simmons (69) it can be seen that although the tunnelling resistivity does vary with V_p, the gradient K varies non linearly so that a mean value of the gradient must be used. For example, at a film thickness of 30^{o}A, the mean value $\bar{K}$ would be equal to $\simeq$ 1, and at a thickness of 15^{o}A K $\simeq$ .8. Substituting $\bar{K}$ for K into equation 5.6 and evaluating the corresponding Q_r values for the three tunnelling junctions now yields the curves illustrated in Figure 5.4. Only values for 2.5 μm radius particle have been plotted since it would appear from Figure 4.7 and 4.8 that the majority of particles selected in the present experimental regime, range in diameter from 4 to 6 micron. A discrepancy between the theoretical and experimental

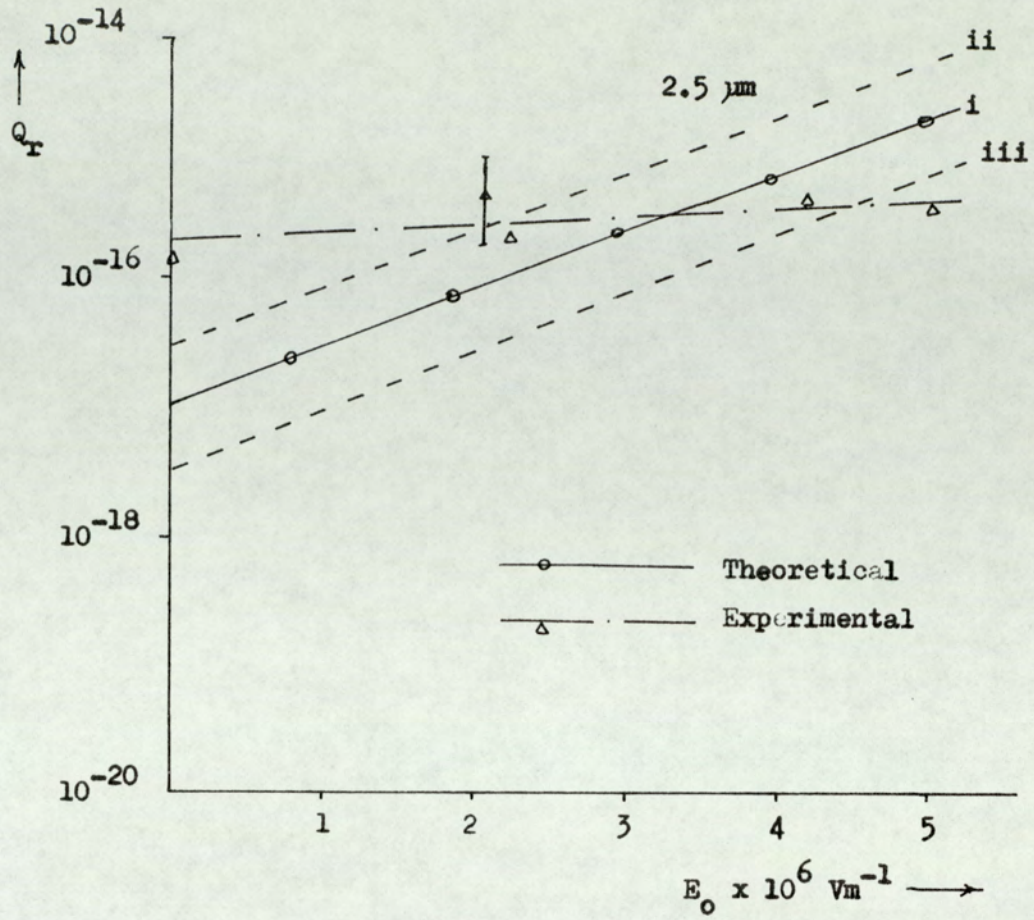

Figure 5.4

results still appears to exist although the slope is much more acceptable. It should be noted here that in practice, the variation of σ with V_p may be much more uniform than that calculated by Simmons. In addition, there is very little evidence to date, to suggest that the experimental variation of σ with V_p is consistent with theoretical approximations; especially at the high bias voltage range.

Figure 5.5 illustrates the theoretical variation of q_2/q_1 with E_o and incorporates the three types of impact events that are possible, and indeed observed experimentally.

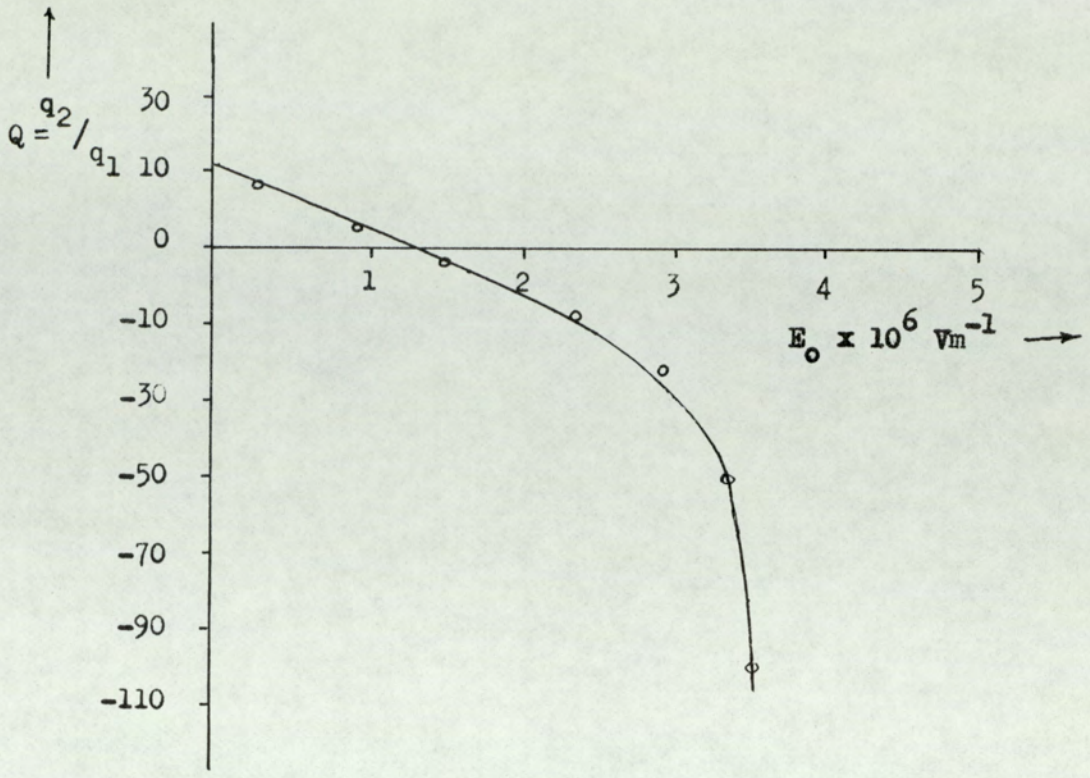

Figure 5.5

In terms of positively charged incident particles such events include

i) A bouncing event where the particle returns with both a reduced positive charge and velocity i.e. as illustrated below.

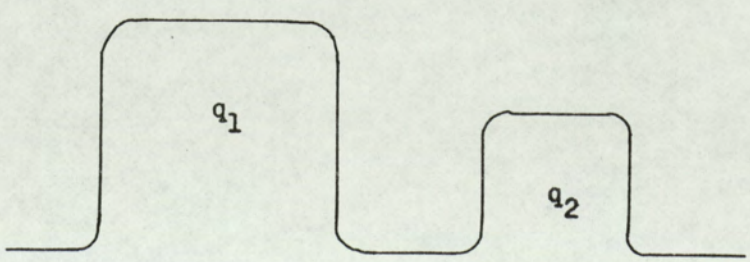

Now since $Q_r = q_1 - q_2$ and $Q = q_2/q_1$ then $Q = (1 - Q_r/q_1)$ and will be positive for $|Q_r| < q_1$

ii) An impact event where there is no 'return' particle i.e. it sticks to the electrode

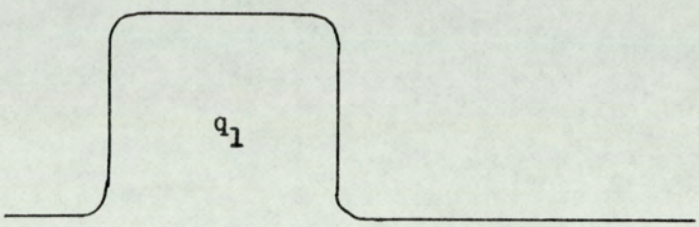

so that $Q_r = q_1$ and $Q = 0$.

iii) A bouncing event where charge reversal occurs so that a particle of opposite charge returns with a negative charge as illustrated.

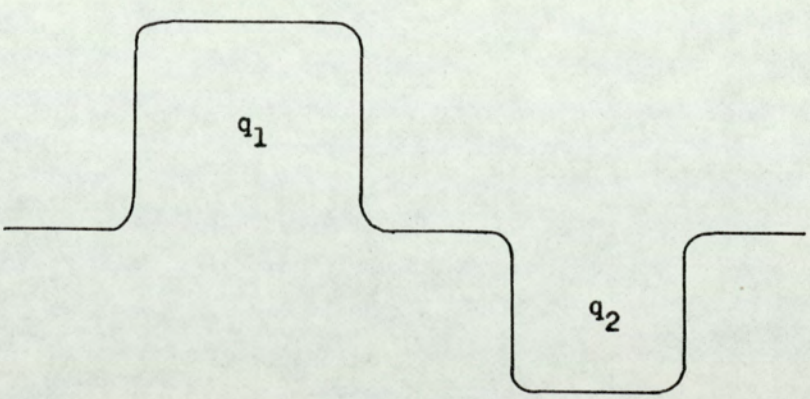

Here again $Q_r = q_1 - q_2$, but because q_2 is negative $|Q_r| = |q_1| + |q_2|$ and $Q = (1 - \frac{Q_r}{q_1})$ will be negative for $|Q_r| > q_1$.

It is therefore seen that theoretical values of q_2/q_1 can vary from + 1 to - 100. It must be noted however that although the experimental values plotted in Figures 4.9 to 4.13 correspond to situation (iii) they appear to differ from the theoretical plots of Figure 5.5. This is because the experimental values represent the modulus and are presented as mirror images.

Referring, again to Figure 5.4, it can be seen that although the slope for the modified expression is much improved, there are still some discrepancies between theoretical and experimental values, both in the slope and the magnitude of charge exchanged. It is clear therefore, that apart from looking in more detail at the various assumptions made in the theoretical model of Section 2, consideration must also be given to the possibility that there may be other important physical mechanism operating during a bouncing event that were not accounted for in the original theory. A qualitative account of a number of some such mechanisms will now be given.

5.3.1 Contact area and contact time

From the foregoing discussion it is clear that the area of contact a and the time of contact t_c, between the microparticle and target has an important influence on the magnitude of charge (Q_r) transferred. Previous values of a, for a one micron particle have been approximated by various authors, to be of the order of $\sim 2 \times 10^{-8}$m. However, this does not appear to be the case in the present experimental regime, where for a 2.5 micron particle (chosen for reasons

mentioned earlier) with a subcritical velocity of $\sim 40 ms^{-1}$ (Figure 4.7), expression 2.9 yields a value of $a = 2 \times 10^{-7} m$. This is an order of magnitude larger than the one used in the previous theory and would therefore correspond to Q_r values which are 100 times larger. Similarly expression 2.8 yields a value of $t_c \simeq 5 \times 10^{-8} s$ for a 2.5 micron particle. Again, this is more than an order of magnitude larger than the previously employed values. From qualitative considerations the use of longer t_c values can be further justified if the effect of adhesive forces as discussed in Section 2.1.3 is considered. Such forces will have the tendency to increase the time of contact between the micro-particle and target. In addition, this will be particularly true for the impact of carbonyl - iron particles with State A titanium targets, since as discussed in Section 2.13, the adhesive forces will be much larger for a non ductile material such as titanium. Thus for the State A targets, the presence of the much stronger surface films (Section 5.1.5) will clearly increase the adhesive forces and thus the contact time. The corresponding effect on the magnitude of Q_r will thus result in larger q_2/q_1 values. This effect is clearly illustrated in Figure 4.9 where the harder surfaces of State A exhibit larger Q values than the 'softer' 'cleaner' surfaces of States B and C.

5.3.2 Electrical properties of surfaces layers

The theoretical considerations clearly indicate that the charge reversal efficiency is strongly dependent on the electrical properties of the various surfaces. To date, all assumptions made in the theoretical model are idealized, e.g. plane homogeneous oxides

with no interband states have been assumed. However, it must be recognized that for the polycrystalline surfaces used in the present study it is possible for there to be large local variations in the oxidation conditions involving both thickness, band gap and interband states, thus indicating that surface properties would ideally need to be defined on a sub - micron scale. Also, the various surface treatments employed in the present study are likely to result in considerably differing surface films and thus electrical properties. For instance, it has been shown that the species of the surface oxide film on titanium can alter with argon ion bombardment (117): viz. a small amount of ion bombardment can lead to the reduction of the normally rutile TiO_2, which is strongly insulating, to TiO with further bombardment resulting in the removal of this TiO. This is due to the composition of the air - formed oxide which varies across its thickness i.e. near the metal interface it consists of TiO and at the surface it is TiO_2 (117). The values of the dielectric constant of the titanium oxide films have been found to vary from 60 - 85 (118, 119), depending on the species of the oxide film. In addition, it has been shown that the presence of surface impurities can alter the dielectric constant by a significant amount (110). The dielectric constants of Fe_2O_3, CuO and stainless steel on the other hand all have considerably lower values (~ 6) (41, 120, 121), although again no detailed information on their exact value with varying oxide species is available. The effect of high dielectric constants would be to increase the magnitude of Q_r, an effect which is again clearly illustrated for the State A surface of titanium in Figure 4.9. For States B and C where if, as assumed, the only film to be considered is that

of the carbonyl - iron particle it can be seen that $\bar{\varepsilon}$, the effective dielectric, whilst remaining relatively uncharged for copper and stainless steel, will be considerably altered for the case of titanium. Thus a much more marked variation in the behaviour of differing states of titanium would be expected. This is again in agreement with the finding of the present study as illustrated in Figures 4.9 and 4.11. It should also be noted here that inhomogeneous oxides are likely to result in variations in the field Eg existing in the film and thus produce large variations in the observed charge reversal values.

5.3.3 Influence of the relative work functions

It is clear from the theoretical considerations of Section 2 that the contribution of the intrinsic field, arising as a result of differing particle/target work functions, will be to either augment or reduce the gap field existing in the tunnelling junction. Thus as expressed in equation 5.6 this contribution will be of particular importance at low external fields or low bias conditions. The mean values of the quoted work functions for the materials studied in their ambient state i.e. equivalent to State A, are:-

$$\phi_{Fe} \sim 4.47, \quad \phi_{Cu} \sim 4.45, \quad \phi_{Ti} \sim 3.95, \quad \phi_{St.St} \sim 4.5,$$

$$\phi_{Au} \sim 5.2, \quad \phi_{Ni} \sim 4.4$$

It therefore follows from Section 5.2.1 that the impact data obtained from copper and stainless steel targets corresponds to tunnelling regime (1). In the case of the State A Ti targets, the tunnelling junction will be 'forward biased' since $\phi_{Fe} > \phi_{Ti}$,

giving rise to an enhanced charge reversal response which is clearly evident in the experimental findings of Figure 4.11. The decrease in the q_2/q_1 ratio for the 'clean' State B and C Ti targets as illustrated in Figure 4.9, which is in sharp contrast to the behaviour of other materials, can be similarly explained by the relative change in the tunnelling regime. For instance, it has been clearly established that the bombardment of Ti by Ar ions increases the work function of titanium (105, 122, 123). A similar effect has also been observed with the electron bombardment of surfaces by several authors (110, 122). Thus, it is clear that although the tunnelling regime may not undergo a complete change from a 'forward' to a 'reverse' biased situation, the charge exchange process will clearly be inhibited. This effect can be assumed to predominate over the enhancement normally expected from the reduction of the oxide thickness. The use of gold microspheres as the impacting particles on titanium results in charge reversal of the particle at much lower fields as illustrated in Figure 4.12. This can again be explained in terms of the intrinsic field contribution due to the difference in work functions, since as mentioned earlier this contribution is particularly important at low external fields. The effect is further enhanced as a result of the 'forward' biased situation ($\phi_{Au} > \phi_{Ti}$). Similarly, the use of gold particles on nickel and copper targets results in 'forward' biased tunnelling regimes whereas the impact with gold targets corresponds to the tunnelling regime (i) since $\phi_p = \phi_T$. Again these effects are clearly illustrated in Figure 4.12. It should also be noted here that Texier (124) assumes the charge exchange mechanism operating in his experimental regime to be

controlled by the contact potential difference, i.e. the difference in the work functions of the impacting microsphere and target.

5.3.4 Temperature effects

If on impact with a target there is a resulting change in temperature, then the tunnelling process would be influenced thus affecting the magnitude of charge transferred. Such an increase in temperature has been considered by Beukema (38) (see Section 1.3.3) in his modified trigger discharge model, where it is assumed that in - flight field electron emission raises the temperature of the particle surface sufficiently to cause local melting and hence welding on impact. Such a rise in temperature would thus have a number of effects;

i) it would tend to assist the tunnelling mechanism and thus enhance the Q - value,

ii) it would cause a transition in 'sticking' effect whereby the particle would only return with the application of a strong field

Thirdly, in relation to (ii) the contact time would appear to increase thereby again increasing the magnitude of charge exchanged. From his analysis, Beukema has calculated the rise in temperature, $\triangle T$ due to such a mechanism to be equal to

$$\triangle T = \frac{2IVt^{\frac{1}{2}}}{\pi R a^2 (\pi K \rho c)^{\frac{1}{2}}} \quad - - - \; 5.8$$

where K, ρ and c are the thermal conductivity, density and specific heat of the carbonyl iron particle; R_a is the radius of the electron impact area, V is the particle/plane potential and results in a

transient current I flowing for a time t. Substituting values for these parameters that are appropriate to the present experimental regime yields a value for $\triangle T \sim 50$ K which is similar to that calculated by ukema at a field of $\sim 5 \times 10^{6} Vm^{-1}$. However, this is considerably lower than the melting point of carbonyl iron (~ 1800 K) and it can therefore be concluded that the rise in temperature due to such a mechanism is unlikely to have a significant influence on the charge exchange process. It is also important to note that in the present experimental regime $E_g < 10^{9}$ Vm^{-1} for all conditions, so that the possibility of in-flight field emission as proposed by Beukema can be neglected. A further mechanism that could result in a rise in temperature of a sub - micron junction has recently been suggested by Cook and Latham (87). They propose that electron - phonon scattering processes in the inter - facing oxide region between the particle and target, where the electron tunnelling process is taking place, are capable of dissipating sufficient energy to raise the sub micron junction temperature to a value at which melting and hence welding would occur. However, no direct evidence of such a mechanism is at present available.

5.3.5 Variation of particle potential

It can be seen from expression 2.35 that the particle potential V_p has a significant influence on the magnitude of charge exchanged. However, the variation of V_p with time viz. $V_{p(t)} = V_{op} \exp - t/tc$ as assumed in the existing theory appears to be a fairly arbitrary approximation and possibly incorrect and will be dealt with subsequently. The use of t_c as

the time constant can however be taken to be a reasonable approximation since observations have shown that the process of charge reversal is completed during contact. Further evidence of this can be obtained if theoretical values for the rebound charge are calculated using the equilibrium charge equation 5.9 detailed below, viz. a spherical microparticle initially lying in contact with a plane electrode will at some critical voltage V, (determined by a balance between adhesive attractive forces and the repulsive electrostatic forces) detach itself from the parent electrode. On detachment from the parent electrode it will acquire a charge given by (26)

$$Q_{o2} = Z \pi^3 \varepsilon_o E_o R_p^2 \qquad --- \qquad 5.9$$

where Z is a charge factor dependent on the particle and plane geometries i.e. for a microsphere resting on a plane $Z \simeq 6.6$, ε_o is the permittivity of free space, E_o is the macroscopic field = V/d, V is the applied voltage, d is the interelectrode gap and R_p is the radius of the particle. A theoretical curve of the q_2/q_1 values for a 2.5 micron particle and having an initial charge equal to 10^{-15} C is shown in Figure 5.6. Since thetheoretical values appear to be similar to the observed values it can be assumed that the process of charge reversal must indeed be completed during contact.

Looking more closely now at the situation of a positive particle approaching a negatively charged planar target it can be seen that the particle potential will decay with time as the particle gets closer to the plane. However, the decay is not necessarily

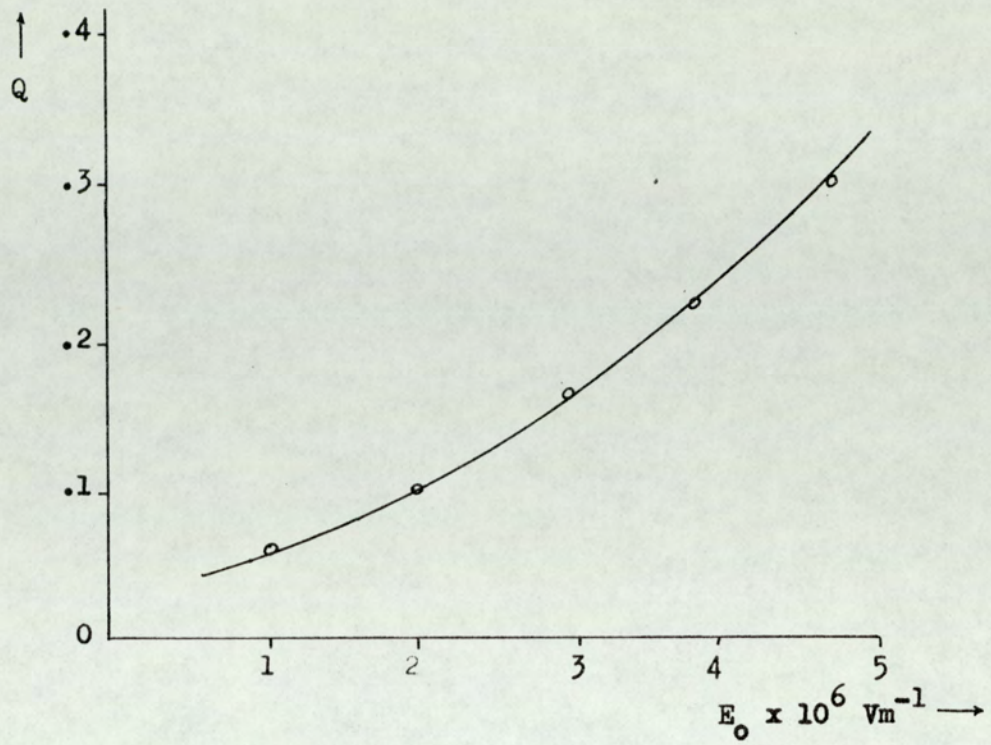

Figure 5.6

exponential as assumed in the existing theory and illustrated by the dotted line of Figure 5.7, since initially the three field components E_1, E_2 and E_3 (which have all been previously defined) will be acting jointly in one direction to assist the decay in particle potential. Thus initially the decay in V_p would be quite rapid, as illustrated by region (i) of Figure 5.7. However, as the sphere gets closer to the target, the negative charge flowing from the anode to the sphere will establish a p.d between it that creates a micro gap field which is in opposition to the enhanced field associated with the gap. Thus in an ideal situation where equilibrium could be established this charging process will continue until these two components are equal. In practice however, this would not occur since either the elastic strain involved in particle bouncing would be sufficiently large or the repulsive forces between

the particle and target would overcome the adhesive and image forces. Thus in the real case the total gap field would be reduced causing the particle potential to decay much more slowly as illustrated in region (ii) of Figure 5.7.

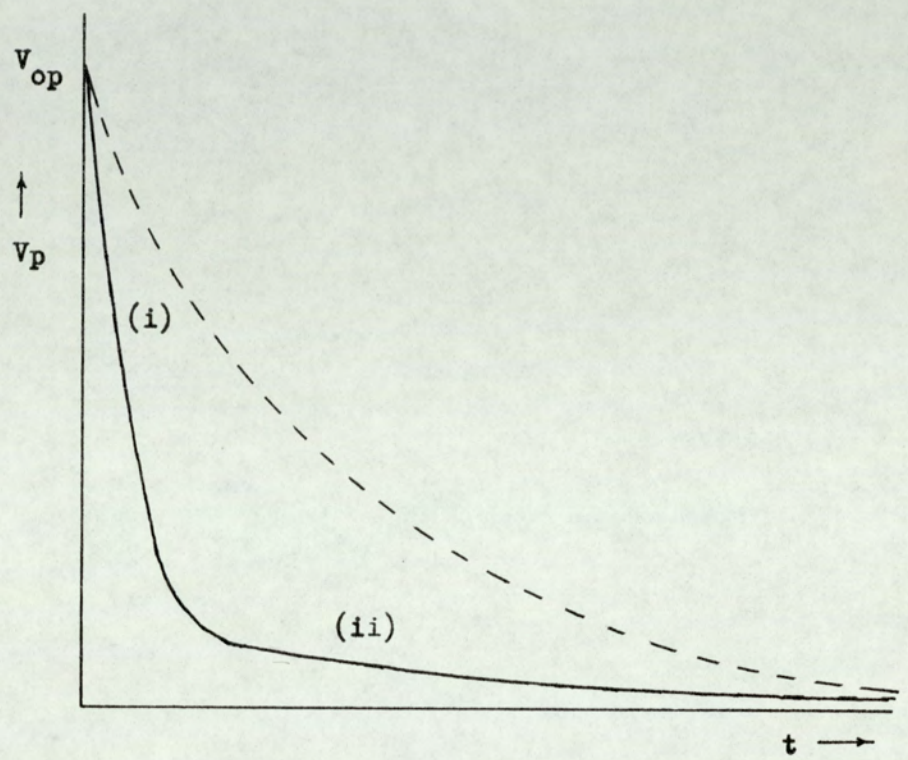

Figure 5.7

This therefore indicates that for most of the time low - bias conditions operate in the present experimental regime. Thus referring to earlier discussions a much smaller value (<1) of K at such low bias voltages can be assumed for the above situation. If now a theoretical plot of Q_r with E_o for a 2.5 micron particle at a gap thickness of $30^{o}A$ is plotted using modified values of a, t_c and K so that $a \simeq 2 \times 10^{-7}m$, $t_c \simeq 5 \times 10^{-7}s$ and $K \simeq \cdot 2$ it can be seen from Figure 5.8 that this is in close agreement with

typical experimental values. For the case of a 50°A film however, a much smaller charge transfer is predicted. This is not the case in practice where a greater magnitude of the reversed charge is observed with thick films. This can however be mainly attributed

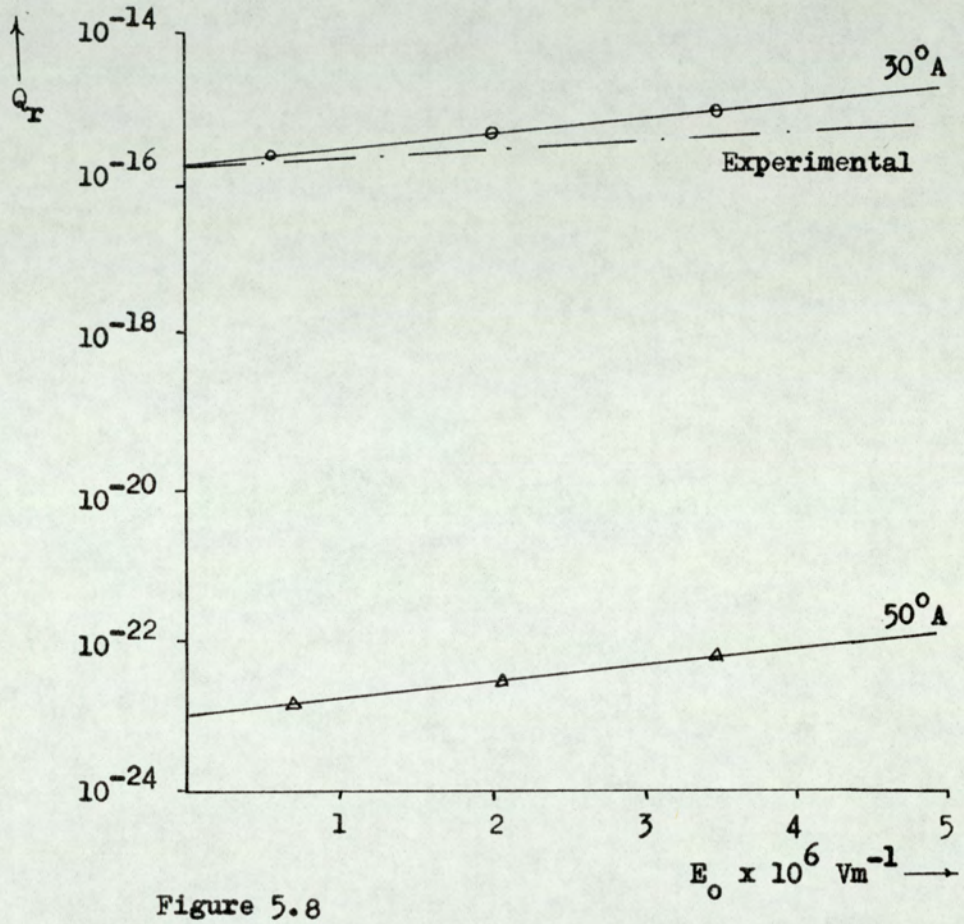

Figure 5.8

to the rather uneven nature of oxide films typically found on poly - crystalline samples, especially those which may also have undergone extensive diamond polishing (see Section 5.3.2). It should also be recognised that the non uniform nature of these films can result in quite large error in the thickness measurements by the ellipsometric technique ($\sim$ 1mm spot size) not to mention other errors being introduced by the use of

approximate optical constants for atomically clean metal surfaces and for the oxide films, where these films may be a combination of two or more different species. In addition, it should be noted that the materials used in the present study are not of ultra - pure quality but commercial materials containing small amounts of impurities which can affect the physical properties of these materials including the nature of the oxide films they may grow and thus influence their electrical and mechanical responses under impact conditions.

5.4 Technological implications

It is evident from the above findings that the efficiency of the particle energy enhancing mechanism is governed both by the mechanical and electrical aspects (as designated by the e and Q values respectively) associated with the electrical breakdown of a high - voltage vacuum gap. It is also clear from the discussion of Section 1.3.5 that for the kinetic energy of the particle to be enhanced between each impact, and thus for the bouncing mechanism to be efficient, the following condition must be fulfilled,

$$e^2 > 1 - Q \quad \text{or} \quad e^2 + Q > 1 \qquad - - - \quad 5.11$$

This relation therefore has two implications,

i) that since the e value has a square function then because e is always less than 1, e^2 must be very much smaller than 1, thereby indicating that Q must be of the order of 1, and

ii) that since energy enhancement is only possible if condition 5.11 is fulfilled, then for the bouncing mechanism to be inefficient, low e and Q values are necessary prerequisites for a stable high voltage electrode material.

From the findings of the impact data presented in Section 4 it can be seen that, in general the softer materials such as copper, gold and nickel yield low e values (0.5) whilst stainless steel and titanium yield high e values of up to 0.8. This gives a corresponding value for e^2 to be $\sim$ 0.25 for soft materials and $\simeq$ 0.7 for hard materials, indicating that copper and nickel are apparently more favourable as high voltage electrode materials.

These findings are in contrast to those found in practice where both titanium and stainless steel are found to be stable electrode materials with much greater breakdown voltages for a given inter-electrode vacuum gap. If now the electrical behaviour is compared it is again found that mechanically polished titanium alloys yield much bigger Q- values than the corresponding surfaces of copper and nickel. This again suggests that breakdown initiated by micro-particle bouncing impacts is much more likely with titanium and stainless steel electrodes than with copper or nickel. However, it must be noted that this highly efficient charge reversal and mechanical response of titanium is only specific to artificial situations where 'foreign' particles (e.g. carbonyl - iron and gold) with highly differing work functions and surface dielectric properties are employed. In the real situation where a large percentage of the naturally occurring microparticles are likely to consist of the parent electrode, the response of the microparticles may be quite different. In addition, since breakdown in the real situation is initiated far more readily when using copper and nickel as high voltage electrode materials (which is again in contrast to the findings of the experimental situation) then it would appear that initiation of breakdown with copper and nickel may in fact be due to one of the other mechanisms discussed in Section 1.

Comparing now the responses of the different surfaces of Ti 318 Ti 115 it is clear that the lowest Q - values are yielded by the argon ion etched surfaces and the lowest ϵ-values by the electro-polished surfaces. This therefore leads to a somewhat difficult situation since, as discussed earlier, a stable high voltage electrode

material must yield both low Q and e-values. To arrive at a reasonable assumption of the choice of a material and surface which will be potentially a more stable electrode in a high vacuum gap one must turn to expression 5.11 . Since, it now appears that $e^2 + Q > 1$ for energy enhancing particle bouncing events to occur, it can be assumed that for any given material and surface condition, the lower the combined value of $e^2 + Q$. the less probability there is of it breaking down. If this condition is now used as a criterion for breakdown, then the following values for $e^2 + Q$, for the differing surfaces of the two titanium alloys are obtained.

	Surface conditions	$e^2 + Q$	
		Ti 318	Ti 115
A	Mechanically polished	0.84	0.60
B	Argon ion etched	0.52	0.50
C	Electron bombarded	0.54	0.50
D	Electropolished	0.50	0.30

Thus, it would appear that if in fact breakdown in the real situation is initiated by the microparticle bouncing phenomenon, then an electropolished Ti 115 electrode surface would be the most appropriate to use as a high voltage electrode material. This is in contrast to a mechanically polished Ti 318 electrode which would prove to be the worst material. It is of interest to note here, that in other metallurgical applications of titanium, where surface properties are important (eg. corrosion resistance) such electropolished surfaces are used. From the impact data of the

various particle/electrode combinations, it would also appear that the breakdown criterion is markedly increased ($\simeq 0.94$) when the impacting carbonyl - iron microspheres are replaced by gold microspheres. Since, in this case the difference in work functions has also increased (from ~ 0.3 to > 1.0) then further justification can be obtained for the assumption that it is this difference in work functions, which may be the cause of the contrasting breakdown behaviour of electrode materials.

In conclusion, it must therefore be said that although the current data does not represent an exact simulation of a real gap, the present work has however isolated and clarified several aspects of the microparticle bouncing energy enhancing mechanism. Theoretically, it has served to provide a clearer insight into the rôle of the mechanical and electrical properties of the electrode surfaces in influencing the behaviour of low velocity microparticles trapped between a real interelectrode gap. However, several discrepancies between experimental and apparent practical experience leads to the notion that perhaps this energy enhancing particle bouncing mechanisms is not important in the real situation and that breakdown of such gaps could be due to some other mechanism. One such mechanism is the 'switching' mechanism where it is proposed that field penetration in an insulating microimpurity that is in intimate contact with the substrate metallic cathode, causes it to 'switch' to a high - conductivity state and it is this 'switching' which is a prerequisite for electron emission (15, 125). This therefore suggests that there is growing evidence of the fact that electron emission and microparticle sites would be significantly

reduced if impurities could be eliminated from electrode surfaces and that considerable improvement could result if electrode materials having electrically insulating and mechanically strong surface films were to be developed.

CHAPTER 6

6.0 Conclusion

It was established in Chapter 1 that there are two main mechanisms responsible for the breakdown of UHV high voltage gaps. The fundamental physical processes on which these are based are (i) the emission of electrons from localised 'point' sites on the electrode surface where it is assumed that the field is locally enhanced to $\geqslant 10^9$ Vm^{-1} at which field electron emission can occur and (ii) the concept that loosely adhering charged microparticles may become detached from an electrically stressed electrode surface resulting in their acceleration across the gap and subsequently causing impact ionisation. Processes(i) and (ii) are respectively assumed to be predominantly responsible for the electrical breakdown of small ($\leqslant$ 1mm) and large ($\geqslant$ 6mm) interelectrode gaps. At intermediate gaps ($1 \leqslant d \leqslant 6$mm) it is possible for both processes to operate. However, experimental evidence exists which strongly suggests that under some circumstances, microparticle based breakdown events can occur at low gaps, even though single transit energies are apparently too low to cause impact ionisation. To accommodate this apparent anomaly, it has been suggested that electrically charged low velocity microparticles may undergo bouncing sequences in the gap, so that if atthe same time, favourable conditions prevail then the particles will undergo charge and momentum reversal. This will therefore result in a progressive velocity enhancement of the particle leading to an ultimate impact velocity which is sufficient to cause a breadkown in an intermediate gap regime. The central aim of this investigation has been to investigate this proposition experimentally by studying the

bouncing impact behaviour of charged microparticles in simulated high voltage planar gap.

On the theoretical level this has involved firstly, a detailed consideration of the fundamental physical processes involved in such a micro impacting regime and secondly, a consideration of the role played by such a phenomena in the practical situation of a high voltage vacuum gap. In this connection, of principal importance is an analysis of the many complex electrical and mechanical interactions that take place as a charged microparticle impacts and bounces off a plane electrode. In order to investigate the particle bouncing phenomena under controlled experimental conditions and with an impact regime that lends itself to analytical treatment, a simulation technique has been used. This is based on a particle gun that can inject positively - charged, low - velocity microspheres into a high field gap for subsequent impact on a negatively charged planar electrode , whose surface states can be prepared in situ by argon ion etching and electron bombardment and precisely monitored by an ellipsometer facility. In these studies, particle bouncing events have been characterized in terms of two parameters. viz. ratio of the rebound to incident velocity (i.e. the coefficient of restitution or e - values) and the ratio of the charge carried by the rebound and incident particles (i.e. the Q - values). These two parameters are assumed to be directly indicative of the mechanical and electrical aspects of an impact. Experiments have been performed on a wide range of impacting surfaces, including different combinations of particle and target materials, and a variety of target preparation procedures. In this connection a particularly

detailed study has been made of the impact responses of two commercially produced titanium alloys, (Ti 318 and Ti 115) that are widely used as high voltage electrode materials.

From studies made on these alloys and other materials, it has been found that the 'microscopic' mechanical properties of the materials, as characterized by the e values, exhibit many trends that are similar to those found with corresponding macro - systems. However, it has been observed that i) there are significant differences in the critical velocity heralding the onset of inelastic deformation, and ii) there is a large scatter in the measured e values that can reach as much as 50% at the higher impact velocities. In the case of the electrical behaviour, as characterized by the Q values, similar trends have been observed for all particle / target combinations. These include the gradual increase in Q with increasing macroscopic gap field, and decrease in Q with increasing impact velocity. Again significant differences appear in the behaviour of individual surfaces and this is particularly true for the State A mechanically polished surfaces of the titanium alloys.

The experimental data has been utilized in two ways. Firstly in a qualitative evaluation in terms of the known microscopic mechanical and electrical properties of surfaces, (for example, strength, thickness and species of the oxide films, substrate work functions, dielectric constants and band gap) and secondly for a detailed evaluation of a theoretical model developed for calculating the magnitude of the charge exchanged between a charged microsphere and an oppositely charged planar electrode for an ideal sphere/plane model. This analysis suggested that whilst the mechanical

behaviour can be explained in terms of such factors as the non-planar microtopography of the various electrodes, the electrical behaviour has to be explained in terms of its extreme sensitvity to the thickness and electrical properties of the surface oxide films. In particular, the surprisingly anomalous behaviour of the mechanically polished titanium targets, which yielded much higher Q - values ($\sim$ 0.4) than the atomically clean ($\sim$ 0.15) or electropolished targets ($\sim$ 0.2) can be explained in terms of the difference in the relative work functions of the interacting materials.

The theoretical evaluation has shown that certain parameters used in the development of the existing theory, such as contact area and contact time, the contributions to the gap field Eg, and the decay of the particle potential V_p are incorrectly approximated. Appropriate refinements to the original theory have resulted in a modified expression for the magnitude of charge exchanged (Q_r) which shows close agreement with experimental findings.

In considering the technological implications of these findings to a UHV high vacuum gap it has firstly been noted that the experimental data does not represent an exact simulation of a real gap where a large percentage of the microparticles will be of the same materials as their parent electrodes. Thus the influence of work function differences (almost zero for the real case cf. with 0.5 eV for the experimental situation) between the particle and electrode, particularly for the mechanically polished surfaces will be negligible, and the charge reversal mechanism will therefore be

controlled by the ambient oxide film. If however, the operational gap field exceeds $\sim 6 \times 10^6$ Vm^{-1}, which is frequently the case in practice then it has been demonstrated that all mechanically polished surfaces approach a common charge reversal response. Under these conditions, any differences in the velocity enhancement from the bouncing mechanism must therefore arise from differences in the e - values. It would therefore appear that mechanically harder surfaces, such as would be provided by the refractory metals, would be more likely to promote the mechanism than the softer non-refractory metals. Secondly, the implications of the findings of the energy enhancing mechanism as discussed in terms of e and Q - values have shown that the breakdown criterion for a stable high voltage electrode material is for it to yield low e and Q - values, so that $e^2 + Q \geqslant 1$. This criterion is most easily achieved with the electropolished surface of a Ti 115 target ($e \sim 0.3$, $Q \sim 0.21$, $e^2 + Q \sim 0.30$) indicating it to be the most appropriate electrode surface for use as a UHV high voltage gap.

In conclusion it can be said that the present study has resulted in both a clearer understanding of the energy enhancing mechanism and a modified theoretical model which gives better agreement between theory and experiment. However, several factors, such as the rôle of the non - uniform surface oxidation of polycrystalline electrodes, the local enhancement of the macroscopic field by the 'rough' surface microtopography of diamond - polished electrodes and the initial distribution in microparticle radii and impact velocities need further clarification. In addition, to further test the validity of the present refined theoretical model, there

is the need to carry out more specialised experiments and if possible improve on this. Accordingly, suggestions for future work are presented in terms of possible experimental and theoretical refinements.

An obvious suggestion would be to use well defined planar targets such as 'dislocation free single crystals' so that the influence of impurities and non homogeneous oxides can be investigated. In addition, it would be desirable to use similar particle and electrode materials so that i) the real gap is better simulated and ii) the differences in mechanical and electrical properties are considerably reduced. On the more practical side, it would be desirable to firstly use a vertical particle injection and detection system as discussed in Section 5.1 and secondly create some means of particle radii and impact velocity selection. Also, since the macroscopic analogy may not be relevant to the present microscopic systems it would be desirable to measure the contact time t_c so that its full significance in determining the magnitude of charge exchanged may be investigated. This could be achieved by i) refining the experimental technique used in the present investigation and ii) using electrode and particle materials which yield bouncing events at low or zero fields. Finally, on the theoretical level, it would be desirable to look more closely at the improved field calculations and the corresponding expression for Q_r, which take into account the previously neglected effects due to differences in work functions of the interacting materials, so that discrepancies and limitations of the model can be clearly identified. It would also be desirable to use these expressions to look more closely at processes such as the trigger discharge process.

APPENDIX 1

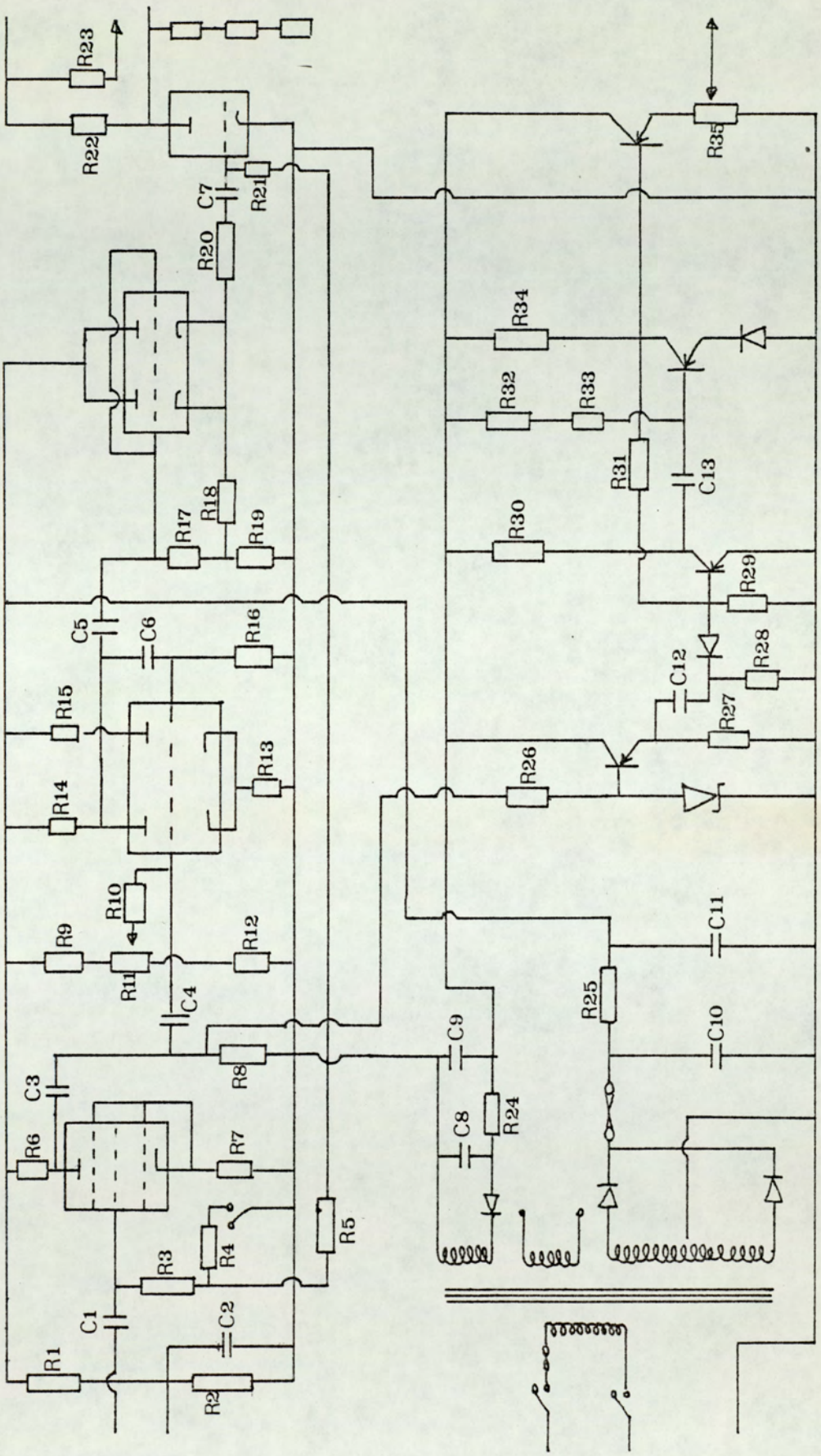

High voltage switch circuit

APPENDIX 2

Computer program used to evaluate particle parameters

```
10  Print  'U1'; 'V2'; 'Q1'; 'Q2'; 'Q'; 'R'; 'U2'; 'V1'; 'C1'
20  L = .03
30  D = 7873
40  Input  'G,T,V,C,W,' G,T,V,C,W
50  Select Print 05
60  Dim L1(20), L2(20), H1(20), H2(20), U1(20), U2(20), V1(20),V2(20),
    Q1(20), Q2(20), Q(20), R(20), C1(20)
70  For  N = 1  to  W
80  Input  'H1, H2, L1, L2,' H1(N), H2(N), L1(N), L2(N)
90  Next  N
100 For  N = 1  to W
110 U1(N)  =  L/L1(N)
120 V2(N)  =  L/L2(N)
130 Q1(N)  =  H1(N)/H2(N)
140 Q2(N)  =  H2(N)/H1(N)
150 C1(N)  =  U1(N)↑2/(2*V)
160 U2(N)  =  SQR (U1(N)↑2)  +  (2*C1(N)*T)
170 V1(N)  =  SQR (V2(N)↑2)  -  (2*(C1(N)/Q1(N)) * T)
180 Q(N)   =  (C*H1(N)*.05)/10
190 R(N)   =   (3*Q(N)*V)/(2*D*π*U1(N)↑2) ↑ .333
200 Print using 220, U1(N), V2(N), Q1(N), Q2(N), Q(N), R(N), U2(N),
    V1(N), C1(N)
210 %     . . . . . .___ . . . . . .____ . . . . . .___
          . . . . . .___ . . . . . .____ . . . . . .___
```

```
220.  Next  N
230   Print 'V = ', V: Print 'T = ', T: Print 'G = ', G'.
      Print 'C = ', C: Print 'E = ', T/G: Print 'R = ', R/W
240   Select  Print  005
250   Go to 20
```

LIST OF REFERENCES

1 Fowler,R.H. & Nordheim,L.; Proc.Roy.Soc.,A119,173-81,(1928)

2 Haefer,R.;Z.Physik, 116,604-22,(1940)

3 Ahearn,A.J.; Phys.Rev., 50,238-53,(1936)

4 Boyle,W.S.,Kisliuk,P., & Germer,L.H.; J.Appl.Phys.,26,720-5,(1955)

5 Farrall,G.A.; J.Appl.Phys.,41,563-71,(1970)

6 Dyke,W.P. & Trolan,J.K.; Phys.Rev.,89,799-808,(1953)

7 Alpert,D.,Lee,D.A.,Lyman,E.M. & Tomanschke,H.E.; J.Vac.Sci. Technol.,1,35-50,(1964)

8 Little,R.P.&Whitney,W.T.; J.Appl.Phys.,34,2430-32,(1963)

9 Little,R.P. & Smith,S.T.; J.Appl.Phys.,36,1502-4,(1965)

10 Van Oostrum,A.; Proc.1Vth.Int.Sym. on Disch. & Elec.Ins. in Vac.,Waterloo,1-12,(1970)

11 Cox,B.M.; J.Phys.D: Appl.Phys.,8,2065-73,(1975)

12 Hurley,R.E. & Dooky,P.J.; J.Phys.D: Appl.Phys.,10,L195-7,(1977)

13 Allen,N.K. & Latham,R.V.; J.Phys.D: Appl.Phys.,11,L55-7,(1978)

14 Hurley,R.E.; J.Phys.D: Appl.Phys.,12,2229-32,(1979)

15 Athwal,C. & Latham,R.V.; 1Xth.Int.Sym. on Disch. and Elec.Ins. Vac.Eindhoven(1980)

16 Charbonnier,F.M.,Bennette,C.J. & Swanson,L.W.; J.Appl.Phys., 38,627-33,(1967)

17 Chatterton,P.A.; Proc.Phys.Soc.,88,231-45,(1966)

18 Utsumi,T.; J.Appl.Phys.,38,2989-97,(1969)

19 Cranberg,L.; J.Appl.Phys.,23,518-22,(1952)

20 Slivkov,I.N.; Sov.Phys.Tech-Phys.,2,1928-34,(1957)

21 Hansen,D.O. & Roy,N.L.; Nucl.Instrum.Meth.,40,209-12,(1966)

22 Slattery,I.C.,Friichtenicht,J.F. & Hansen,D.O.; Appl.Phys. Letters,7,23-5,(1965)

23 Anderson,H.W.; Trans.Am.Inst.Elec.Engrs.,54,1315-20,(1935)

24 Menon,M.M. & Srivastava,K.D.; J.Appl.Phys.,45,3832-35,(1974)

25 Birdar,P.J. & Chatterton,P.A.; S.Agn.Phys.,30,163-70,(1970)

26 Hurley,R.E. & Parnell,T.M.; J.Phys.D:Appl.Phys.,2,881-7,(1969)

27 Texier,C.; J.Phys.D:Appl.Phys.,10,1693-1702,(1977)

28 Rohrbach,F.; Cern.Courier,9,208-12,(1969)

29 Puiz,F.; Cern.Report,TC-L/Int.,72,(1972)

30 Jenkins,J.E. & Chatterton,P.A.; J.Phys.D:Appl.Phys.,10,L17-23,(1977)

31 Olendzkaya,N.S.; Rad.Eng. & Elec.Phys.,8,423-9,(1963)

32 Martynov,E.P.; Electronnya Technica Serio,3,(1968)

33 Chatterton,P.A.,Menon,M.M. & Srivastava,K.D.; J.Appl.Phys., 43,4536-42,(1972)

34 Chak rabarti,A.K. & Chatterton,P.A.; Proc.V1th.Int.Conf.on Disch. & Elec.Ins. in Vac.,Swansea,16-21,(1974)

35 Beukema,G.P.; J.Phys.D:Appl.Phys.,7,1740-55,(1974)

36 Dietzel,H.,Neukem,G. & Rauser,P.; J. of Geo.Phys.Research, 77,1375-95,(1972)

37 Friichtenicht,J.F.; Rev.Sci.Instrum.,33,209-15,(1965)

38 Auer,S. & Sitte,K.; Earth & Planet Sci. Letters,4,178-83,(1968)

39 Smith,D. & Adams,N.G.; J.Phys.D:Appl.Phys.,6,700-19,(1973)

40 Brah,A.S. & Latham,R.V.; J.Phys.D:Appl.Phys.,8,L109-11,(1975)

41 Latham,R.V.; J.Phys.D:Appl.Phys.,5,2044-54,(1972)

42 Latham,R.V. & Braun,E; J.Phys.D:Appl.Phys.,3,1663-9,(1970)

43 Latham,R.V. & Brah,A.S.; J.Phys.D:Appl.Phys.,10,151-67,(1977)

44 Latham,R.V.,Brah,A.S.,Fok,F. & Woods,M.O.; J.Phys.D:Appl. Phys.,10,139-50,(1977)

45 Hertz,H.; J.Reine Agnew.Math.,92,56-65,(1889)

46 Tabor,D.; Proc.Roy.Soc.Am.,A192,247-74,(1948)

47 Bowden,F.P. & Tabor,D.; Friction Lubrication of Solids,(Lond.-Oxford Univ.Press),(1964)

48 Greenwood,J.A. & Williamson,J.B.P.,; Proc.Roy.Soc.,Lond., A295,300-19,(1966)

49 Archard,J.F. & Whitehouse,J.; Proc.Roy.Soc.,A316,97-121,(1970)

50 Andrews,J.P.; Phil.Mag.,9,593-610,(1930)

51 Hutchings,J.M.; J.Phys.D:Appl.Phys.,10,L179-83,(1977)

52 Tabor,D.; The Hardness of Metals,(Oxford Clarenden Press),(1951)

53 Fuller,K.N. & Tabor,D.; Proc.Roy.Soc.,Lond.,A345,327-43,(1975)

54 Holm,R.; Electrical Contacts,Stockholm;Hugh Gerber,(1946)

55 Shaw,P.E. & Leavey,E.W.; Phil.Mag.,10,809-14,(1930)

56 McFarlane,J.S. & Tabor,D.; Proc.Roy.Soc.,Lond.,A202,224-52,(1950)

57 Kendall,K.; J.Phys.D:Appl.Phys.,4,1186-95,(1971)

58 Johnson,K.L.,Kendall,K. & Roberts,A.D.; Proc.Roy.Soc.,Lond., A324,301-13,(1971)

59 Tabor,D. & Winterton,R.H.S.; Proc.Roy.Soc.,Lond.,A312,435-50,(1969)

60 Gane,N.,Pfaelzer,P.F. & Tabor,D.; Proc.Roy.Soc.,Lond.,A340, 495-517,(1974)

61 Pollock,H.M.;Shufflebottom,P. & Skinner,J.; J.Phys.D:Appl. Phys.,10,127-38,(1977)

62 Easterling,K.E. & Swann,P.R.; Acta Met.,19,117,(1971)

63 Dayson,C. & Lowe,J.; Wear,21,263-88,(1972)

64 Navara,E. & Easterling,K.E.; Int.J.Powder Met.,7,111,(1971)

65 Kittell,C.; Introduction to Solid State Physics,2nd.ed.,John Wiley & Sons,N.Y.,(1956)

66 Simmons,J.G.; Trans. of Metallur. Soc. of Aime,233,485-92,(1965)

67 Simmons,J.G.; J.Appl.Phys.,34,1793-1803,(1963)

68 Burstein,E. & Lundqvist,S.; Tunnelling Phenomenon in Solids, Plenum Press,N.Y.,(1969)

69 Simmons,J.G.; J.Appl.Phys.,34,2581-90,(1963)

70 Simmons,J.G.; J.Appl.Phys.,35,2472-81,(1964)

71 Standley,C.L. & Maissel,L.J.; J.Appl.Phys.,35,1530-34,(1964)

72 Martynov,E.P. & Ivanov,V.A.; Rad.Eng. & Elec.Phys.,14,1732-35,(1969)

73 Lorrain,P. & Carson,D.R.; Electromagnetic Fields and Waves, (San Francisco:W.H.Freeman & Co.),(1970)

74 Miller,H.C.; J.Appl.Phys.,38,4501-4 ,(1967)

75 Morse,P.M. & Feshbach,H.; Methods of Theoretical Physics,II, New York,McGraw Hill,(1953)

76 Shelton,H.,Hendricks,C.D. & Wuerker,R.F.; J.Appl.Phys.,31, 1243-50,(1960)

77 Brah,A.S.; Ph.D. Thesis,Univ. of Aston in Birm.,(1977)

78 Brah,A.S. & Latham,R.V.; J.Phys.E:Sci.Inst.,9,119-23,(1976)

79 Read,F.H.,Adams,A. & Solo-Montiel,J.R.; J.Phys.E:Sci.Inst., 4,625-32,(1971)

80 Feynman,R.P.,Leighton,R.B. & Sands,H.; Feynman Lectures on Physics,2,710-11,(Massachusetts:Addison Wesley),(1970)

81 Khorossany,M. & Fitch,R.K.; Vacuum,27,159-62,(1977)

82 Franks,J. & Ghander,A.M.; Vacuum,24,489-91,(1974)

83 Dhariwal,R.S. & Fitch,R.K.; J.Mat.Sci.,12,1225-29,(1977)

84 Ditchburn,R.W.; J.Opt.Soc.Am.,45,743-8,(1955)

85 Neal,W.E.J. & Fane,R.W.; J.Phys.E:Sci.Instrum.,6,409-16,(1973)

86 Jacquet,P.A.; Rev.Met.,46,214-5,(1949)

87 Cook,S. & Latham,R.V.; 1Xth. Int.Sym. on Disch. & Elect.Ins. in Vac.,Eindhoven,(1980)

88 Tabor,D.; Surface Phys. of Materials,II,Blakely,London,Acad. Press,(1975)

89 Menard,C.J.; J.Opt.Soc.Am.,52,427-31,(1962)

90 Johnson,D.L. & Tao,L.C.; Surf.Sci.,16,390-6,(1969)

91 Carroll,J.J. & Melmed,A.J.; J.Opt.Soc.Am.,64,514-5,(1974)

92 Hass,G. & Bradford,A.P.; J.Opt.Soc.Am.,47,125-9,(1957)

93 McCrackin,F.L.; NBS Technical Note,479-81,(1969)

94 Smith,T.; Surf.Sci.,38,292-312,(1973)

95 Hickman,J.W. & Gulbransen,E.A.; J.Analy.Chem.,20,158-62,(1948)

96 Andreeva,V.V. & Aleskeeva,E.A.; Proc.Acad.Sci.U.S.S.R.Phys. Chem.Sect.,134,793-7,(1960)

97 Cathcart,J.V.,Campell,J.J. & Smith,G.P.; J.Elec.Chem.Soc., 105,442-6,(1958)

98 Borie,B.S. & Sparks,C.J.; Acta Crystallog.,14,569-70,(1961)

99 Wallwork,G.R.; Rep.Prog.Phys.,39,401-83,(1976)

100 Taylor,G.I.; J.Inst.Civil Engg.,26,486-519,(1946)

101 Dietzel,H. & Tabor,D.; J.Geophys.Res.,77,1375-95,(1972)

102 Bowden,F.P. & Tabor,D.; Friction and Lubrication of Solids, II,Oxford Univ.Press,(1950)

103 Samuels,L.E.; J.Inst.Metals,85,51-6,(1956)

104 Barrett,E.; Structure of Metals,McGraw Hill Book Co.,(1969)

105 McCracken,G.M.; Rep.Prog.Phys.,38,241-327,(1975)

106 Stewart,A.D.G. & Thompson,M.W.; J.Mat.Sci.,4,56-60,(1969)

107 Shore,P.J.; Iron Steel Inst.,2,59-67,(1918)

108 Maurer,W.C.& Rhinehart,J.; J.Appl.Phys.,31,1247-57,(1960)

109 Shewman,P.G.; Transformations in Metals,McGraw-Hill,N.Y.(1969)

110 Maissel,L.I. &Glang,R.; Handbook of Thin Film Technology, McGraw-Hill,N.Y.,(1970)

111 Gane,N.; Proc.Roy.Soc.Lond.,A317,367-91,(1970)

112 Hansen,D.O.; Appl.Phys.Letters,13,89-91,(1968)

113 Tabor,D.; Surface Colloid Sci.,5,245-312,(1972)

114 Chakrabarti,A.K.; Ph.D. Thesis,Univ. of Liverpool,(1975)

115 Brah,A.S. Mohindra, S. & Latham,R.V.; V111th.Int.Sym. on Disch. & Elec. Ins. in Vac.; Albuquerque,New Mexico,(1978)

116 Thomas,S.; Surface Sci.;55,754-8,(1976)

117 Tomashov,N.D., Alkovskii,R.M. & Tabushnerev,M.; Dokl.Akad.Nauk., (USSR),Tom.2,141,(1961)

118 Von Hippel,A., Dielectric materials and applications, John Wiley & Sons Inc.,N.Y.,(1954)

119 Chopra,K.L.; J.Appl.Phys.,36,184-7,(1965)

120 Feng,J.S.Y., Pashley,R.D. & Nicolet,M.A.; J.Phys.C: Solid State Phys.,8,1010-21,(1975)

121 Anderson,J.S. & Greenwood,N.N.; Proc.Roy. Soc.,A215,353-70,(1952)

122 Smith,T.; Surface Sci.,27,45-59,(1971)

123 Chang,Y.W., Lo,W.J. & Somorjai,G.A.; Surface Sci.,64,588-92,(1977)

124 Texier,C.; Phys. Abstracts,No.6700,1-11,(1979)

125 Latham,R.V.; High Voltage Vacuum Insulation; The Physical basis, Academic Press, N.Y.,London,(1981)

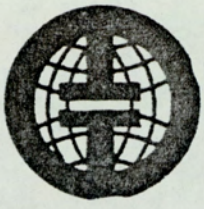

VIII International Symposium on

Discharges and Electrical Insulation in Vacuum

5th - 7th September 1978

Sandia Laboratories
Albuquerque, New Mexico ····· 87185
U.S.A.

MICROPARTICLE BOUNCING BEHAVIOUR FROM OXIDISED AND ATOMICALLY CLEAN ELECTRODE SURFACES

A.S. Brah*, S. Mohindra and R.V. Latham
Department of Physics, University of Aston, Birmingham B47ET,U.K.

ABSTRACT

Studies have been made on the bouncing impact behaviour of positively charged microparticles in a high-voltage vacuum gap. Comparative impact data is presented for commercially polished and atomically clean electrodes of copper, titanium and stainless steel which illustrates how the particle charge and momentum reversal processes are very sensitive to the surface condition of the target electrode.

INTRODUCTION

The behaviour of micron-sized charged particles in a high voltage vacuum gap, in particular the mechanisms by which they can initiate electrical breakdown of the gap, has been the subject of considerable research. One important mechanism is based on the phenomena of microparticles bouncing between electrodes, where it was proposed by Latham and Braun [1] that under favourable conditions of charge and momentum reversal, this phenomena could result in a progressive velocity enhancement with an ultimate impact velocity sufficient to cause breakdown. This hypothesis was subsequently verified under controlled laboratory conditions by Brah and Latham [2] using artificially generated microparticles.

This experimental technique was subsequently refined for conducting more detailed studies of the bouncing mechanism with the aim of determining the parameters that control the momentum and charge reversal.

* Department of Metallurgy & Materials Science, Imperial College of Science and Technology, London, U.K.

It was found that the efficiency of these exchange processes depended strongly on the target electrode material, which was subsequently shown to be related to the surface properties of the electrodes. In a detailed investigation by Latham and Brah [3] using in situ argon ion etching and ellipsometry techniques, it was established that removal of the ambient oxide film present on copper and stainless steel electrodes enhanced the charge reversal mechanism in both cases.

The present short paper reports on further results from the above study and includes new impact data from experiments on a titanium alloy (Ti 318) which is widely used in high voltage vacuum technology.

EXPERIMENTAL

The investigation was carried out under ultra high vacuum conditions using the low-velocity microparticle facility illustrated in Figure 1 and fully described elsewhere [2] [3] [4] [5] [6]. Briefly, it consists of a dust source gun (Mg) from which carbonyl iron spheres ranging in diameter from .5 to 5 μm could be delivered into the experimental chamber. The focussing and final velocity of the particles was controlled by a decelerating electrostatic lens (EL). A drift tube (Dt) through which the particles passed, together with a charge sensitive amplifier (A) and a storage oscilloscope, constituted the particle detecting system. From the height and width of the pulse obtained on the scope it was possible to calculate respectively the particle charge and velocity. The 'test' high voltage gap (d) is formed between an earthed grid (G) and planar target electrode T. The target electrodes can be rotated from the 'test' positio to the 'service' position where their surfaces may be cleaned in situ by an argon ion (Ig) etching facility. Whilst in this "service" position an ellipsometer (Ep) is used to determine the thickness of the oxide layer

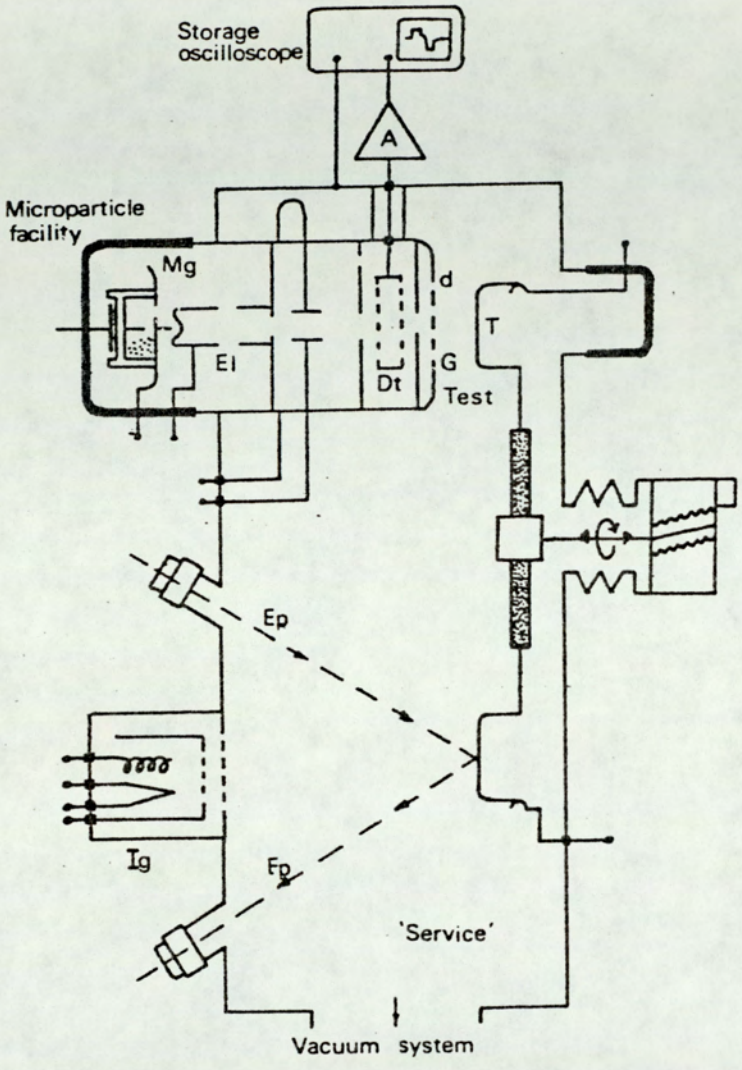

Figure 1. Schematic representation of the experimental lay-out within the UHV chamber (vertical elevation)

present on the surface both before and after ion bombardment. With this facility it is possible to compare impact characteristics of a given target material in its commercially polished state (State A) and its atomically clean state (State B).

RESULTS

The data obtained from the impact of carbonyl-iron spheres on the three target materials of copper (1) stainless steel (2) and titanium (3) has been collated in Figures 2 to 5. Each experimental point represents the average of approximately 50 individual particle impact events covering a range of particle velocities from 20 to 100 ms^{-1} and particle diameters from 0.5 to 5 μm. For convenience of interpretation, the data is presented in terms of the electrical and mechanical aspects of the bouncing mechanism. Thus Figures 2 and 3 show respectively how the ratio of the incident to reversed charge (q_1/q_2) varies with the macroscopic gap field E for states A and B of the three materials. Similarly, Figures 4 and 5 show the variation of the coefficient of restitution (e) with the particle impact velocity (v_i) for the two states.

Since low values of q_1/q_2 correspond to efficient charge reversal, it follows from Figures 2 and 3 that in all cases the exchange process is enhanced with increasing gap field. For the commercially polished surfaces of Figure 2 (State A), titanium is clearly the most efficient in promoting the mechanism and stainless steel the least effective. Removal of the surface oxide from the target (State B - Figure 3) results in a reversal of the previous situation with the charge exchange process becoming more efficient for stainless steel and copper and less efficient for titanium. Figure 4, again representing the commercially polished surfaces, shows

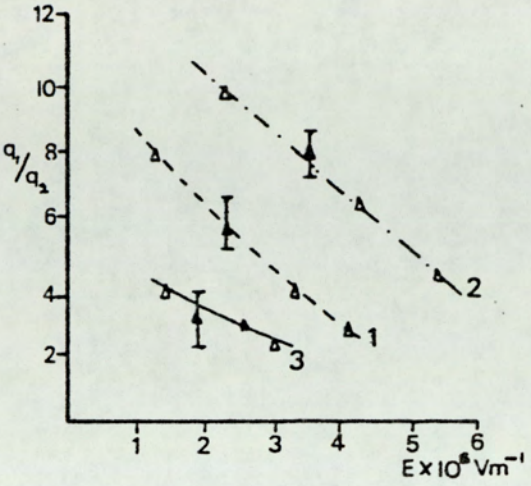

Figure 2. Charge reversal data obtained from commercially polished electrodes. (State A)

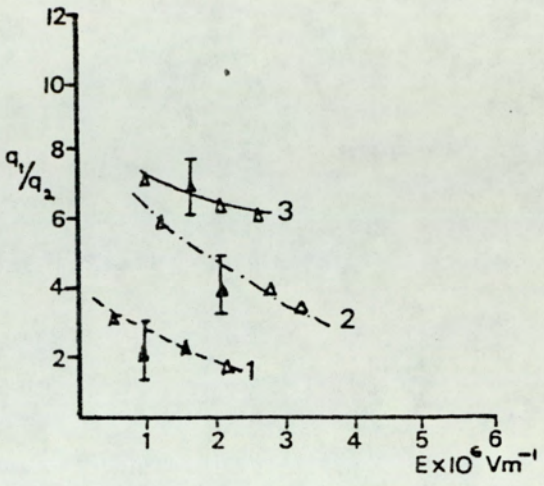

Figure 3. Charge reversal data (q_1/q_2) obtained from atomically clean electrodes. (State B)

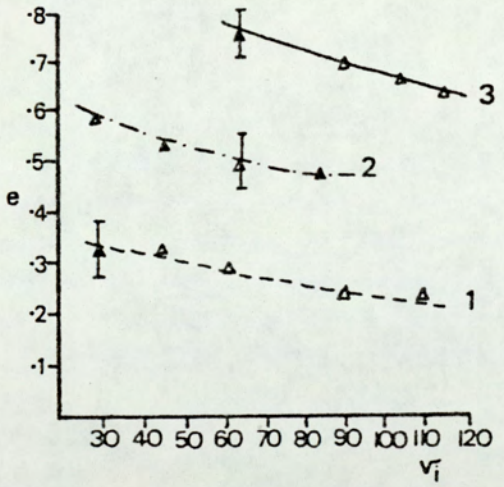

Figure 4. Coefficient of restitution (e) data obtained from commercially polished electrodes. (State A)

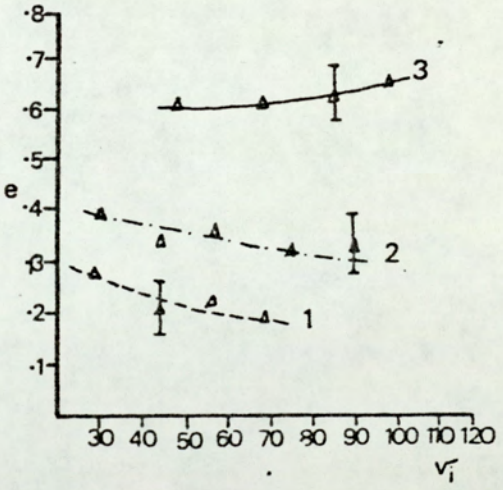

Figure 5. Coefficient of restitution (e) data obtained from atomically clean electrodes (State B)

that in general the e-values tend to decrease with increasing impact velocity. In addition, the relative microscopic hardnesses of the three materials, as measured by the mean microscopic e-values have been found to be in good agreement with their corresponding macroscopic hardness values [5]. Referring to Figure 5, which gives the data obtained from the atomically clean surfaces (State B), it will be seen that removal of the oxide film has resulted in a significant lowering of the e-values for each material. However the relative hardnesses of the three surfaces remain unchanged.

Finally it should be noted that the restricted range of the macroscopic E-fields for which measurements could be made on State B surfaces is a consequence of the well known instability that results from the ion-etching of electrode surfaces. For example, whilst 10 kV can be supported by a 2 mm gap with a State A target, only $\sim$5 kV can be used for a State B target if breakdown of the gap is to be avoided.

DISCUSSION

The type of charge reversal data presented in Figure 3 has been successfully interpreted by Latham and Brah [3] in terms of a transient metal-insulator-metal (MIM) quantum mechanical electron tunnelling mechanism that occurs during the brief contact ($< 10^{-8}$s) of a charged microsphere with the target electrode. For a given junction, the tunnelling current density (j) is determined by the external bias voltage applied across the junction (V) and the tunnelling resistance (σ) of the junction [7], where $j = \frac{V}{\sigma}$. In the present particle impact regime, V will depend on the particle charge and the macroscopic gap field, whilst σ is a complex function of the particle and target work functions (ϕ_p and ϕ_T respectively) and the thickness and electrical properties of the composite oxide film [3]. The actual electric

field (E_T) existing across a junction, which is directly responsible for the tunnelling current, is the sum of the external component (E_e) derived from the bias voltage V, whose direction is always such as to promote electron tunnelling from the target to particle, and an internal component (E_i) derived from the internal bias arising from any difference in the substrate work functions. Accordingly, three types of tunnelling regime may be considered:

(i) $E_T = E_e$, corresponding to $\phi_p = \phi_T$ so that Ei = 0

(ii) $E_T = E_e + E_i$, corresponding to $\phi_p > \phi_T$ so that the junction is "forward-biased"

(iii) $E_T = E_e - E_i$, corresponding to $\phi_p < \phi_T$ so that the junction is "reverse-biased".

The mean values of the quoted work functions for the three materials studied in their ambient state, i.e. equivalent to state A, are:-

$$\phi_{Cu} - 4.45, \quad \phi_{Fe} - 4.47, \quad \phi_{Ti} - 3.95, \quad \phi_{St.St.} - 4.5$$

It therefore follows from the above discussion that since $\phi_{Fe} - \phi_{Cu} - \phi_{St.St.}$, the impact data obtained from the copper and stainless steel targets correspond to tunnelling regime (1) and that the enhanced charge reversal observed for State B targets has to be interpreted in terms of the reduced thickness of the intermediate oxide film as discussed by Latham and Brah [3] . In the case of the State A Ti - target, the tunnelling junction will be "forward biased" since $\phi_{Fe} > \phi_{Ti}$, and this will give rise to an enhanced charge reversal response that is clearly evident in the experimental characteristics of Figure 2. The increase of the q_1/q_2 ratio for the State B Ti-target, which is in sharp contrast to the behaviour of the other materials, can only be explained if it is

assumed that the ion etching process has resulted in a significant increase in the Ti work function so that the tunnelling regime is altered from being "forward" to "reverse" biased:this effect is then assumed to predominate over the enhancement expected from the reduction of the oxide thickness. In support of this explanation, reference can be made to measurements which confirm that the necessary changes in the work function of Ti can occur following Ag-ion etching, the effect being attributed to ion impregnation [8] [9].

Referring to Figures 4 and 5, the significant lowering of the e-values for all three materials between their state A and state B surfaces can readily be explained in terms of the influences of the ambient surface oxide film which is generally known to be mechanically harder than its substrate metal. In addition, the reduction of the e-values with increasing impact velocity follows the behaviour associated with macro systems and has been discussed elsewhere [5].

In considering the implication of these findings to the practical problem of the breakdown of commercially polished (state A) high voltage electrodes by microparticle impact following multiple bouncing [1] [10] [3], it has to be assumed that particles will generally be of the same materials as their parent electrodes, so that $\phi_p = \phi_T$ and there will be no "forward" or "reverse" biassing effects : the charge reversal mechanism will therefore be controlled by the properties of the ambient oxide film [3]. If however the operational gap field exceeds $\sim 6 \times 10^6$ V m^{-1}, which is frequently the case in practice, Figure 2 indicates that all state A surfaces approach a common charge reversal response. Under these conditions any differences in the velocity enhancement from the bouncing mechanism must therefore arise from differences in the e-values. It would therefore

appear that mechanically harder surfaces, such as would be provided by the refractory metals, would be more likely to promote the mechanism than the softer non-refractory metals.

REFERENCES

1. R.V.Latham and E.Braun, J.Phys.D:Appl.Phys. 3, 1663 (1970).
2. A.S. Brah and R.V.Latham, J.Phys.E:Sci.Instruments 9, 119 (1976).
3. R.V. Latham and A.S.Brah, J.Phys.D:Appl.Phys. 10, 151 (1977).
4. A.S. Brah and R.V.Latham, J.Phys.D:Appl.Phys. 8, L109 (1975).
5. R.V. Latham, A.S. Brah, K.Fok and M.Woods, J.Phys.D:Appl.Phys. 10, 139 (1977).
6. R.W. Fane, W.E J. Neal and R.V. Latham, J. Appl.Phys. 44, 740 (1973).
7. J.G. Simmons, J.Appl.Phys. 34, 2581 (1963).
8. T. Smith, Surface Science 27, 45 (1971).
9. Y.W. Chang, WJ. Lo and G.A. Samorjai, Surface Science 64, 588 (1977).
10. R.V. Latham, J.Phys.D:Appl.Phys. 5, 2044 (1972).